UC Merced

UC Merced Electronic Theses and Dissertations

Title

Exploring Organic Photophysics: A Computational Study of Potential Energy Surfaces and Transition States

Permalink

https://escholarship.org/uc/item/3291w8dc

ISBN

9798197875457

Author

Sarabia, Cristian

Publication Date

2026-05-08

Peer reviewed|Thesis/dissertation

eScholarship.org Powered by the California Digital Library
University of California

UNIVERSITY OF CALIFORNIA, MERCED

Exploring Organic Photophysics: A Computational Study of Potential Energy Surfaces and Transition States

A dissertation submitted in partial satisfaction of the
requirements for the degree of
Doctor of Philosophy

in

Chemistry

by

Cristian Sarabia

Committee in charge:
Professor Hrant Hratchian, Chair
Professor Ryan Baxter, Advisor
Professor Rebeca Arevalo
Professor Sayantani Ghosh

2026

© Cristian Sarabia, 2026
All rights reserved

The Dissertation of Cristian Sarabia is approved, and it is acceptable in quality and form for publication on microfilm and electronically:

_____
Professor Hrant Hratchian, Chair

_____
Professor Ryan Baxter, Advisor

_____
Professor Rebeca Arevalo

_____
Professor Sayantani Ghosh

University of California, Merced
2026

Dedication

To my father, Francisco Jesus Trigueros,

Thank you, for a lifetime of inspiration, and for teaching me grit, determination, and persistence. He was a fierce proponent of education and believed in me and in what I could achieve more than I did in myself. I am forever indebted to him for his love, support, and wisdom. All your years of hard work were noticed and not in vain. An undertaking of this magnitude would not have been possible without you as my father. This achievement is yours as much as it is mine.

To my wife, Alexandra Danielle Saxberg,

Thank you, for your unconditional love, support, and unwavering belief in our family and me. I could not have achieved this feat without your encouragement, care, and assistance. You are the support system that made it possible to accomplish my goal. I am beyond grateful for all the sacrifices you have endured on this journey, and there would be no success without you by my side. You deserve as much praise and commendation for the effort it took to make me reach my full potential and achieve this milestone. I will spend a lifetime attempting to match your strength and support for our family and me.

Table of Contents

List of Tables ..... **vii**

List of Figures ..... **viii**

Acknowledgements ..... **xi**

Curriculum Vita, Publications, and Field of Study ..... **xiii**

Abstract ..... **xviii**

Chapter 1 Introduction **1**

1.1 Quantum Mechanics 1

1.2 The Hartree Fock Method 3

1.3 Density Functional Theory 6

1.4 Time-Dependent Density Functional Theory 8

Chapter 2 Computational and Mechanistic Analysis of Nitroso Compounds **11**

2.1 Background 11

2.2 A New Reagent for Transnitrosation 13

2.3 Second Generation Transnitrosation Reagents 19

2.3.1 Diethyl NO-1 Analog 20

2.3.2 Diphenyl NO-1 Analog 21

2.3.3 Diisopropyl NO-1 Analog 22

2.4 Conclusion 22

Chapter 3 Organic Photophysics of Benzoyl Pyrazinium Salts **24**

3.1 Background 24

3.2 Observations 25

3.3 Study of Reactivity Due to Structural Factors 29

3.3.1 Testing electron deficiency on the N atom 29

3.3.2 Testing electron withdrawing effects on the pyrazinium ring 31

3.3.3 Testing the presence of a charge 33

3.3.4 Testing the charge dipole produced by the charge 34

3.4 Push Pull Systems and Hammett Study 36

3.5 Conclusion 42

Chapter 4 Δ-SCF Methods for Charge Transfer Excitations **44**

4.1 Background 44

4.2 Results 45

4.2.1 Ruthenium and MLCT 45

4.2.2 Copper and LLCT 47

4.2.3 Zirconium and LMCT 50

4.3 Conclusion 53

Chapter 5 Transition State Optimization 54
5.1 Background 54
5.2 The Newton-Raphson Method 55
5.2.1 The Hessian Eigen Basis 56
5.2.2 The Trust-Region Newton-Raphson 58
5.3 Quasi Newton Methods 60
5.4 TS Optimization Methods 61
5.5 Gradient Decomposition Method 63
5.6 Results 65
5.7 Conclusions 69
References 71

List of Tables

Table 1 Quantitative metrics for Δ-SCF vs TD-DFT on Charge Transfer States

List of Figures

Figure 2.1 Biologically active nitroso compounds 11
Figure 2.2 N-nitroso urea's structural activity relationship 12
Figure 2.3 N-nitroso compound synthesis 12
Figure 2.4 N-nitroso compound synthesis Mechanism 12
Figure 2.5 TBN equilibrium with alcohols 12
Figure 2.6 N-nitrososulfonamide (NO-1) Reagent 13
Figure 2.7 X-Ray Crystal Structure of NO-1 as a mixture of rotamers NO-1a and NO-1b (LEFT). The structures of NO-1a and NO-1b and interconversion between the two (RIGHT). 13
Figure 2.8 Relaxed potential energy scan of NO-1 using the S-N-N-O dihedral angle (RED). The scan rotates the S-N-N-O dihedral angle at ten degree intervals and reoptimizes the NO-1 energy at the new geometry. The relaxed energy scan is performed using DFT with the B3LYP functional, basis set 6-311+G(2d,p) and the PCM solvent model with acetonitrile. 14
Figure 2.9 Relaxed potential energy scan of NO-1 using the S-N-N-O dihedral angle (RED). Constrained sp^2 NO-1 PES using S-N-N-O dihedral angle (GREEN). Constrained sp^3 NO-1 PES using S-N-N-O dihedral angle (BLUE). 15
Figure 2.10 Nitrogen-Nitrogen bond length scan of NO-1 using the S-N-N-O dihedral angle (RED). Constrained sp^2 NO-1 PES using S-N-N-O dihedral angle (GREEN). Constrained sp^3 NO-1 PES using S-N-N-O dihedral angle (BLUE). 16
Figure 2.11 Nitrogen-Oxygen bond length scan of NO-1 using the S-N-N-O dihedral angle (RED). Constrained sp^2 NO-1 PES using S-N-N-O dihedral angle (GREEN). Constrained sp^3 NO-1 PES using S-N-N-O dihedral angle (BLUE). 17
Figure 2.12 Sulfur-Oxygen bond length scan of NO-1 using the S-N-N-O dihedral angle (RED). Constrained sp^2 NO-1 PES using S-N-N-O dihedral angle (GREEN). Constrained sp^3 NO-1 PES using S-N-N-O dihedral angle (BLUE). 18
Figure 2.13 Relaxed dihedral energy scan of NO-1 performed using DFT with the B3LYP functional, basis set 6-311+G(2d,p), and the PCM solvent model with acetonitrile. 18
Figure 2.14 Relaxed dihedral energy scan of NO-1 performed using DFT with the B3LYP functional, basis set 6-311+G(2d,p), and the SMD solvent model with acetonitrile. 19
Figure 2.15 Relaxed dihedral energy scan of DiethylNO-1 performed using DFT with the B3LYP functional, basis set 6-311+G(2d,p), and the SMD solvent model with acetonitrile. 20
Figure 2.16 Relaxed potential energy scan of DiethylNO-1 using the S-N-N-O dihedral angle (RED). Constrained sp^2 DiethylNO-1 PES using S-N-N-O dihedral angle (GREEN). Constrained sp^3 DiethylNO-1 PES using S-N-N-O dihedral angle (BLUE). 21
Figure 2.17 Relaxed dihedral energy scan of DiphenylNO-1 performed using DFT with the B3LYP functional, basis set 6-311+G(2d,p), and the SMD solvent model with acetonitrile. 21

Figure 2.18 Relaxed dihedral energy scan of DiisopropylNO-1 performed using DFT with the B3LYP functional, basis set 6-311+G(2d,p), and the SMD solvent model with acetonitrile. 22
Figure 3.1 UV-Vis Absorption spectrum of Benzoyl Pyrazinium 26
Figure 3.2 Hole and Particle NTOs for Benzoyl Pyrazinium Excited State 7 27
Figure 3.3 Benzoyl Pyrazinium Difference Density between ground state and 7th excited state 27
Figure 3.4 Pyrazinium Partioning Scheme for Theodore Analysis..... 28
Figure 3.5 Benzoyl Pyrazinium Theodore Analysis Results..... 28
Figure 3.6 Hole and Particle NTOs for PyraziniumH Excited State 7..... 29
Figure 3.7 PyraziniumH Theodore Analysis Results 29
Figure 3.8 Electron Deficient Pyrazinium Derivatives 29
Figure 3.9 Benzoyl Pyrazine Theodore Analysis Results 30
Figure 3.10 Benzoyl Pyridine Theodore Analysis Results..... 31
Figure 3.11 Benzoyl PyrazineB4 Theodore Analysis Results 31
Figure 3.12 Electron withdrawing pyridine derivatives..... 32
Figure 3.13 Benzoyl PyridineNO2 Theodore Analysis Results..... 32
Figure 3.14 Benzoyl PyridineCN Theodore Analysis Results 33
Figure 3.15 Benzoyl PyridineCF3 Theodore Analysis Results..... 33
Figure 3.16 MePyridyl Pyrazinium Theodore Analysis Results..... 34
Figure 3.17 Phenoxide Pyrazinium Theodore Analysis Results 35
Figure 3.18 Phenoxide Pyrazinium Excited State 1 NTOs 35
Figure 3.19 Phenoxide Pyrazinium Excited State 2 NTOs 36
Figure 3.20 Para-substituted Benzoyl Pyrazinium Derivatives..... 36
Figure 3.21 Linear Free Energy Relationship between CT and a hammet parameter. 37
Figure 3.22 Linear Free Energy Relationship between CT and a hammet parameter. 38
Figure 3.23 Linear Free Energy Relationship between CT and a hammet parameter. 38
Figure 3.24 Electronic effects on absorption λ_{max} of compounds in (Figure 3.20)..... 39
Figure 3.25 CN BenzoylPyrazinium Theodore Analysis Results 40
Figure 3.26 CHO BenzoylPyrazinium Theodore Analysis Results 40
Figure 3.27 FBenzoylPyrazinium Theodore Analysis Results 41
Figure 3.28 MeBenzoyl Pyrazinium Theodore Analysis Results 41
Figure 3.29 MeOBenzoyl Pyrazinium Theodore Analysis Results 42
Figure 3.30 NH2Benzoyl Pyrazinium Theodore Analysis Results..... 42
Figure 4.1 RuBiPy Particle NTO 45
Figure 4.2 RuBiPy Hole NTO..... 46
Figure 4.3 RuBiPy TD-DFT Density Difference 46
Figure 4.4 RuBiPy Δ-SCF Difference Density 47
Figure 4.5 MACCu(I)CzCN Particle NTO 48
Figure 4.6 MACCu(I)CzCN Hole NTO..... 48
Figure 4.7 MACCu(I)CzCN TD-DFT Difference Density..... 49
Figure 4.8 MACCu(I)CzCN Δ-SCF Difference Density 49
Figure 4.9 Zr(IV)Me(PDP)$_2$ Particle NTO..... 50
Figure 4.10 Zr(IV)Me(PDP)$_2$ Hole NTO 51
Figure 4.11 Zr(IV)Me(PDP)$_2$ TD-DFT Density Difference 51

Figure 4.12 $Zr(IV)Me(PDP)_2$ Δ-SCF Difference Density 52
Figure 5.1 The Schlegel model potential energy surface showing reactant and product minima, multiple transition states (first-order saddle points), and a second-order saddle point. 55
Figure 5.2 Gradient Decomposition Method between adjacent minima on the Muller-Brown surface. 66
Figure 5.3 Gradient Decomposition Method between adjacent minima on the Muller-Brown Surface 67
Figure 5.4 Gradient Decomposition Method between nonadjacent minima on the Muller-Brown surface. 68
Figure 5.5 Gradient Decomposition Method between adjacent minima on the Schlegal surface. 69

Acknowledgements

I would like to first start by thanking my wife, best friend, and colleague, Alexandra Danielle Saxberg. Her support throughout these past years has undoubtedly been more than I ever expected, more than I could have ever asked for, and truly one of the biggest reasons I was able to make it this far in my career. She has been with me since the beginning of this journey in undergrad, where she recognized, encouraged, and supported my passion for mathematics, chemistry, and science. I could not imagine moving on to the next chapter of my life without Alex. You gave me the I truly could not have asked for a stronger life partner, and for that, I am eternally grateful.

I am also deeply indebted to my advisors, Professor Ryan Baxter and Professor Hrant Hratchian. They have surpassed what I expected in mentorship, both professionally and personally. As a scientist, Ryan always challenged any assumptions and preconceived notions, and made me always think from first principles. This really pushed me not to just assume everything I thought was true was always correct and to truly understand why the equations and principles I learned were true and when they applied. Experimentally, he taught me to think of experiments as a way to probe and ask questions that can only have a true-or-false answer, which gets me closer to understanding and testing the hypothesis I am making. I truly feel I am a better scientist overall because I had the privilege of working alongside him. Personally, he took the time to look into resources when I was starting a family to make sure my entire family always had access to full health care coverage. When I suffered the loss of my father due to the pandemic, he made sure I was provided with the resources from the university as I transitioned to being the head of my family. I can truly say that when I asked him for help, he left no stone unturned and made sure I would succeed.

Professionally, Hrant accepted me when I didn't know any theory or how to open a terminal. My biggest transformation in computational technical abilities, I really owe it all to his mentorship. He always checked in on me during our weekly meetings and was never too proud to walk me through how to do something himself no matter how elementary the task. He really showed me how to lead by example and I never felt any task I was given was not something he wouldn't do himself. Personally, he always made sure I was medically taken care of by the university due to my chronic medical condition and made sure I never had a lapse in my medical care because of him. I can sincerely say he cares about my well-being and has made sure it was never an issue during these past couple of years. He was also extremely supportive during the time I was starting a family and made sure I had the time to attend every doctor's appointment with my wife no matter the meeting. He really taught me how to do science at the highest level and made sure I always had time for my family.

Thanks are also in order to Professor Auroa Pribram-Jones for all the moral support and graduate school experiences she shared with me throughout the years. She constantly kept reminding me what each graduate school milestone meant and how much I had grown since beginning grad school. Her wisdom really helped me navigate grad school during the toughest moments and gave me the encouragement I needed from an outsiders' perspective at those critical times. I am also grateful for the support and assistance of my lab mates in both labs. Their technical support over the past years was critical to ensuring I was able to accomplish all of my graduate school goals. These past years have helped me build camaraderie not only with my lab mates but with the UC Merced chemistry department as a whole. I would like to, in particular, recognize the members of the Isborn, Pribram-Jones, and Shi groups for always allowing me to learn from them in their respective fields and for welcoming me into their labs whenever I had a question. My work also benefited heavily from my committee members, Professors Arevalo and Ghosh, who provided valuable scientific insights throughout my Ph.D. studies.

I would be remorseful if I did not thank Lilia DeLaCerda from my alma mater, Fresno State, for being my first and life-long mentor. Lilia, in her role as the LSAMP program director, was the first person to show me what a career in science was and how to apply to PhD programs. Throughout the time that I have known her, she has supported me on my journey to the PhD through research grants, tutoring, poster presentations, and conferences. Even beyond undergrad, she helped apply for fellowships, like the NSF GRFP, that I don't think I would have otherwise applied for and earned without her incredible support. She really changed the trajectory of my life from the moment I met her, my first day of college, and I would not be where I am today without her guidance, encouragement, and immense support.

I would also like to acknowledge the sacrifices my mother, grandparents, and family made to give me the opportunity and privilege to get an education in America. It is only because of their hard work and the disparities they endured that I was able to achieve this. Thank you to my family and siblings for your love and support. You are the fuel that helped me get up every day and push me across the finish line. To my in-laws and new family, thank you for showing me unconditional support throughout this arduous journey. Your support has been invaluable and will forever be remembered. I could not have achieved this without your daily assistance. Last but not least, I would like to thank my tia Connie and tio Arnoldo, who both supported me emotionally and my education in more ways than one. Thank you for always showing up at school when I needed you the most, your kindness and love for my family and me is beyond measure.

Curriculum Vita, Publications, and Field of Study

CRISTIAN SARABIA

Email: csarabia4@ucmerced.edu
Github: sarabiacristian

EDUCATION

Ph.D., Chemistry*, expected* 2026 August 2019-Current
University of California, Merced (UC Merced)

M.S., Chemistry, December 2022 August 2019-December 2022
University of California, Merced (UC Merced)

B.S., Biochemistry, May 2017 August 2012-May 2017
Minors: Physics and Mathematics
California State University, Fresno (CSU, Fresno)

HONORS/AWARDS

Graduate Division Fellowship	August 2023-August 2024
Chemistry Department Outstanding Service Award	May 2024
NSF Graduate Research Fellowship Program	August 2019-August 2024
LSAMP Bridge to Doctorate Fellowship	August 2017-August 2019
ASI Undergraduate Research Grant	August 2016-May 2017
Louis Stoke Alliance for Minority Participation (LSAMP) Research Grant	August 2014-May 2016
CSU-LSAMP PROUD Scholar for Outstanding Research in STEM and Leadership	October 2016
President Volunteer Service Award	March 2016

RESEARCH EXPERIENCE

Graduate Research August 2019-Current

Advisors: Hrant Hratchian, Ph.D. and Ryan Baxter, Ph.D.
Project 1: Transition States Optimization Method Development
Objective: Create a new numerical method for finding molecular transition states optimization that is robust.
University of California, Merced

• Numerical methods optimization codes such as Gradient Descent, Newton-Raphson, BFGS, Wolfe-Conditions Line Searches, and Hessian Updating in Fortran, Julia, and Python

• Numerical Differentiation of Gradients, Jacobians, and Hessians using Finite Differences and Automatic Differentiation.
• Potential Energy Surface Exploration with Gaussian16
• Optimization and Frequency Analysis of compounds using Gaussian16

Project 2: Photoinduced Cyclization of Benzoyl Pyrazinium Salts
Objective: Quantitative Absorption Prediction for Photoinduced Cyclization
University of California, Merced
• Computational modeling of Molecular Excited States
• Quantitative Structure Property Relationships
• Computational Spectroscopy
• Charge Transfer Quantification

Summer Internships
Lawrence Livermore National Lab Data Science Challenge June–July 2022
• Used molecular features to predict binding to COVID-19 spike protein
• Performed PCA on Drug Features and Random Forest to predict drug binding
• Performed Hyper parameter optimization for Machine Learning Models

Undergraduate Research June 2014-May 2017
Advisor: Qiao-Hong Chen, Ph.D.
Project: Curcumin Analogues
Objective: Synthesizing Curcumin Analogues as Anti-Prostate Cancer Agents
California State University, Fresno

- Synthesized various analogues or derivatives of Curcumin and Fisetin as anticancer agents, using acid-base, alkylations, oxidations, Aldol condensation, and Wittig reactions
- Purified the synthesized compounds through liquid-liquid extractions, recrystallization, Preparative Thin Layer Chromatography, and Silica Gel Column Chromatography
- Characterized chemical structures of the synthesized compounds through Infrared Spectroscopy and ^{1}H and ^{13}C nuclear magnetic resonance spectroscopy.

JOURNAL PUBLICATIONS

Baxter, R.; Yaghoubi, M.; Rajaram, P.; **Sarabia, C.** 3,3-Dimethyl-2-Nitroso-2,3-Dihydrobenzo[d] Isothiazole-1,1-Dioxide. *Encycl. Reagents Org. Synth.* **2022**, 1–2.

Galloway, J. D.; **Sarabia, C**.; Fettinger, J. C.; Hratchian, H. P.; Baxter, R. D. Versatile New Reagent for Nitrosation under Mild Conditions. *Org. Lett.* **2021**, 23, 3253-3258.

"Structure-activity relationship studies of 1,7-diheteroarylhepta-1,4,6-trien-3-ones with two different terminal rings in prostate epithelial cell models", Rubing Wang, Xiaojie Zhang, Chengsheng Chen, Guanglin Chen, **Cristian Sarabia**, Qiang Zhang, Shilong Zheng, Guangdi Wang, and Qiao-Hong Chen, *European Journal of Medicinal Chemistry*, *133* (16): 208-226 (**2017**).

PRESENTATIONS

Cristian Sarabia, Ryan Baxter, and Hrant Hratchian, "Toward an improved method for optimizing Transition Structures" poster presentation, American Chemical Society National Meeting, San Diego, California, USA, March 25, 2025.

Cristian Sarabia, Pravien Rajaram, Ryan Baxter, and Hrant Hratchian, "Investigating intramolecular charge transfer in benzoyl pyrazinium organic salts" oral presentation, American Chemical Society National Meeting, New Orleans, Louisiana, USA, March 21, 2024.

Cristian Sarabia, Ryan Baxter, and Hrant Hratchian, "Computational Photophysical Characterization of Benzoyl Pyrazinium Salts" poster presentation, West Coast Theory Conference, Davis, California, USA, May 6, 2023.

Cristian Sarabia, Ryan Baxter, and Hrant Hratchian, "ONIOM Virtual Screening of the CB1 receptor and target identification" oral presentation, American Chemical Society National Meeting, Chicago, Illinois, USA, March 21, 2022.

Cristian Sarabia, Ryan Baxter, and Hrant Hratchian, "A Versatile New Reagent for Nitrosation" oral presentation, UC Merced Chemistry Department Seminar, Merced, California, USA, April 30, 2021.

Rubing Wang, Chengsheng Chen, **Cristian Sarabia**, Xiaojie Zhang, and Qiao-Hong Chen, "Synthesis and cell-based evaluation of 1,7-diarylheptatrien-3-ones with different terminal aromatic rings," oral presentation, the 37th Annual Central California Research Symposium, Fresno, California, USA, April 20, 2016.

Rubing Wang, Chengsheng Chen, **Cristian Sarabia**, Xiaojie Zhang, and Qiao-Hong Chen, "Synthesis and antiproliferative evaluation of 1,7-diarylhepta-1,4,6-trien-3-ones with different terminal aromatic rings," poster presentation, the 28th Annual CSU Biotechnology Symposium, Garden Grove, California, January 7-9, 2016.

Chengsheng Chen, **Cristian Sarabia**, Xiaojie Zhang, Rubing Wang, and Qiao-Hong Chen, "Asymmetric 1,5-diheteroaryl-1,4-pentadien-3-ones: a new class of promising anti-prostate cancer agents," oral presentation, The 36th Annual Central California Research Symposium, Fresno, California, USA, April 22, 2015.

TEACHING EXPERIENCE

Teaching Assistant, UC Merced Chemistry Department, Merced, CA
August 2019-May 2026
Organic Chemistry: Lectured and provided supplemental instruction to students on the basic principles of organic molecules and their structure, synthetic methods and analysis of molecules.
General Chemistry: Instructed students on Lewis Dot Structures, Molecular properties such as polarity, dipole moments, and Intramolecular forces

Facilitator, CSU Fresno LSAMP Program, Fresno, CA
August 2014-May 2017
Organic Chemistry: Lectured and provided supplemental instruction to students on the basic principles of organic molecules and their structure, synthetic methods and analysis of molecules.
Calculus: Taught students functions, graphs, derivatives, partial derivatives, vectors, with techniques and applications of integration.
Demonstrated basic arithmetic and computational procedures for the evaluation of definite and indefinite integrals.

Tutor, CSU Fresno Learning Center, Fresno, CA
August 2015-May 2017
Chemistry: Assisted students with course and lab materials in General Chemistry, Organic Chemistry, Biochemistry and Physical Chemistry. Worked with students from diverse majors, ethnicities, backgrounds, and age groups. Also created worksheets, flashcards, practice tests, and mock final exams for students. Received training about effective learning based on neuroscience, psychology, and higher education research.

LEADERSHIP ACTIVITIES

Lead Organizer, Joint Computational & Theoretical Chemistry Meetings, Merced, CA
August 2021-December 2022

- Organized bimonthly workshops on computing skills such as:
    - Python
    - Fortran
    - Julia
    - Mathematica
- Organized Guest Speakers and Lectures on Computational Chemistry

Lead Peer Mentor, CSU Fresno LSAMP Program, Fresno, CA
August 2013-May 2017

- Implemented retention activities for students who face social,

educational, or economic barriers
- Assisted with career and educational planning and dealing with the transition to the university
- Coordinated with program director to implement peer mentoring for first year students

Senator, College of Science and Mathematics, CSU Fresno, Fresno, CA
August 2015-May 2016
- Represent the students in College of Science and Mathematics (CSM) regarding campus issues and making sure students voices are heard
- Attend various campus meetings such as Senate Meetings, ASI Committee Meetings, Academic Meetings, and First Year Experience Committee
- Visit CSM student club meetings to inform members of the opportunities available including funding and volunteering.
- Awarded CSM student club sponsorships.
- Coordinated social and professional events for CSM students and clubs.

COMMUNITY SERVICE

Career Day, Luther Burbank Elementary School**,** Merced, CA
May 2024
Science Fair Judge, Chenoweth Elementary School**,** Merced, CA
February 2022
Physics Outreach, CSU Fresno Physics Department, Fresno CA
January 2017-May 2017
ASI Community Revitalization Program, CSU Fresno ASI, Fresno CA
May 2015-May 2016

Abstract

Exploring Organic Photophysics: A Computational Study of Potential Energy Surfaces and Transition States
by
Cristian Sarabia
Doctor of Philosophy
in
Chemistry
University of California, Merced

Rational design of molecules for chemical transformations and optoelectronic devices requires an understanding of excited state electronic transitions and the pathways connecting stable conformers on potential energy surfaces (PES). In this work, we demonstrate how computational methods like PES scans can be used to elucidate and design new reagents for chemical transformations. We also show how to use photophysical characterization of compounds, like charge transfer (CT), oscillators strengths, and absorption profiles can be used to design and chemically tune optical properties. We then show how Δ-SCF methods can be used to model CT states qualitatively using difference densities and quantitatively with CT distance metrics against methods like TD-DFT. Lastly a new method for transition state (TS) optimization is developed and evaluated on complex topologies like the Müller-Brown and Schlegel surfaces.

Chapter 1

Introduction

"Those who are not shocked when they first come across quantum theory cannot possibly have understood it."

-Niels Bohr

1.1 Quantum Mechanics

For several decades, computational chemistry has become extremely popular and standard practice for studying chemical transformations. In particular, quantum chemistry has gained popularity due to the availability of standard black-box algorithms for computing ground state and excited state chemical descriptors. The appeal and success of quantum chemistry is based on electronic structure theory, a first principles, or *ab initio*, approach to calculate molecular properties based on a many electron wavefunction evaluated from a Hamiltonian operator using only established physical laws and constants. Ab initio approaches that systematically increase in complexity and computational cost have been developed in order to treat electron correlation more accurately. The foundation to all of these more complex methods begins with the Hartree-Fock (HF) method. Let us first take a step back and understand the basic problem that these methods are trying to solve.

We begin with the partial differential equation used to describe a single particle system, like electrons in a molecule, the Time-Dependent Schrodinger Equation, (TDSE) proposed by Erwin Schrödinger,

$$i\hbar\frac{\partial\Psi(\mathrm{x,t})}{\partial\mathrm{t}} = -\frac{\hbar^2}{2m}\frac{\partial^2\Psi(x,t)}{\partial t^2} + V(x,t)\Psi(x,t) \qquad (1.1)$$

where i is the imaginary unit, $\hbar$ is Planck's constant, h, divided by 2π, $V(x,t)$ is the potential energy operator, and m is the mass of the electron or particle of interest.[1] Using the method of separation of variables, one can separate the wavefunction $\Psi(x,t)$ into its spatial and time components, Eq. 1.2, where x denotes the spatial coordinates of the particle and t represents time.

$$\Psi(x,t) = \psi(x)\phi(t) \qquad (1.2)$$

Plugging in Eq. 1.2 into Eq 1.1 and isolating for the time variable, one arrives at Eq 1.3.

$$\frac{d\phi(t)}{dt} = -\frac{iE}{\hbar}\phi(t) \qquad (1.3)$$

Solving this differential equation gives the time component of the wavefunction $\phi(t)$,

$$\phi(t) = e^{-\frac{iE}{\hbar}t} \tag{1.4}$$

In a similar manner, plugging Eq 1.2 into Eq 1.1 and isolating for the spatial variable gives the time-independent Schrödinger Equation (TISE):

$$\hat{H}|\psi(x)\rangle = E|\psi(x)\rangle \tag{1.5}$$

where ψ is the wavefunction and contains all the necessary information of the quantum mechanical system of interest, $\hat{H}$ is the Hamiltonian or total energy operator, and E is the total energy of the system. It is important to note that the wavefunction ψ is not an observable quantity and that it is the probability amplitude of the system. The probability amplitude squared, $|\psi|^2$, by definition, is the probability density of finding the particle in space. The Hamiltonian operator $\hat{H}$ is the total energy operator defined as the sum of the kinetic and potential energy operators and crucial for understanding the properties of the system. To obtain all the molecular properties of the system of interest, one must first solve the Schrödinger Equation. Solving the Schrödinger Equation will yield the total energy of the system and allow for the derivation of its molecular properties. The Hamiltonian operator for a multielectron system in atomic units is given by the following:

$$\hat{H} = -\sum_{A=1}^{M}\frac{1}{2M_A}\nabla_A^2 - \sum_{i=1}^{N}\frac{1}{2}\nabla_i^2 - \sum_{i=1}^{N}\sum_{A=1}^{M}\frac{Z_A}{r_{iA}} + \sum_{i}^{N}\sum_{j>i}^{N}\frac{1}{r_{ij}} + \sum_{A}^{M}\sum_{B>A}^{M}\frac{Z_A Z_B}{R_{AB}} \tag{1.6}$$

where the first two terms are the kinetic energy of the nuclei and electrons respectively, M_A represents the mass of the nuclei, ∇_A^2 represents the Laplacian with respect to the nuclear coordinates, and ∇_i^2 represents the Laplacian with respect to the electron coordinates. The third term represent the electron-nuclear attraction potential energy where Z_A is nuclear charge and r_{iA} is the electron nuclear distance. The fifth term is the nuclear-nuclear repulsion energy between atoms in a molecule where Z_A and Z_B are the nuclear charges of the atoms and R_{AB} is the internuclear distance between the nuclei. Lastly, we have the fourth term which is the electron-electron repulsion potential energy where r_{ij} is the electron-electron distance. This term in many cases is what prevents the solution to Schrödinger Equation since it couples the positions of the electrons to each other, also referred to as correlated electron motion. This term is what many molecular quantum mechanical models aim to approximate.

The solutions to the one electron terms in Eq 1.6 are the solutions to the Hydrogen atom. In systems of more than one electron, however there is no analytic solution to the Schrödinger Equation due to the fourth term in Eq 1.6. This is because the fourth term couples the positions of the electrons and does not allow for the separation of the variables. In order to solve this conundrum, various methods with different approximation have been created that attempt to solve the multielectron Schrödinger Equation with varying degree of accuracy and computational cost.

The first approximation that is generally made to Eq 1.6 is the Born-Oppenheimer approximation, which decouples the nuclear motion from the electrons motion.[2] The

justification behind this approximation is that nuclei in molecules are several magnitudes heavier than electrons and so it is reasonable to assume that nuclei are stationary from the frame of reference of the electrons. This results in the following simplification:

$$\hat{H}_e = -\sum_{i=1}^{N}\frac{1}{2}\nabla_i^2 - \sum_{i=1}^{N}\sum_{A=1}^{M}\frac{Z_A}{r_{iA}} + \sum_{i}^{N}\sum_{j>i}^{N}\frac{1}{r_{ij}} + \sum_{A}^{M}\sum_{B>A}^{M}\frac{Z_A Z_B}{R_{AB}} \tag{1.7}$$

where the first term in Eq 1.6 is gone due to the fact that the nuclei are stationary. This new simplified Hamiltonian Eq 1.7 is referred to as the electronic Hamiltonian. Since all the nuclear positions are fixed the last term simplifies to just being a constant and Eq 1.7 reduces to:

$$\hat{H}_e = -\sum_{i=1}^{N}\frac{1}{2}\nabla_i^2 - \sum_{i=1}^{N}\sum_{A=1}^{M}\frac{Z_A}{r_{iA}} + \sum_{i}^{N}\sum_{j>i}^{N}\frac{1}{r_{ij}} + \hat{V}_{NN}(R) \tag{1.8}$$

So, by invoking the Born-Oppenheimer approximation we have reduced the Schrödinger Equation, to an electronic Hamiltonian with fixed nuclear coordinates that reduces to Eq 1.8. The separation of the Hamiltonian into an electronic and nuclear component is a consequence of performing separation of variables on ψ into an electronic ψ_e and nuclear ψ_N components. Therefore, the Born-Oppenheimer approximation mathematically allows you to decouple the electronic and nuclear degrees of freedom such that the electronic Hamiltonian and electronic wavefunction only depend parametrically on the nuclear coordinates.

1.2 The Hartree Fock Method

The fundamental building block of wavefunction theory for the multielectron Schrödinger Equation is the Hartree Fock method.[3–9] The first important approximation the Hartree Fock method does is assume a single slater determinant wavefunction Ψ, an anti-symmetrized product of one electron molecular orbitals (MO) χ_N:

$$\Psi(\mathbf{x}_1, \mathbf{x}_2, \cdots, \mathbf{x}_\mathrm{N}) = \frac{1}{\sqrt{N!}}\begin{vmatrix} \chi_1(\mathbf{x}_1) & \chi_2(\mathbf{x}_1) & \cdots & \chi_\mathrm{N}(\mathbf{x}_1) \\ \chi_1(\mathbf{x}_2) & \chi_2(\mathbf{x}_2) & \cdots & \chi_\mathrm{N}(\mathbf{x}_2) \\ \vdots & \vdots & \ddots & \vdots \\ \chi_1(\mathbf{x}_N) & \chi_2(\mathbf{x}_N) & \cdots & \chi_\mathrm{N}(\mathbf{x}_\mathrm{N}) \end{vmatrix} \tag{1.9}$$

where $\mathbf{x}_\mathrm{N}$ are the spin and spatial coordinates and N is the number of electrons in the system.

For a multielectron system, the Hartree product Eq 1.10 is the simplest way to approximate Ψ:

$$\Psi(\mathbf{x}_1, \mathbf{x}_2, \cdots, \mathbf{x}_\mathrm{N}) = \chi_1(\mathbf{x}_1)\chi_2(\mathbf{x}_2)\cdots\chi_\mathrm{N}(\mathbf{x}_\mathrm{N}) \tag{1.10}$$

while the Hartree product does manage to simplify the representation of the wavefunction Ψ using products of single particle wavefunctions χ, it still violates the Pauli exclusion

principle. The Pauli exclusion principle states that the molecular wavefunction must be antisymmetric such that:

$$\hat{\mathcal{P}}_{12}\Psi(\mathbf{x}_1, \mathbf{x}_2, \cdots, \mathbf{x}_\mathrm{N}) = -\Psi(\mathbf{x}_2, \mathbf{x}_1, \cdots, \mathbf{x}_\mathrm{N}) \tag{1.11}$$

where $\hat{\mathcal{P}}_{12}$ is the permutation operator and permutes the coordinates of electron 1 and electron 2. To write the wavefunction as both a Hartree product and an antisymmetric wavefunction you need linear combinations of Hartree products. Slater proposed the determinant Eq 1.9 as the way to systematically build a consistent antisymmetric wavefunction out of linear combinations of Hartree products.

Furthermore, each MO, χ, can be separated into a spatial component $\psi(\boldsymbol{r})$ and a spin component $\alpha(\omega)$ or $\beta(\omega)$ written as:

$$\chi(\mathbf{x}) = \begin{cases} \psi(\mathbf{r})\alpha(\omega) \\ \psi(\mathbf{r})\beta(\omega) \end{cases} \tag{1.12}$$

The spatial component $\psi(\boldsymbol{r})$ can be further broken down as a linear combination of atomic orbitals (LCAO), or basis functions, as shown in Eq 1.13.

$$\psi_i(\mathbf{r}) = \sum_{\mu=1}^{N_{basis}} C_{\mu i}\phi_\mu(\mathbf{r}) \tag{1.13}$$

where ϕ_μ are the basis functions, $C_{\mu i}$ the expansion coefficients, and N_{basis} the number of basis functions used in the expansion.

The Hartee Fock method approximates the electron-electron coulombic repulsion term in $\widehat{H}_e$ as the coulombic interaction of an electron with the average electrostatic potential produced by all the other electrons in the system. This effectively reduces $\widehat{H}_e$ to one body potentials for each electron in the system using the following definitions. The Fock operator $\hat{f}$ is defined as:

$$\hat{f}(1) = \hat{h}(1) + \sum_{j}^{N/2} 2\hat{J}_j(1) - \widehat{K}_j(1) \tag{1.14}$$

where $h(1)$ is the core Hamiltonian and contains the electron kinetic energy and electron-nuclear attraction operators defined as:

$$\hat{h}(1) = -\frac{1}{2}\nabla_1^2 - \sum_{A=1}^{M}\frac{Z_A}{\mathbf{r}_{1A}} \tag{1.15}$$

while $\hat{J}_j(1)$ is the coulomb operator, and represents the electrostatic repulsion between electron 1 and the average electrostatic potential of all the other electrons in orbitals *j* defined as:

$$\hat{J}_j(1)\chi_\mathrm{i}(1) = \left[\int \chi_j^*(2)\frac{1}{\mathbf{r}_{12}}\chi_j(2)\,d\mathbf{x}_2\right]\chi_\mathrm{i}(1) \tag{1.16}$$

$\widehat{K}_j(1)$ is the exchange operator and the result of using an anti-symmetrized wavefunction with no classical analog interpretation defined as:

$$\hat{K}_j(1)\chi_i(1) = \left[\int \chi_j^*(2)\frac{1}{\mathbf{r}_{12}}\chi_i(2)\,d\mathbf{x}_2\right]\chi_j(1) \tag{1.17}$$

Consequently, the restricted Hartree-Fock Energy expression can be written as:

$$\begin{aligned} E_{HF} &= \sum_{i=1}^{N}\langle\chi_i|\hat{h}(i)|\chi_i\rangle + \frac{1}{2}\sum_{i=1}^{N}\sum_{j=1}^{N}\langle\chi_i|\hat{J}_j(i)|\chi_i\rangle - \langle\chi_i|\hat{K}_j(i)|\chi_i\rangle \\ E_{HF} &= \sum_{i}\langle i|\hat{h}(i)|i\rangle + \frac{1}{2}\sum_{ij}[\langle ij|ij\rangle - \langle ij|ji\rangle] \\ E_{HF} &= 2\sum_{i}\left(i\middle|\hat{h}(i)\middle|i\right) + \sum_{ij}[2(ii|jj) - (ij|ji)] \end{aligned} \tag{1.18}$$

where Dirac's Bra-Ket notation with physicist and chemist notation for electron repulsion integrals has both used been used for electron repulsion integrals, and in the last step where we have integrated out spin and only spatial integrals involving $\psi_i(\mathbf{r})$ remain. One assumption that was made here was that the 2 electrons α and β have the same spatial orbital $\psi(\mathbf{r})$. This means that both α and β electrons are restricted to being in the same spatial location or orbital, hence the name restricted Hartree Fock.

The variational method can then be invoked to minimize the energy of Eq 1.18 with respect to the expansion coefficients $C_{\mu i}$. This results in E_{HF} being an upper bound to the true energy of the system. The outcome of this procedure is a pseudo-eigen value problem of the form:

$$\boldsymbol{FC} = \boldsymbol{SC\mathcal{E}} \tag{1.19}$$

where $\boldsymbol{C}$ is the expansion coefficients matrix, **S** is the overlap matrix with elements defined by:

$$S_{\mu\nu} = \langle\mu|\nu\rangle \tag{1.20}$$

and **F** is the Fock matrix with elements defined as:

$$\begin{aligned} F_{\mu\nu} &= \langle\mu|\hat{f}|\nu\rangle \\ &= \langle\mu|\hat{h}|\nu\rangle + \frac{1}{2}\sum_{\lambda\sigma}P_{\lambda\sigma}[2(\mu\nu|\lambda\sigma) - (\mu\sigma|\lambda\nu)] \\ &= H_{\mu\nu} + \sum_{\lambda\sigma}P_{\lambda\sigma}\left[(\mu\nu|\lambda\sigma) - \frac{1}{2}(\mu\sigma|\lambda\nu)\right] \\ &= H_{\mu\nu} + G_{\mu\nu} \end{aligned} \tag{1.21}$$

where we have introduced the density matrix $P_{\lambda\sigma}$ defined as:

$$P_{\lambda\sigma} = 2\sum_{j}C_{\lambda j}^*C_{\sigma j} \tag{1.22}$$

and where $G_{\mu\nu}$is the two-electron part of the fock matrix and defined as:

$$G_{\mu\nu} = \sum_{\lambda\sigma} P_{\lambda\sigma}\left[(\mu\nu|\lambda\sigma) - \frac{1}{2}(\mu\sigma|\lambda\nu)\right] \tag{1.23}$$

Eq 1.19 is commonly referred to as the Hartree-Fock-Roothan equation since Roothan proposed it as a way of solving the Hartree Fock equation.[10] A remaining with Eq 1.19 is that by using the atomic orbital (AO) basis we have ended up with a nonorthogonal equation that involves the overlap matrix **S**. In order to solve Eq 1.19, we need to orthogonalize the overlap matrix **S**, this is most commonly done using Löwdin symmetric orthogonalization, which involves using the overlap matrix **S**, as the transformation matrix **X** as follows:

$$\boldsymbol{X} = \boldsymbol{S}^{-\frac{1}{2}} \tag{1.24}$$

which allows use to define:

$$\boldsymbol{C'} = \boldsymbol{X^{-1}C} \tag{1.25}$$

$$\boldsymbol{C} = \boldsymbol{XC'} \tag{1.26}$$

$$\boldsymbol{F'} = \boldsymbol{X^{\dagger}FX} \tag{1.27}$$

resulting in:

$$\boldsymbol{F'C'} = \boldsymbol{C'\mathcal{E}} \tag{1.28}$$

Eq 1.28 can now be solved by diagonalizing $\boldsymbol{F'}$ and the resulting $\boldsymbol{C'}$ coefficient matrix can be back transformed using Eq 1.26.[11] Lastly, in this context, the Hartree Fock energy can then be recast and calculated using:

$$E_{HF} = \frac{1}{2}\sum_{\mu\nu} P_{\mu\nu}\left(H_{\mu\nu} + F_{\mu\nu}\right) \tag{1.29}$$

1.3 Density Functional Theory

Density functional theory (DFT) provides an alternative approach to solving the electronic structure problem. It is by far the most popular method for running electronic structure calculations. DFT asserts that all that is needed to solve for the ground state energy of a chemical system is the system's electron density $\rho(\boldsymbol{r})$.

$$\rho(\mathbf{r}) = N\int \Psi^*(\mathbf{r}, \mathbf{r}_2, \cdots, \mathbf{r}_n)\Psi(\mathbf{r}, \mathbf{r}_2, \cdots, \mathbf{r}_n)\, d\mathbf{r}_2 \cdots d\mathbf{r}_n \tag{1.30}$$

DFT states that this is because the energy of the system can be written as a functional of the electron density, $E[\rho]$. However, one of the biggest problems in DFT is finding the form of a universal functional, that can exactly determine the energy of all molecular systems.[12]

To show that this was possible Hohenberg and Kohn in their first theorem showed that the ground state density, $\rho(\mathbf{r})$, of a system is unique for a given external potential by reductio ad absurdum. This is because if the ground state density can uniquely determine

the external potential, then that defines the Hamiltonian along with its associated wavefunction and energy. Hohenberg and Kohn showed the connection between the density, $\rho(\mathbf{r})$, and energy E. They then followed up with a second theorem demonstrating that if you have many trial electron densities, each with their corresponding Hamiltonians, wavefunction, and energies then the electron density that corresponds to the lowest energy must be the correct density due to the variational principle of MO theory. This second theorem essentially connected the electron density $\rho(\mathbf{r})$ to a variational principle.[13]

While these Hohenberg-Kohn theorems made solving the electronic structure problem using the density, $\rho(\mathbf{r})$, possible it did not make it easier. In 1965 Kohn and Sham made the problem easier and practical by assuming that the ground state density of the system is for a system of non-interacting electrons. They crucially reintroduced molecular orbitals, ϕ_i also known as Kohn-Sham orbitals, which allows you to reconstruct the electron density as

$$\rho(\mathbf{r}) = \sum_{i}^{occ} |\phi_i(\mathbf{r})|^2 \tag{1.31}$$

consequently, you can accurately calculate the kinetic energy functional for a system of non-interacting electrons as

$$T_s[\rho(\mathbf{r})] = -\frac{1}{2}\sum_{i}^{occ} \int \phi_i^*(\mathbf{r})\nabla^2 \phi_i(\mathbf{r}) d\mathbf{r} \tag{1.32}$$

This then allows you write down the energy functional as:

$$J[\rho(\mathbf{r})] = \frac{1}{2}\int\int \frac{\rho(\mathbf{r})\rho(\mathbf{r}')}{|\mathbf{r}-\mathbf{r}'|} d\mathbf{r} d\mathbf{r}' \tag{1.33}$$

$$V_{Ne}[\rho(\mathbf{r})] = -\sum_{A}^{M} \int \frac{\rho(\mathbf{r})Z_A}{|\mathbf{r}-\mathbf{R}_A|} d\mathbf{r} \tag{1.34}$$

$$E[\rho(\mathbf{r})] = T_s[\rho(\mathbf{r})] + V_{Ne}[\rho(\mathbf{r})] + J[\rho(\mathbf{r})] + E_{xc}[\rho(\mathbf{r})] \tag{1.35}$$

where the first term is the non-interacting kinetic energy, the second is the electron-nuclear attraction potential, defined in Eq 1.34, the third is the electron-electron coulombic repulsion, defined in Eq 1.33 and lastly the final term is electron correlation energy. The electron correlation energy considers corrections due to the difference in the kinetic energy of the interacting and non-interacting electrons and any corrections to the coulombic repulsion due nonelectrostastic interactions like exchange.[12] However no explicit functional exists for E_{xc}

$$E_{xc}[\rho(\mathbf{r})] = (T[\rho] - T_s[\rho]) + (V_{ee}[\rho] - J[\rho]) \tag{1.36}$$

In order increase the accuracy of Kohn-Sham DFT several approximations to the exchange correlation functional, E_{xc}, have been made to better account for the exchange and correlation effects found in molecules. Some of these methods use the density, $\rho(\mathbf{r})$, its gradient, $\nabla\rho(\mathbf{r})$, and higher order derivatives of the density, $\nabla^2\rho(r)$, while others chose methods that used empirically fitted parameters.[12,14–19] As a conceptual framework many of these approximations to the exchange correlation functional are classified into one of five hierarchal rungs. Where the rungs refer to a ladder known as Jacob's ladder, with higher rungs offering more accuracy at higher computational cost. This ladder essentially serves as a guide from simple approximations towards complex and nonlocal approximations. Most DFT functionals approximations fall into one of the following classes listed from the simplest to the most complex approximations:

- The Local Density Approximation (LDA), is the simplest approximation where the functional only depends on the local density $\rho(\mathbf{r})$ and implements the exchange and correlation terms based off the uniform electron gas.[12,16]
- The Generalized Gradient Approximation (GGA), this is a semilocal approximation that takes into account the density $\rho(\mathbf{r})$ and its gradient $\nabla\rho(\mathbf{r})$ to correct for errors in the LDA approach for both the exchange and correlation.[14,15]
- The Meta-Generalized Gradient Approximation (Meta-GGA) this approximation again uses the density $\rho(\mathbf{r})$, its gradient $\nabla\rho(\mathbf{r})$, and its Laplacian $\nabla^2\rho(\mathbf{r})$ or kinetic energy density τ for the exchange and correlation to correct for errors further.[17]
- Hybrids functional mix a portion of semilocal exchange from the GGA approximation with nonlocal Hartree-Fock exchange into the exchange portion of functional. The ratio of GGA exchange to Hartree-Fock exchange varies depending on the functional.[17,18]
- Double Hybrids mix both exchange and correlation from the GGA approximation with Hartree-Fock exchange into the exchange portion of functional and with Moller-Plesset correlation into the correlation portion of functional.[19]

1.4 Time-Dependent Density Functional Theory

In the last sections we talked about methods suitable for studying molecules in the ground state. While molecules and their chemical properties in the ground state are essential, many chemical processes and reactions occur in the excited state. This makes it important to have scalable and reliable methods capable of studying excited states. While there are various excited state methods established in the literature for studying excited states such as Configuration Interaction Singles (CIS), Time-Dependent Hartree-Fock (TDHF), Equations-of-Motion Coupled Cluster (EOM-CC) and Time-Dependent Density Functional Theory (TD-DFT).[20–24] In what follows I will be focusing on TD-DFT since it is the most widely used method for studying excited states of molecules.

TD-DFT can be seen as an extension of Kohn-Sham DFT that allows for time dependent potentials such as electric and magnetic fields. TD-DFT is based off the Runge-Gross Theorem which is its foundational principal. The Runge-Gross theorem is a generalization of the Hohenberg-Kohn to allow for time-dependent potentials. Formally, the Runge-Gross theorem connects and forms a mapping between a time-dependent electron density, $\rho(\mathbf{r}, t)$ and the time-dependent external potential $v_{ext}(\mathbf{r}, t)$ up to a time a

constant time-dependent function. Meaning that the time-dependent potential $v_{ext}(\mathbf{r},t)$ can be uniquely determined by $\rho(\mathbf{r},t)$ as long as $v_{ext}(\mathbf{r},t)$ can be Taylor expanded around the initial time.[24] Analogously, to how Hohenberg-Kohn showed that $\rho(\mathbf{r})$ is the quantity of interest for DFT, $\rho(\mathbf{r},t)$ is the quantity of interest for TD-DFT.

Applying the Kohn-Sham formulation to the time-dependent Schrödinger equation leads to the time-dependent Khon-Sham (TDKS) equations,

$$i\frac{\partial}{\partial t}\phi_i(\mathbf{r},t) = \left(-\frac{1}{2}\nabla^2 + v_s(\mathbf{r},t)\right)\phi_i(\mathbf{r},t) \tag{1.37}$$

where $v_s(\mathbf{r},t)$ consists of the exchange-correlation potential, $V_{xc}[\rho]$, the Hartree potential, $V_H[\rho]$, and the external potential, $V_{ext}[\rho]$

$$V_{xc}[\rho(\mathbf{r},t)] = \frac{\delta A_{xc}[\rho(\mathbf{r},t)]}{\delta\rho(\mathbf{r},t)} \tag{1.38}$$

$$V_H[\rho(\mathbf{r},t)] = \frac{\delta J[\rho(\mathbf{r},t)]}{\delta\rho(\mathbf{r},t)} \tag{1.39}$$

$$V_{ext}[\rho(\mathbf{r},t)] = \frac{\delta V_{Ne}[\rho(\mathbf{r},t)]}{\delta\rho(\mathbf{r},t)} \tag{1.40}$$

where A_{xc} is the exchange-correlation action functional and $v_s(\mathbf{r},t)$ is defined as

$$v_s(\mathbf{r},t) = V_{ext}(\mathbf{r},t) + V_H(\mathbf{r},t) + V_{xc}(\mathbf{r},t) \tag{1.41}$$

The TDKS orbitals, $\phi_i(\mathbf{r},t)$, can then be used to build the time-dependent density $\rho(\mathbf{r},t)$ as follows

$$\rho(\mathbf{r},t) = \sum_{i}^{occ} |\phi_i(\mathbf{r},t)|^2 \tag{1.42}$$

and $v_s(\mathbf{r},t)$ allows us to study and compute excited states of molecules by applying a time-dependent electric field perturbation. Using first-order perturbation theory we can obtain the so-called Linear Response of the initial ground state density to the time dependent perturbation. The equations that arise out of applying first-order time-dependent perturbation theory to this perturbation are known as the Casida equations and are given by

$$\begin{bmatrix} \boldsymbol{A} & \boldsymbol{B} \\ \boldsymbol{B}^* & \boldsymbol{A}^* \end{bmatrix}\begin{bmatrix} \boldsymbol{X} \\ \boldsymbol{Y} \end{bmatrix} = \omega \begin{bmatrix} \mathbf{1} & \mathbf{0} \\ \mathbf{0} & -\mathbf{1} \end{bmatrix}\begin{bmatrix} \boldsymbol{X} \\ \boldsymbol{Y} \end{bmatrix} \tag{1.43}$$

where $\boldsymbol{X}$ and $\boldsymbol{Y}$ are the transition vectors and ω are the excitation energies. The $\boldsymbol{A}$ and $\boldsymbol{B}$ matrices for hybrid functionals are defined by

$$A_{ia,jb} = \delta_{ij}\delta_{ab}(\epsilon_a - \epsilon_i) + (ia|jb) - c_{HF}(ij|ab) + (1 - c_{HF})(ia|f_{xc}|jb) \quad (1.44)$$

$$B_{ia,jb} = (ia|bj) - c_{HF}(ib|aj) + (1 - c_{HF})(ia|f_{xc}|bj) \quad (1.45)$$

where i and j refer to orbitals in the occupied space and a and b refer to orbitals in the virtual space. Additionally, c_{HF} corresponds to the amount of Hartree-Fock exchange computed from the Kohn-Sham orbitals, ϕ_i, and ranges between 0.1- 0.4 corresponding to between 10% - 40% Hartree-Fock exchange. The Kohn-Sham orbitals ϕ_i and ϕ_a have corresponding energies ϵ_i and ϵ_a. The $(ia|jb)$ terms and its permutations refer to coloumb like two electron integrals. Lastly, f_{xc} is the exchange-correlation kernel and under the local density approximation for the exchange correlation can be defined as the second functional derivative of the exchange correlation energy given by

$$(ia|f_{xc}|jb) = \int \phi_i^*(\mathbf{r})\phi_a(\mathbf{r}) \frac{\delta^2 E_{xc}}{\delta\rho(\mathbf{r})\delta\rho(\mathbf{r}')} \phi_b^*(\mathbf{r}')\phi_j(\mathbf{r}')d^3\mathbf{r}\, d^3\mathbf{r}' \quad (1.46)$$

Solving the Casida equations is at the core of TD-DFT calculations because their solutions yield excited state energies and oscillator strengths which allows us to plot ultraviolet (UV) spectra and compute other derived excited state properties using these quantities.

Chapter 2

Computational and Mechanistic Analysis of Nitroso Compounds

"What the chemist has at hand always consists of substances, themselves made up molecules, containing defined number of atoms in ordered arrangements. Consequently, in order to synthesize anyone substance, his task is that of combining, modifying, transforming, and tailoring known substances, until the total effects of his manipulations is the conversion of one or more forms of matter into another."

-Robert Burns Woodward

2.1 Background

The nitroso (NO) functional group is found in several small molecules of biological and chemical importance (Figure 2.1). For instance, Lomustine, a small N-nitrosourea, is a therapeutic molecule which has been used to halt tumor growth as a potent DNA alkylator in various different cancers.[25] S-nitroso-N-penicillamine (SNAP) is a nitrosothiol known to be involved in cell signaling and antiproliferation.[26] While alkyl nitrates such as, nitroglycerin are used as vasodilators[27] and alkyl nitrites such as amyl nitrate are used as treatment for cyanide poisoning.[28] Additionally, molecules with heteroatoms-NO or R-NO_2 bonds are efficient donors of gaseous nitric oxide (NO) in biological systems. Organic compounds capable of delivering NO in-situ by direct bond cleavage make it an effective way to deliver NO. Additionally, nitric oxide's poor water solubility makes an organic compound a good way to deliver NO and study NO pathways in the body.[29,30] Furthermore, while Lomustine is a therapeutic compound its structurally similar Semustine is a known DNA alkylator carcinogen with only one methyl group difference in their chemical structure (Figure 2.2). This drastic difference between a therapeutic and a carcinogen in their biological profile implies a sensitive structure-activity relationship that needs to be further explored in nitrosated compounds.

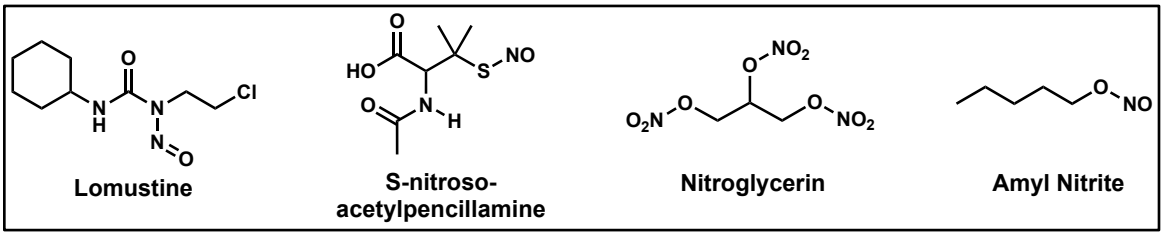


Figure 2.1 Biologically active nitroso compounds

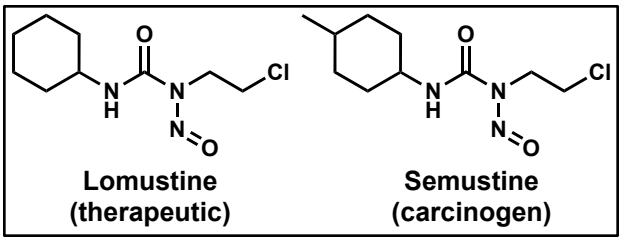


Figure 2.2 N-nitroso urea's structural activity relationship

Currently, many of the synthetic methods available to synthesize nitrosated compounds required harsh conditions such as strong Bronsted or Lewis acids with inorganic nitrites[31]. For example, synthesis of N-nitroso compound usually involves an inorganic nitrite such as sodium nitrite in the presence of a lewis acid (Figure 2.3).[32,33] The nitrite anion and the lewis acid then react to give a nitrosonium cation (NO^+) in situ, a really strong electrophile, that is then attacked by the corresponding nitrogen nucleophile to give the N-nitroso product (Figure 2.4).[34] Unfortunately, these low pH conditions limit the scope of substrates that can be effectively used. Similary alkyl nitrites

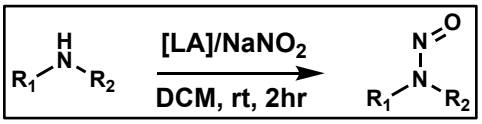


Figure 2.3 N-nitroso compound synthesis

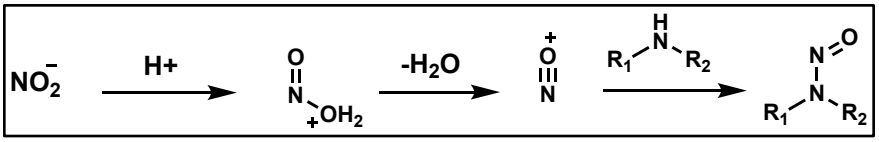


Figure 2.4 N-nitroso compound synthesis Mechanism

To remedy this issue, a new reagent, *tert*-butyl nitrite (TBN), was introduced as a new electrophilic source of NO. Fortunately, TBN does not require strongly acidic conditions for transnitrosation, but it does require excess amounts to minimize reversible transnitrosation with itself and certain nucleophiles (Figure 2.5).[35] Additionally, TBN is known to be air-sensitive due to experiencing autooxidation and homolytic thermolysis at room temperature. To avoid TBN drawbacks, it must be stored under low temperatures and an inert atmosphere.[36]

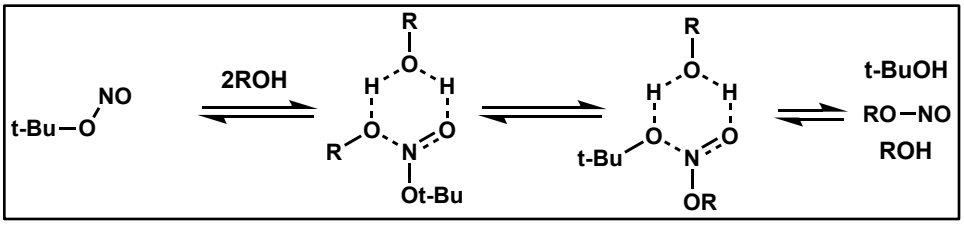


Figure 2.5 TBN equilibrium with alcohols

2.2 A New Reagent for Transnitrosation

To address the downfalls of TBN, we developed a new organic reagent as an alternative for transnitrosation under mild conditions. N-nitrososulfonamide (NO-1) is a solid crystalline transnitrosation stable reagent (Figure 2.6).[37]

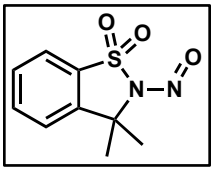


Figure 2.6 N-nitrososulfonamide (NO-1) Reagent

While we were establishing the reactivity profile of NO-1 we found discrepancies in the yields of transnitrosation obtained when using different synthesized batches of NO-1.[38] Upon further investigation using x-ray crystallography, we discovered that there were two different rotational configurations of the NO-1 reagent. The crystal structure of the batch of NO-1 that gave reproducible results was NO-1a and the crystal structure of the batch of NO-1 that gave irreproducible results contained a mixture of both NO-1a and NO-1b (Figure 2.7). The crystallography data showed that both NO-1a and NO-1b are rotational isomers and that they were both present in the batch with inconsistent yields, but only NO-1a was present in the batch with consistent yields.

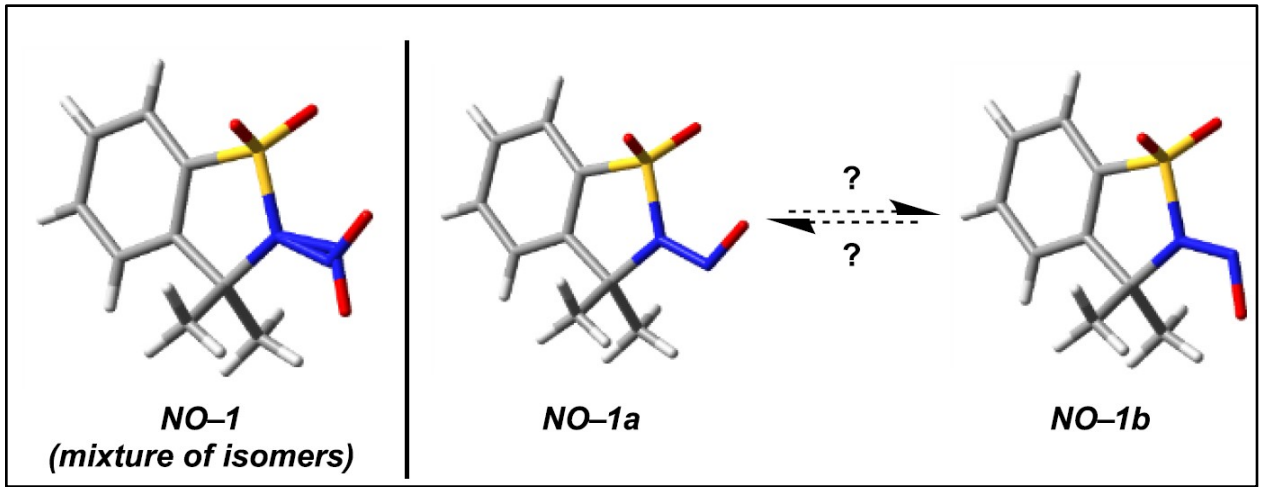


Figure 2.7 X-Ray Crystal Structure of NO-1 as a mixture of rotamers NO-1a and NO-1b (LEFT). The structures of NO-1a and NO-1b and interconversion between the two (RIGHT).

As shown in Figure 2.7, a poorly performing batch of NO-1 exists as a mixture of stable rotational isomers centered around the N−N−O bond. Superimposed structures show that the molecular geometry is nearly identical throughout both isomers, beyond the orientation of the nitroso N−O bond. Interestingly, while ineffective at room temperature, this batch of NO−1 was still capable of transnitrosation to produce some products in high yields at elevated temperatures. This suggested either that both isomers were sufficiently

reactive at an elevated temperature or that thermally induced conversion to a single active rotamer was occurring.

To better understand the possibility of thermal interconversion between stable rotational isomers, we computed a potential energy scan of NO−1 along the S−N−N−O dihedral angle (Figure 2.8, red data). Initial results confirmed that structure NO−1a was lower in energy than NO−1b by approximately −1.2 kcal/mol (0°and 180° dihedral angles, respectively in Figure 2.8). Interestingly, different rotational barriers were calculated when rotating between 0° and 120° than from 180° to 290°. Discontinuities in the potential energy scan were also noted between 130° to 140° and 290° to 300°, which suggested a change in the ground-state electronic structure and warranted further investigation. Upon analyzing the geometries of NO−1 at each data point along the potential energy scan, we noted geometry/hybridization changes of the nitrogen atom within the ring.

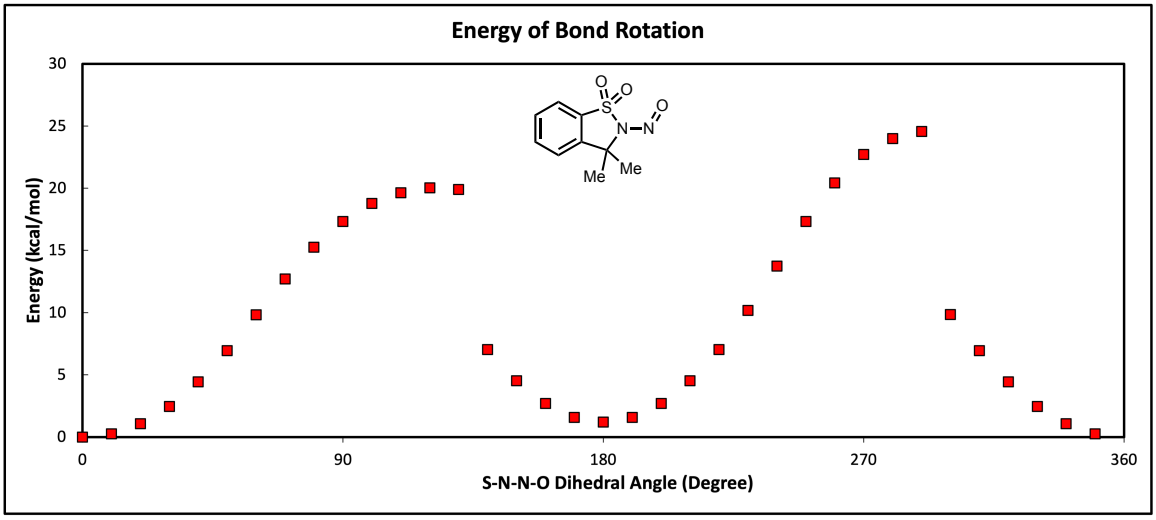


Figure 2.8 Relaxed potential energy scan of NO-1 using the S-N-N-O dihedral angle (RED). The scan rotates the S-N-N-O dihedral angle at ten degree intervals and reoptimizes the NO-1 energy at the new geometry. The relaxed energy scan is performed using DFT with the B3LYP functional, basis set 6-311+G(2d,p) and the PCM solvent model with acetonitrile.

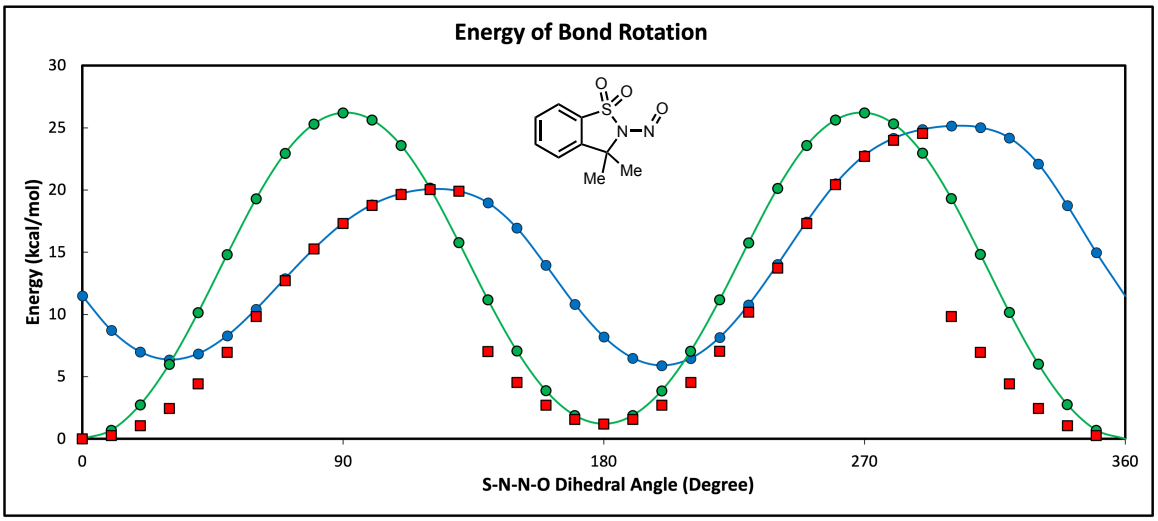


Figure 2.9 Relaxed potential energy scan of NO-1 using the S-N-N-O dihedral angle (RED). Constrained sp^2 NO-1 PES using S-N-N-O dihedral angle (GREEN). Constrained sp^3 NO-1 PES using S-N-N-O dihedral angle (BLUE).

To further investigate this change in hybridization along the scan coordinate, we computed two additional potential energy scans with geometric constraints that imposed either sp2 or sp3 hybridization at the nitrogen in the ring (Figure 2.9, green and blue data, respectively). As shown in Figure 2.9, the observed discontinuities in the initial scan (Figure 2.8, top panel) were confirmed to result from changes in electronic states. Specifically, the different electronic states correspond to different hybridizations, sp2 and sp3, of the nitrogen in the ring that are induced by geometric changes of NO−1. Overlap of the red data with either the blue or green curves indicates the hybridization of the energy-minimized structure at a particular dihedral angle. Lack of overlap, coinciding with discontinuities in the unrestricted data (red), indicates a geometry that does not fit neatly into the limiting definitions of sp2 or sp3 hybridization.

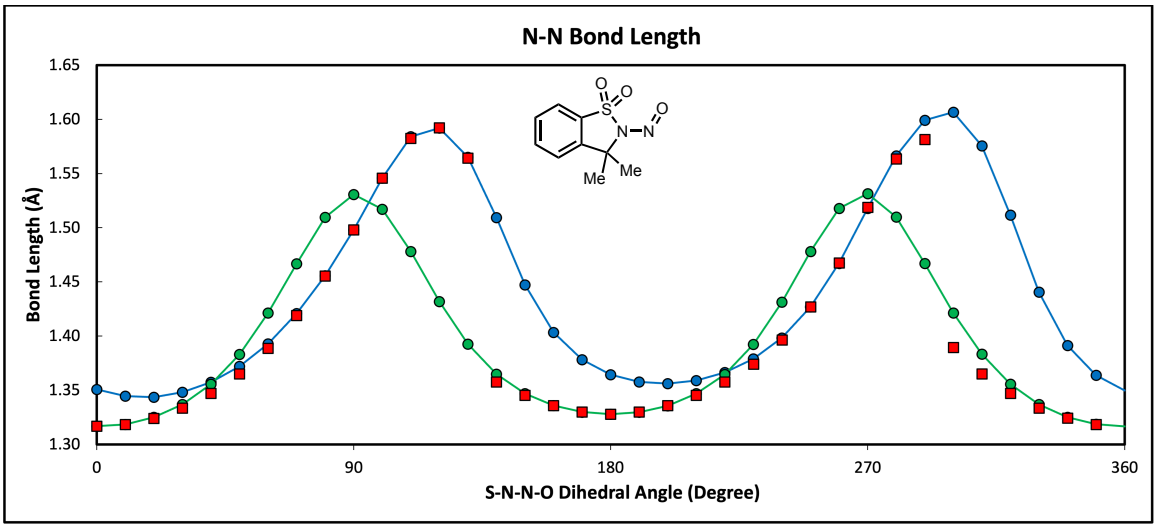


Figure 2.10 Nitrogen-Nitrogen bond length scan of NO-1 using the S-N-N-O dihedral angle (RED). Constrained sp^2 NO-1 PES using S-N-N-O dihedral angle (GREEN). Constrained sp^3 NO-1 PES using S-N-N-O dihedral angle (BLUE).

To corroborate these results, we also looked at the nitrogen-nitrogen bond distance. Figure 2.10 demonstrates how the nitrogen-nitrogen bond distance of NO-1 changes as the S-N-N-O dihedral angle of NO-1 is rotated. As before we also did this for the sp^2 and sp^3 geometrically constrained variants of NO-1. As we can see in Figure 2.10 when NO-1 is in the NO-1a confirmation, the nitrogen-nitrogen bond length overlaps with the sp^2 constrained curve. Furthermore, we then again see that as the S-N-N-O dihedral angle is scanned, NO-1 changes hybridization from sp^2 to sp^3. This identifies the resonance structure of the sp^2 hybridized NO-1 as having a nitrogen-nitrogen double bond due to the shorter bond length and the sp^3 hybridized structure of NO-1 having a nitrogen-nitrogen single bond.

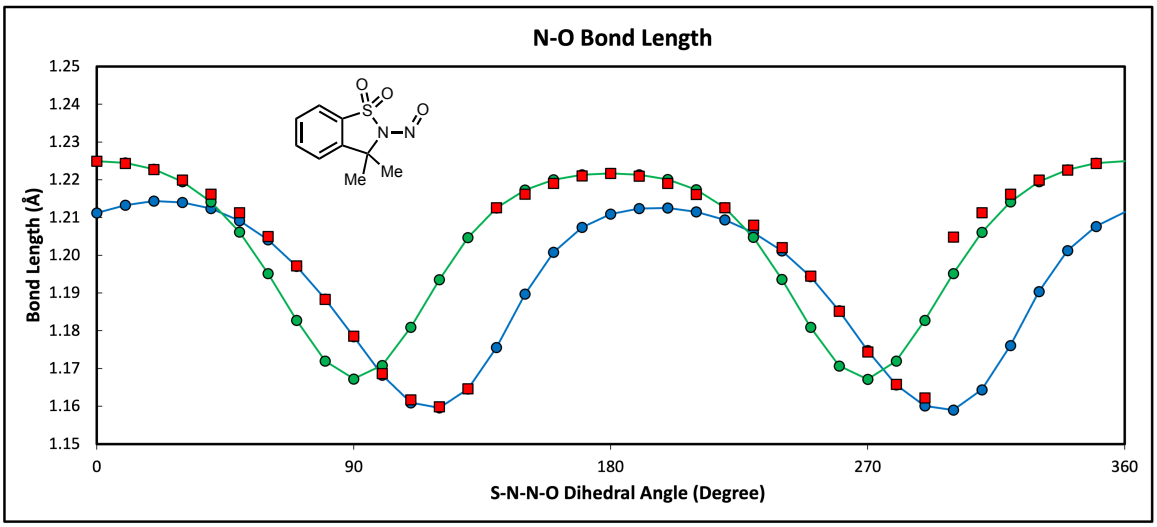


Figure 2.11 Nitrogen-Oxygen bond length scan of NO-1 using the S-N-N-O dihedral angle (RED). Constrained sp^2 NO-1 PES using S-N-N-O dihedral angle (GREEN). Constrained sp^3 NO-1 PES using S-N-N-O dihedral angle (BLUE).

Other bond lengths that can verify the resonance structures of the sp^2 and sp^3 structures are the nitrogen-oxygen bond length in the nitroso group and the sulfur-oxygen bond of the sulfonyl group. This is because the sulfonyl, nitroso, and the nitrogen-nitrogen bond are all conjugated. Therefore, changing the length or hybridization of one group affects the others. Figure 2.11 shows us that as NO-1's S-N-N-O dihedral angled is rotated the nitrogen-oxygen bond length begins elongated, overlapping with sp^2 curve, as the dihedral angle is scanned it overlaps with the sp^3 curve and the bond length shortens. This behavior then repeats at around 130°, where we see the change in hybridization change back to the sp^2 curve. The same trend but in reverse, is observed with the sulfur-oxygen bond length as can be seen in Figure 2.12. In this case, the NO-1 sulfur-oxygen bond length begins small and grows as its overlap with the sp^3 curve increases. Both of the former dihedral scans provide strong evidence for NO-1a being in the sp^2 hybridized resonance structure in the active form of NO-1a.

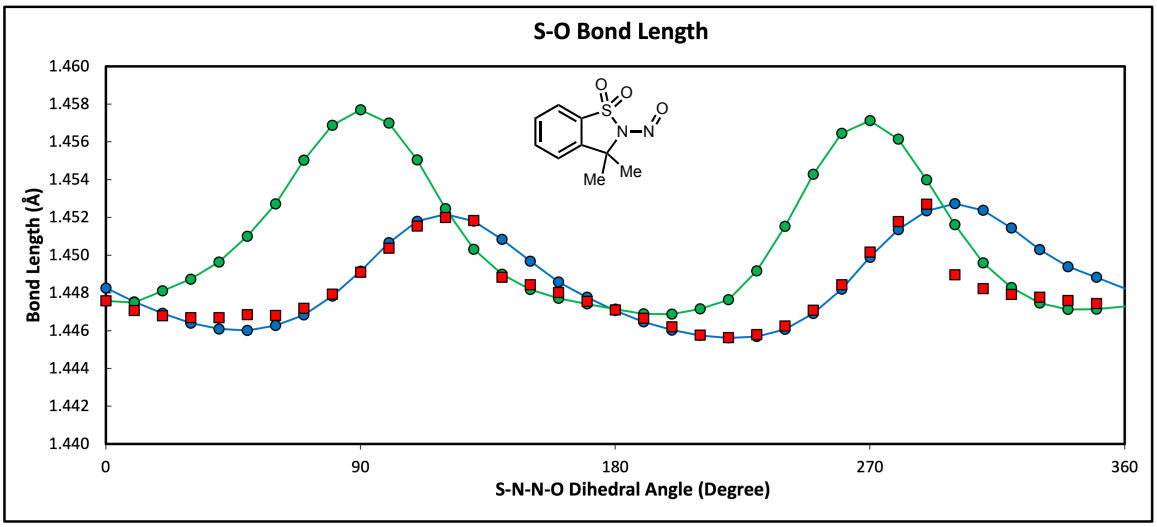


Figure 2.12 Sulfur-Oxygen bond length scan of NO-1 using the S-N-N-O dihedral angle (RED). Constrained sp^2 NO-1 PES using S-N-N-O dihedral angle (GREEN). Constrained sp^3 NO-1 PES using S-N-N-O dihedral angle (BLUE).

We also went ahead and compared the results of the Integral Equation Formulation Polarizable Continuum Model (IEF-PCM or PCM) for the acetonitrile solvent from Figure 2.13 against Solvent Model Density (SMD) method. While the PCM model does well taking into account electronic effects it does not take into account non-electrostatic solvation effects such as cavitation, dispersion, and structural rearrangement of the solvent. This is why the SMD solvation model was employed since it takes into account both electronic and non-electronic solvation effects.

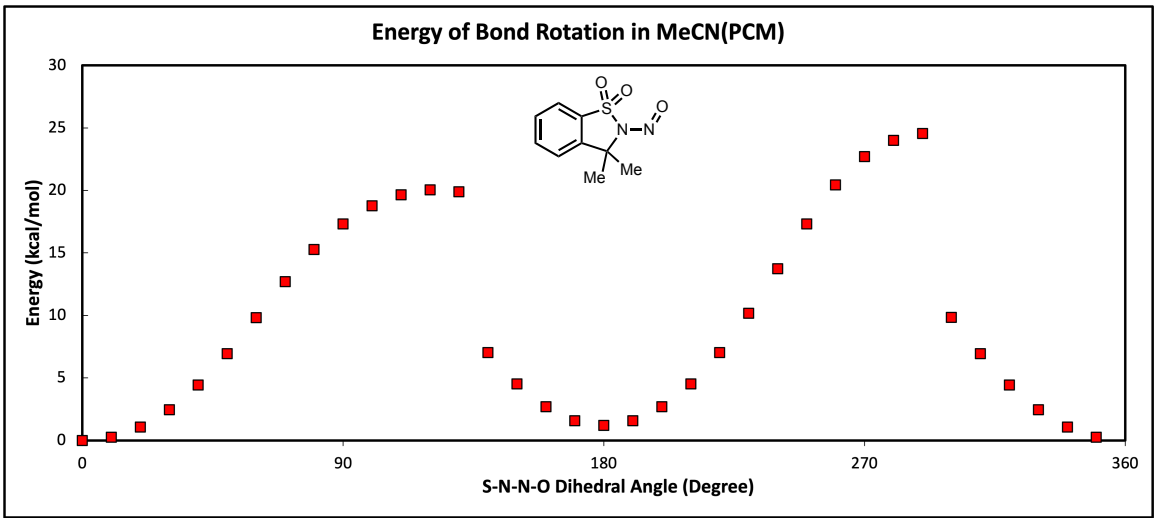


Figure 2.13 Relaxed dihedral energy scan of NO-1 performed using DFT with the B3LYP functional, basis set 6-311+G(2d,p), and the PCM solvent model with acetonitrile.

As can be seen when comparing Figure 2.13 and Figure 2.14 SMD solvation model is able to replicate the energy barriers of the PCM model and has the same general characteristics.

Since the SMD solvation model was able to recreate the general energy profile of the PCM model, we went ahead and used SMD going forward since it can capture both electrostatic and non-electrostatic solvation effects. These results further strengthen our belief that the SMD was able to obtain similar or more accurate results than those produced by the PCM solvation model.

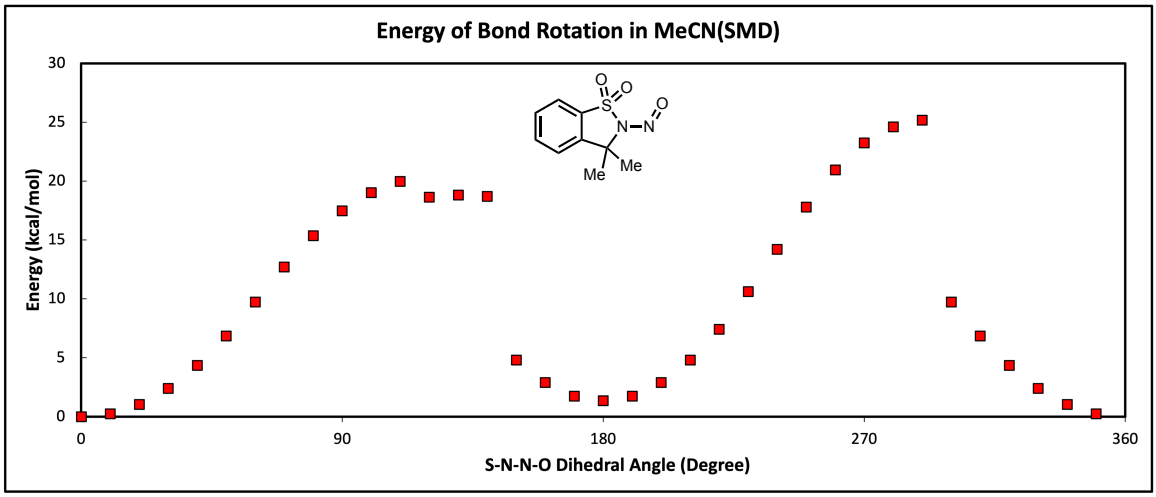


Figure 2.14 Relaxed dihedral energy scan of NO-1 performed using DFT with the B3LYP functional, basis set 6-311+G(2d,p), and the SMD solvent model with acetonitrile.

Experimental efforts then confirmed that NO−1a is the active rotational isomer for transnitrosation at room temperature. Simply heating a crude mixture of NO−1 to 80 °C as a final step in the synthesis yields a reagent that consistently transnitrosates at room temperature and a crystal structure consistent with NO-1a. Efforts to identify the source of disparate reactivity between NO−1a and NO−1b at room temperature are ongoing.

2.3 Second Generation Transnitrosation Reagents

In order to create a reagent that could transnitrosate repeatedly and efficiently we began working on new nitrosation reagents. Our hypothesis was that if we could favor the NO-1a confirmation over the NO-1b then we would have a reliable reagent. To accomplish this, we proposed modifying the alkyl groups of NO-1. We hypothesized that by modifying the alkyl groups of NO-1 to bigger and bulkier groups, it will make the NO-1b rotamer higher in energy or increase the energy barrier for intercoversion between the two rotamers. This change in relative energies or energy barriers would lead to the NO-1a rotamer being the preferred configuration.

To test this hypothesis, we decided to look at three new analogs where the methyl groups of NO-1 were replaced with ethyl, phenyl, and isopropyl. For all the 3 analogs we analyzed the relaxed energy scan of the S-N-N-O dihedral using the SMD solvation model in the acetonitrile solvent.

2.3.1 Diethyl NO-1 Analog

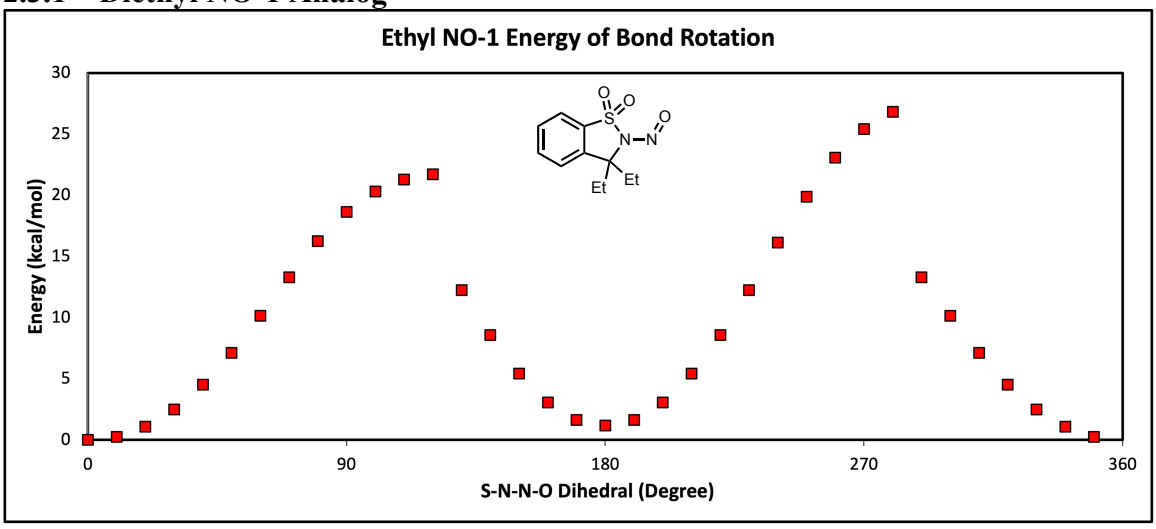


Figure 2.15 Relaxed dihedral energy scan of DiethylNO-1 performed using DFT with the B3LYP functional, basis set 6-311+G(2d,p), and the SMD solvent model with acetonitrile.

We began with the Diethyl group since we believed it was the next logical choice for increasing the steric hinderance in the NO-1b confirmation. The data in Figure 2.15 showed us that the energy difference between the NO-1a and NO-1b rotamers was only 1.17 kcal/mol. This was similar to what was seen before in Figure 2.14 where difference in energy between the two rotamers was 1.36 kcal/mol. The two energy barriers in Figure 2.14 were also 19.9 kcal/mol and 23.8 kcal/mol respectively. Compared with the energy barriers in Figure 2.15 of 21.7kcal/mol and 25.6kcal/mol respectively. These energy values told us that the NO-1b was more stabilized by the diethyl groups due to the smaller energy difference between the two rotamers. Interestingly though we see an increase in the barrier heights making interconversion between more difficult.

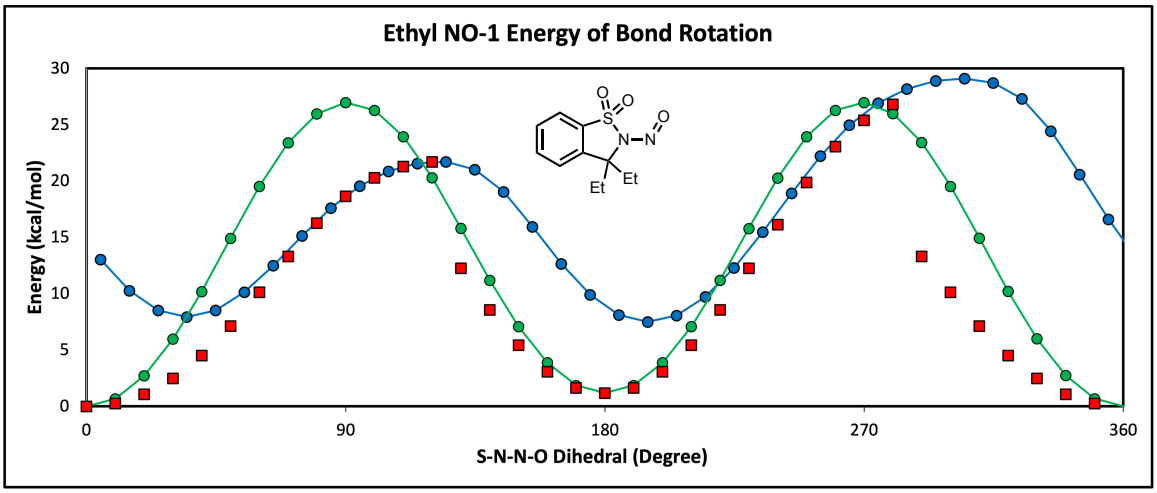


Figure 2.16 Relaxed potential energy scan of DiethylNO-1 using the S-N-N-O dihedral angle (RED). Constrained sp^2 DiethylNO-1 PES using S-N-N-O dihedral angle (GREEN). Constrained sp^3 DiethylNO-1 PES using S-N-N-O dihedral angle (BLUE).

We also wanted to know if we could confirm the identity of the active resonance structure. Figure 2.16 shows the same analysis we performed before follows the same trend as before. DiethylNO-1 begins overlapping with the sp^2 curve and gradually changes hybridization and overlaps with the sp^3 curve as the S-N-N-O dihedral angle is rotated. This analysis confirmed that diethylNO-1 has the same resonance structures as NO-1 and results in the same rotamer confirmations with the only difference being in relative rotamer energies and energy barriers. However, since we didn't observe the drastic difference in relative energies or energy barriers we went ahead and tried larger groups.

2.3.2 Diphenyl NO-1 Analog

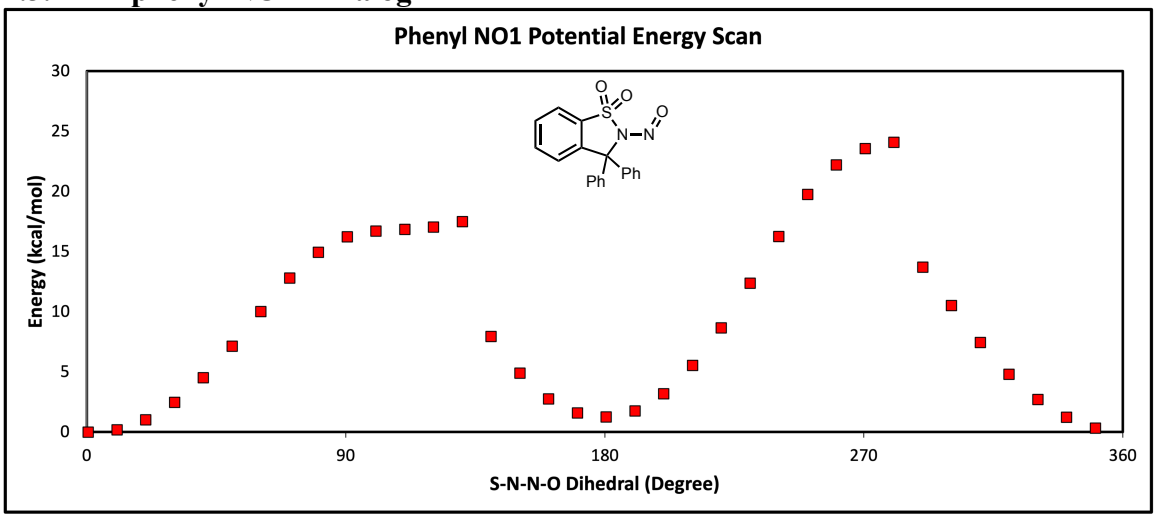


Figure 2.17 Relaxed dihedral energy scan of DiphenylNO-1 performed using DFT with the B3LYP functional, basis set 6-311+G(2d,p), and the SMD solvent model with acetonitrile.

Our next analog was the diphenylNO-1, we believed since the diethyl groups weren't bulky enough to cause a significant difference then phenyl groups would because a large change in the energetics due to their large size. Figure 2.17 shows the results of the diphenylNO-1 energy scan. We observed a relative rotamer energy difference of 1.26 kcal/mol with energy barrier heights of 17.5 kcal/mol and 22.8 kcal/mol respectively. While the rotamer energy differences and energy barrier heights were closer to NO-1 we still did not observe the drastic rotamer energy differences we hypothesize.

2.3.3 Diisopropyl NO-1 Analog

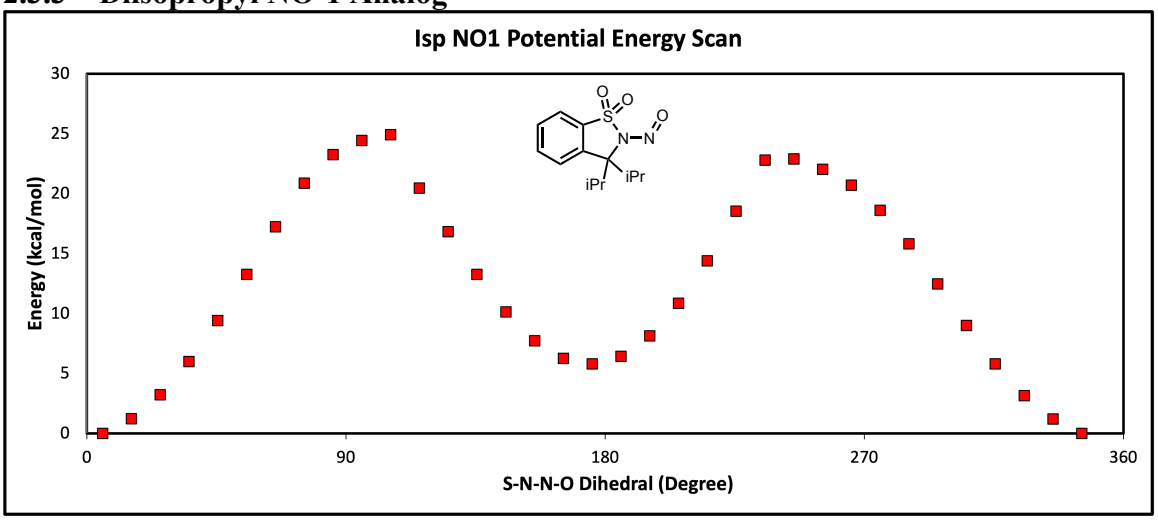


Figure 2.18 Relaxed dihedral energy scan of DiisopropylNO-1 performed using DFT with the B3LYP functional, basis set 6-311+G(2d,p), and the SMD solvent model with acetonitrile.

Our final NO-1 analog was a diisopropylNO-1 the results of the energy scan are presented in Figure 2.18. The scan shows a 6.19 kcal/mol rotamer energy difference and energy barrier heights of 25.3 kcal/mol and 17.1 kcal/mol respectively. These numbers demonstrated the drastic energy difference we hypothesized. The energy curve shows a large difference in the rotamers stabilization with preference for the diisopropylNO-1a rotamer. Additionally, the barrier height increased intensely compared to NO-1, decreasing interconversion between the two rotamers.

2.4 Conclusion

We have reported the invention of a new reagent for transnitrosation under mild conditions. This reagent, nitrosates nucleophiles irreversibly, and is straightforward to regenerate from the byproducts of a successful reaction. Mild rection conditions make this an ideal reagent to explore nitrosated molecules that are challenging, or impossible, to make via traditional methods. Two rotational isomers of NO−1 are stable at room temperature, although theoretical and experimental data suggest a single isomer (NO−1a) is active for transnitrosation.

Furthermore, we were able to design a second-generation version of the reagent with better energetic properties than the first reagent that should be able to overcome the synthetic limitation we observed with the first-generation regent. Future work will involve synthesis of the newly designed reagent, further exploration of molecules that can be nitrosated by NO−1 and diisopropylNO-1, and identification of features that favor reaction from NO−1a rotamer at room temperature.

Chapter 3

Organic Photophysics of Benzoyl Pyrazinium Salts

"I therefore take the liberty of proposing for this hypothetical new atom, which is not light but plays an essential part in every process of radiation, the name photon."

-Gilbert Newton Lewis

3.1 Background

Luminescent materials have found important applications in areas such as biosensing, imaging, environmental sensing, and display technology.[39–43] In order to keep up with the demand, materials that are inexpensive, scalable, synthetically accessible, and tunable are needed.[41,42] Organic molecules in particular have been shown to be one such class of materials, capable of tunable photophysical properties from first principles.[44–47] Understanding intramolecular charge transfer is important for the design of materials with applications in solar cells, photocatalysis, and fluorescent probes.[44] For instance in photoredox catalysis an understanding of the excited state's multiplicity and charge transfer can approximate properties such excited state lifetimes and quantum yields which in turn can determine whether a reaction can undergo a photoinduced electron transfer or an electron energy transfer pathway.[48]

Excited state characterization such as intramolecular charge transfer (CT) involves an electron transfer that occurs when a compound is irradiated with light. This causes an electronic excitation from a donor group in the molecule to the acceptor group in the molecule. This change in the distribution of the electron density in the excited state is what enables and gives rise to photophysics and photochemistry that is not possible in the ground state. For example, transition metal complexes such as $Ru(bpy)_3^{2+}$ are used as photocatalyst in organic chemistry due to their ability to performing a metal to ligand charge transfer (MLCT). This CT allows the complex to be in an excited state and perform single electron transfer (SET) chemistry, act as oxidant, or reductant.[49] Reactions that make use of excited charge transfer complexes are able to perform reductions of olefins, reductive dehalogenations, aerobic oxidative of benzylic halides and oxidative biaryl couplings. Furthermore, analysis of the type of CT and excited sate allows chemists to understand and tune the properties of interest such as emission wavelengths, excited state lifetimes, or chemical transformations.[49,50]

Small organic compunds are another well know class of photocatalyst that make use of CT excited states. Some common classes of organic photocatalyst are cyanoarenes, benzophenones, quinones, and pyriliums. Organic photocatalyst's diverse range of photophysical properties such as absorbption wavelengths, excited state lifetimes, emission wavelengths, and quantum yields make them a diverse set of compounds which can

modulate their photoreactivity. These properties are all dependent upon the characterization of the excited state such as CT excited states which allows them to perform photoinduced electron transfers (PET). This excited state allows them to perform reactions such as oxidative aminations, oxidative cycloadditions, peroxidation cyclizations, aromatic C-H oxidations and many more.[48] This why in this work we present structural design principles and rationale for enhancing charge transfer states when studying benzoyl pyraziniums salts.

A well-known and established strategy for tuning the photophysical properties of a molecule is by designing large conjugated-π systems and tuning the electronics.[45] This is achieved by varying the electron-donating groups and electron-withdrawing groups on the chromophore. While electronics are usually invoked for photophysical transitions it is important to distinguish between their different effects since they are not the same. Resonance delocalization is an electronic effect that occurs when there is direct conjugation between the donor and acceptor group and as a result there is electronic delocalization between the two groups. While the inductive effect is due to bond polarization or nonuniform distribution of electron density in a compound as result of differences in electronegativity. In this work we test various hypothesizes for designing compounds and enhancing the CT character which gives rise to the photochemical cyclization of benzoyl pyrazinium salts.

3.2 Observations

Baxter and coworkers have proposed an aza-Nazarov intramolecular photocyclization reaction that transforms benzoyl methyl pyrazinium tetrafluoroborate salts to polycyclic pyrazino[1,2-a]Indoles under monochromatic light.[51] While both the reactant and photocyclized product are photoluminescent it is unclear what is the origin of these photophysical properties. While similar cyclized products have been reported, reaction side products have previously hindered the understanding of the photosensitivity of benzoyl pyrazinium analogs.[50,52,53] Baxter and coworker's study showed that structural modification of benzoyl pyrazinium's pre and post cyclization gave rise to varied and desirable optical spectral properties making it a design strategy for fine tuning absorption and fluorescence of these compounds. To better understand the photophysics of this chemical transformation the absorption of the benzoyl pyrazinium reactant and analogs is modeled to derive insight into their photochemistry.

The report claims benzoyl pyrazinium salts under monochromatic 280 nm light undergo an irreversible intramolecular photocyclization. This suggest that the reaction is thermally inaccessible and photoinitiated. Also, many of their analogs of the benzoyl pyrazinium exhibit variable quantum yields and suggesting different absorption profiles due to the chemical modification. In the case of the unmodified benzoyl pyrazinium (Figure 3) they also mention a drastic difference in the time for photocyclization between 6 to 1 hour when using 280nm and 365nm light respectively. This suggests different excited states may play role in the reaction. Effects due to intermolecular interactions were also invoked as a justification for the difference in reaction time due to differences in reaction

concentration. In order to better understand the nature of this photochemical cyclization we computationally computed the UV-Vis spectrum of this compound. The computationally computed spectrum is well in agreement with the experimentally obtained spectrum. This suggests that the level of theory and model chemistry used was accurate for this system and spectroscopy.

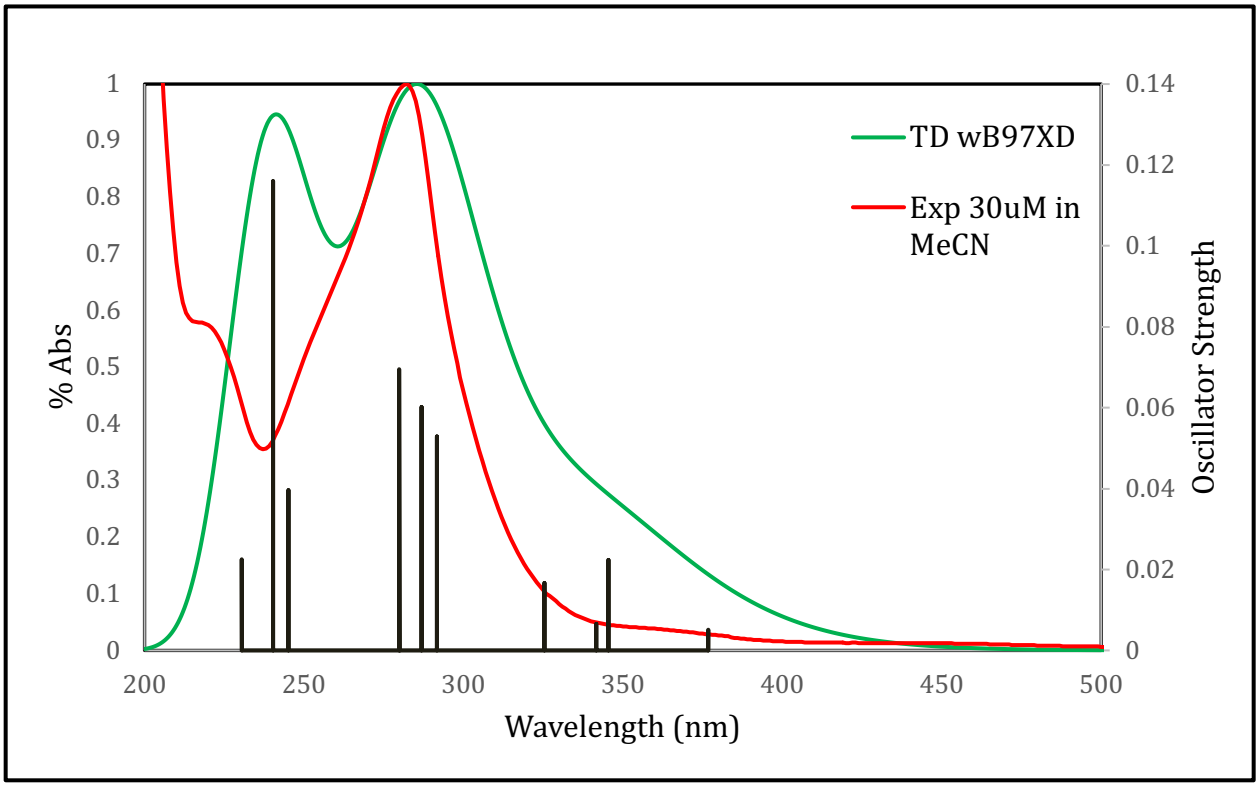


Figure 3.1 UV-Vis Absorption spectrum of Benzoyl Pyrazinium

The UV-Vis spectrum (Figure 3.1) also suggests that the excited state of interest is excited state 7, since it is the excited state with the largest oscillator strength (f = 0.07) at the same energy (E = 279nm) of light (E=280nm) used for the photocyclization. Further analysis was performed on excited state 7 in order to characterize it. To thoroughly characterize the excited state, we performed Natural Transition Orbitals (NTOs) analysis[54] (Figure 3.2). The particle hole pair NTOs of excited state 7 revealed a high degree of charge transfer (CT). This is due to localization of the hole orbital on the benzoyl fragment and the localization of the particle orbital on the pyrazinium fragment. To validate this finding we visualized the difference density between excited state 7 and the ground state to confirm CT was occuring. The difference density map in (Figure 3.3) strongly supports that excited state 7 is a CT state. This is due to the movement of electron density in the ground state on the benzoyl fragment to the pyrazinium fragment in excited state 7. All of this data leads us to believe that excited state 7 is a CT transfer state and responsible for the first peak in the UV-Vis spectra.

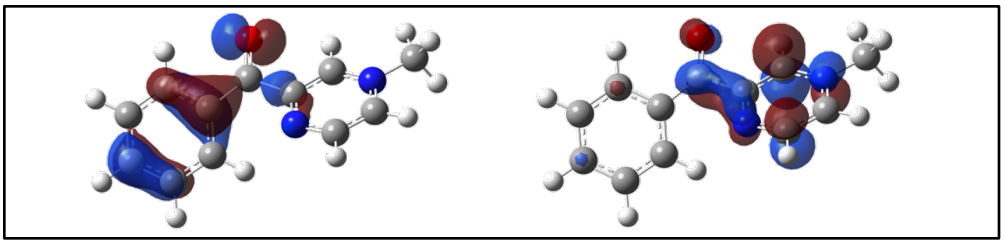


Figure 3.2 Hole and Particle NTOs for Benzoyl Pyrazinium Excited State 7

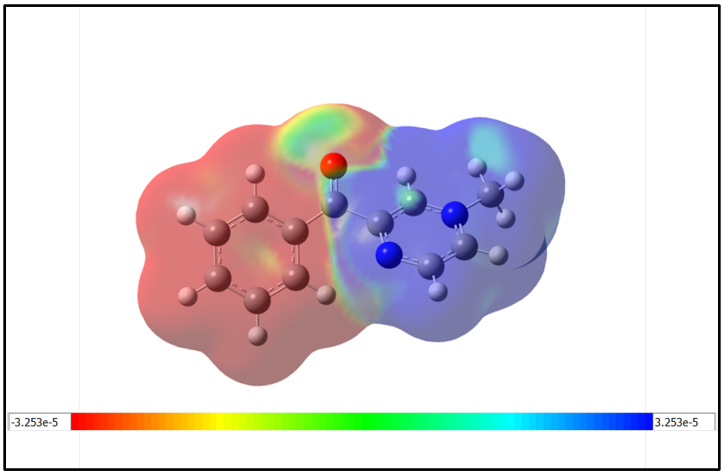


Figure 3.3 Benzoyl Pyrazinium Difference Density between ground state and 7th excited state

While all of this analysis is strong evidence for a CT state it does not quantify the degree of CT. In order to quantify CT many metrics have been proposed[55–57], our method for quantifying the amount of charge transfer uses the one-electron transition density matrix (1TDM). This is due to the pioneering work of Plasser and coworkers.[58,59] The analysis of the 1TDM through the TheoDORE package developed by Plasser and coworker allows for quantifiable descriptors derived from the 1TDM between the ground state and excited state of interest. The descriptors which reveal the most insight in our analysis was the CT number and CT distance (RMSeh). The CT number is a measure of how much change in electron density there is between defined fragment groups in the molecule. The CT distance is a measure of separation between the particle and hole densities as defined by the 1TDM on each fragment. The TheoDORE analysis was performed by partitioning the compound into two fragments (Figure 3.4). The first fragment is the Benzoyl group and any substituents attached to the benzene ring. This fragment will account for any local excitation in the benzene and carbonyl group side of the molecule. The second fragment contains the the pyrazinium ring and any substituents that may be attached to the ring. This fragment will capture any local excitations on the pyrazinium side of the molecule. This partitioning is necessary in order to be able to assign a CT number between different regions in the compound. Lastly, this method is very versatile as the exciton analysis can be performed with any quantum chemical method that produces an excited state density coefficient matrix.

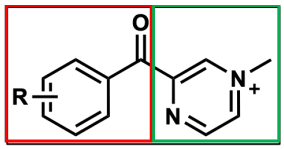
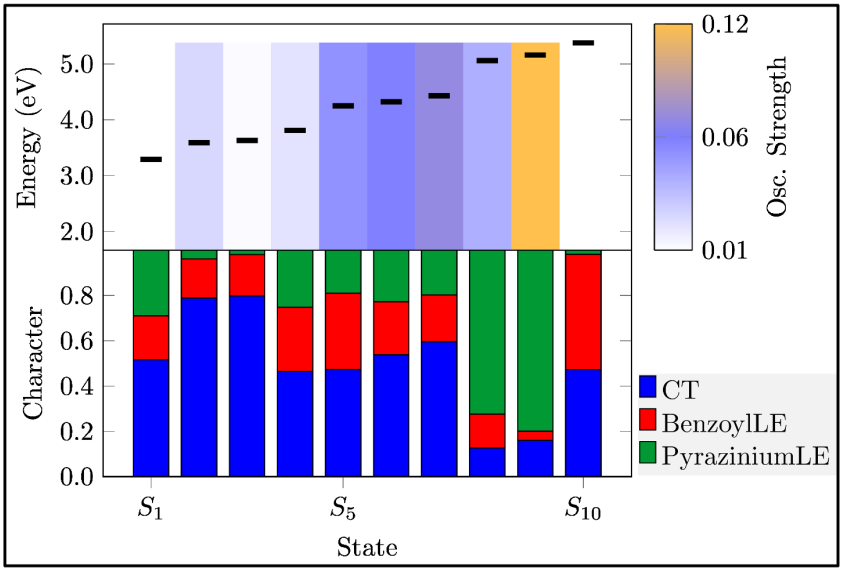


Figure 3.4 Pyrazinium Partioning Scheme for Theodore Analysis

The Theodore analysis of the Benzoyl Pyrazinium (**Error! Reference source not found.**) strongly supports our previous findings that excited state 7 has a strong oscillator strength at 279nm (4.4eV) and that excited state 7 is a CT state. Additionally, however we now have the CT number of 0.59 which is a measure of how much charge transfer there is between the benzoyl group and the pyrazinium group. Furthermore, the excited state analysis allows us to determine precisely the amount local excited state character versus CT character as defined by the fragments in the molecule.



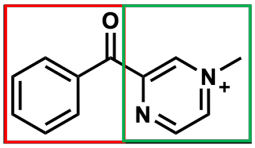


Figure 3.5 Benzoyl Pyrazinium Theodore Analysis Results

To probe if the CT property was only present in the benzoyl pyrazinium we also looked at a model system, which we referred to as benzoyl pyraziniumH which is just a protonated instead of methylated benzoyl pyrazinium. When performing the TheoDORE analysis on the Benzoyl PyraziniumH (Figure 3.7) we can see once again that excited state 7 has a large oscillator strength at 289nm (4.29eV) which is within the accessible energy range of the light source of 280nm. Furthermore, the data suggests that excited state 7 characterization is also a CT state with a CT number of 0.60. These results were further supported by the NTO analysis of the benzoyl pyrazinium on excited state 7. The particle hole whole pair confirm that excited state 7 is indeed a CT state. Like our previous findings, the hole orbital is localized on the benzoyl group and the particle orbital is localized on the pyrazinium. The correlation between the high oscillator strengths around 280nm and the excited state character being a CT State in both the Benzoyl Pyrazinium and Benzoyl PyraziniumH strongly suggests that a high oscillator strength around 280nm must be

present and that the character of that excited state must be a CT state in order for the photoinitiated cyclization to occur.

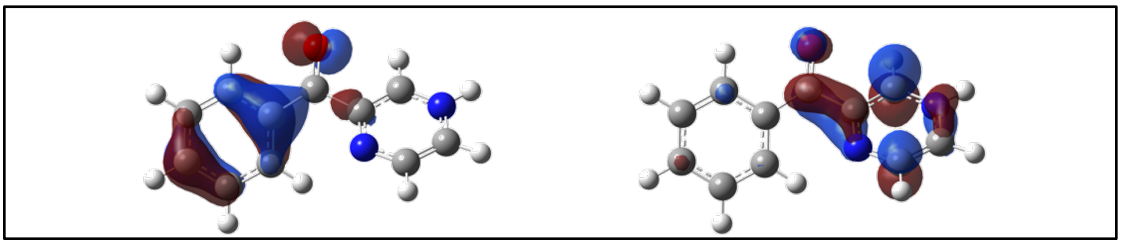
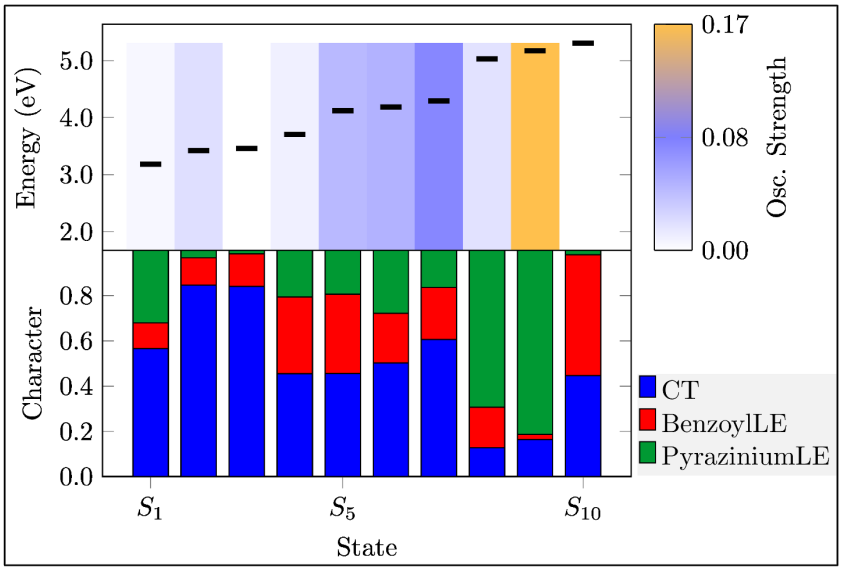


Figure 3.6 Hole and Particle NTOs for PyraziniumH Excited State 7



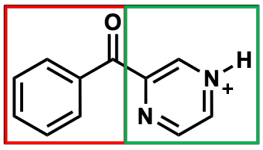


Figure 3.7 PyraziniumH Theodore Analysis Results

3.3 Study of Reactivity Due to Structural Factors

3.3.1 Testing electron deficiency on the N atom

In order to further elucidate the factors giving rise to the CT state we began by investigating if the electron deficiency on the Nitrogen of the charged pyrazinium gave rise to the CT state at the accessible energy range. To test this hypothesis, we looked at 3 uncharged benzoyl pyrazine compound derivatives, benzoyl pyrazine, benzoyl pyridine, and benzoyl pyrazineB4 (benzoyl 4-azaborine). These compounds were chosen in that order so that they would successively decrease the electron density at the positively charged position on the benzene ring (Figure 3.8).

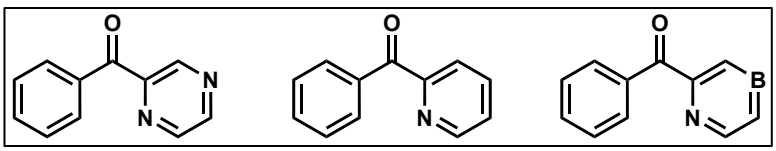
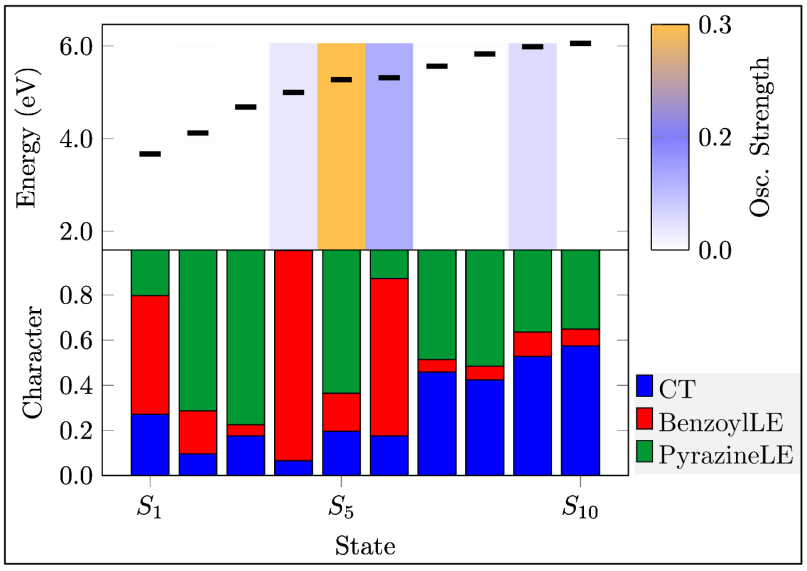


Figure 3.8 Electron Deficient Pyrazinium Derivatives

Figure 3.9, Figure 3.10, and Figure 3.11 are the results after carrying out TheoDORE analysis on each of the compounds respectively. The results show that there is a noticable difference in the absorption wavelengths for each compound respectively 235nm (5.3eV), 230nm (5.4eV), and 240nm (5.2eV) compared to the charged compounds. These absorptions all correspond to a large oscillator strength at the lowest energy. From the data we can conclude that all the compounds do not have an accessible excited state within the energy range of interest 280nm. Furthermore, the excited states with highest transition probability for each compound respectively S_5, S_5, and S_8 are not CT states. This is clear from the characterization of each excited state. In fact, they show the excited state is either a local excitation on the benzoyl group or the pyrazine rings. These findings are further supported by the low CT number of each of the compound's states of 0.20, 0.14, 0.22 respectively. These findings all seem to indicate that the electron deficiency on the Nitrogen of the charged pyrazinium is not the factor manifesting the CT state at low energies.



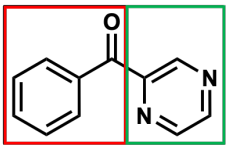
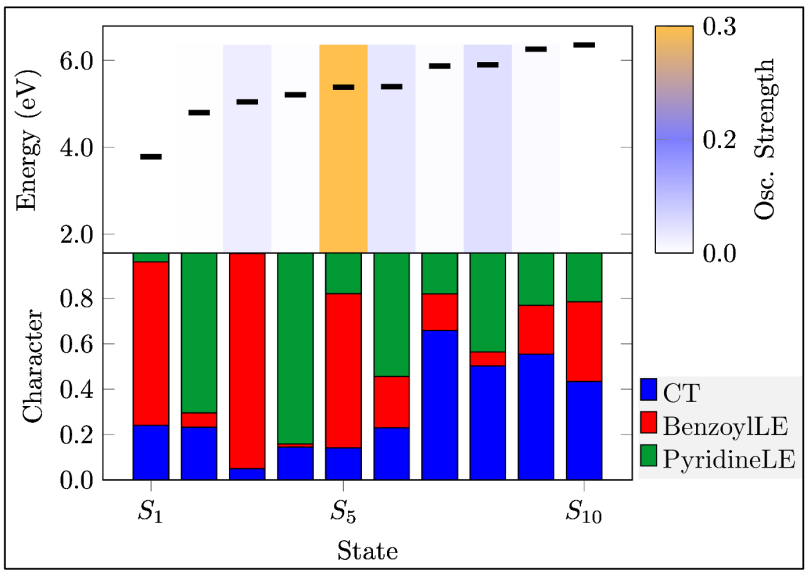


Figure 3.9 Benzoyl Pyrazine Theodore Analysis Results



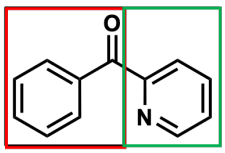
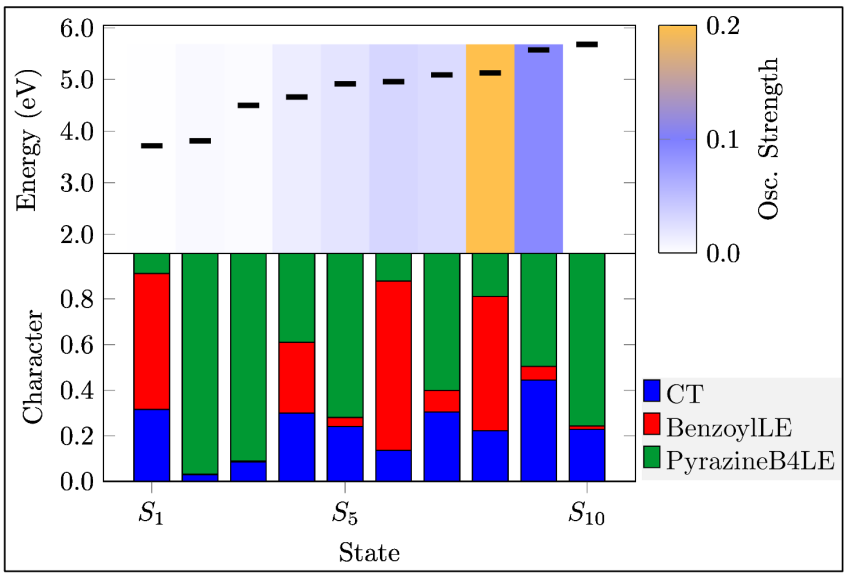


Figure 3.10 Benzoyl Pyridine Theodore Analysis Results



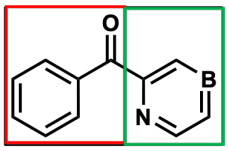


Figure 3.11 Benzoyl PyrazineB4 Theodore Analysis Results

3.3.2 Testing electron withdrawing effects on the pyrazinium ring

Another possible explanation giving rise to the CT state is the inductive effect of the pyrazinium ring due to a positive charge. This is due to the withdrawing ability of the charge to pull electron density towards that position. To explore this theory, we looked at 3 para substituted benzoyl pyridine derivatives, benzoyl 4-nitropyridine, benzoyl 4-cyanopyridine, and benzoyl 4-trifluoromethylpyridine. These substituted compounds were chosen due to their known electron withdrawing abilities.

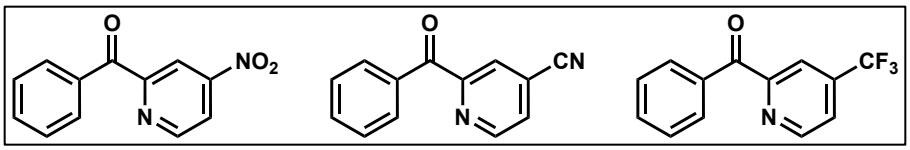
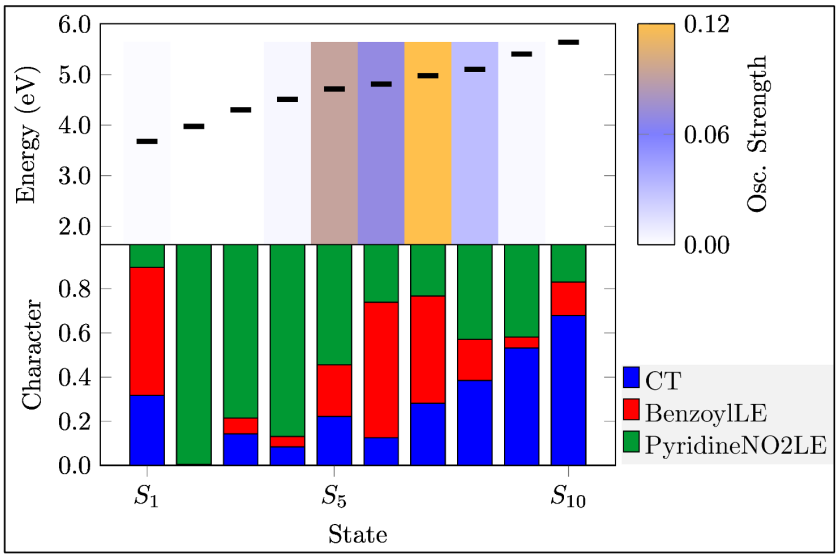


Figure 3.12 Electron withdrawing pyridine derivatives

After performing a TheoDORE analysis on the compounds the data reveals that the lowest accessible excited state of all three compounds is lower in energy than the electron deficient benzoyl pyrazinium derivatives. This seems to suggest that an inductive effect on the pyridine ring has the effect of bringing down the energy of the lowest accessible excited state. While the excited state of these compounds may be closer to being energetically accessible, all the accessible excited states still have very little CT character. Also, compared to the benzoyl pyridine CT number of 0.14, the nitro, cyano, and trifluoromethyl derivatives CT numbers 0.22, 0.25, and 0.25 respectively, seemed to have increased but not by a substantial margin. While the electron withdrawing of the compounds decrease from left to right in (Figure 3.12) the compound's CT numbers increased in the opposite direction. There seems to be a balance between the low energy excited and the CT number. Nonetheless, the inductive effect on the pyridine ring is not the origin of a CT state however, electron withdrawing groups on the pyridine ring do seem to lower the energy of the first accessible excited state. This is a promising tuning strategy that could be employed to control the energy level at which the photocyclization can occur once the presence of the CT can be controlled.



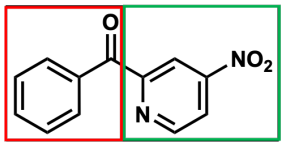
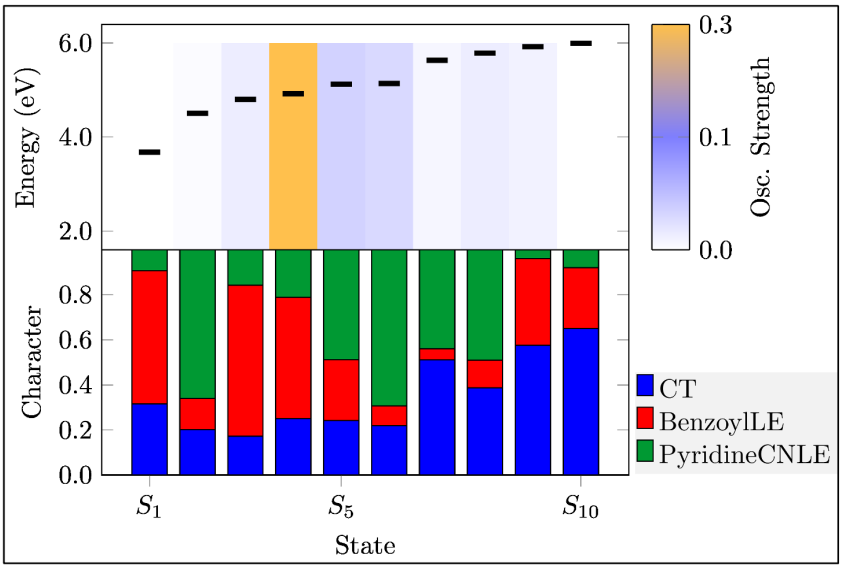


Figure 3.13 Benzoyl PyridineNO2 Theodore Analysis Results



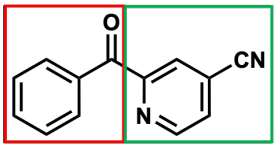
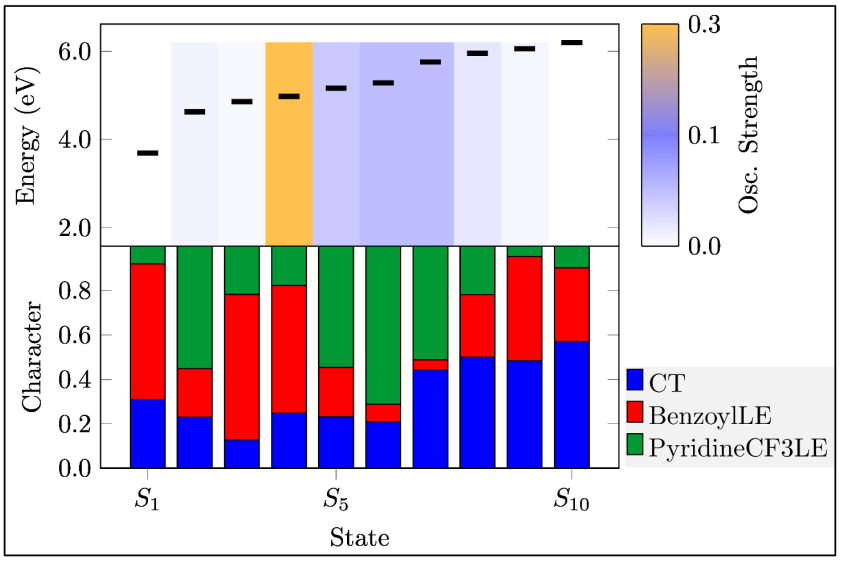


Figure 3.14 Benzoyl PyridineCN Theodore Analysis Results



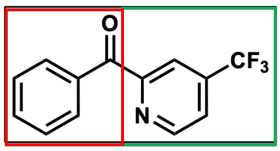
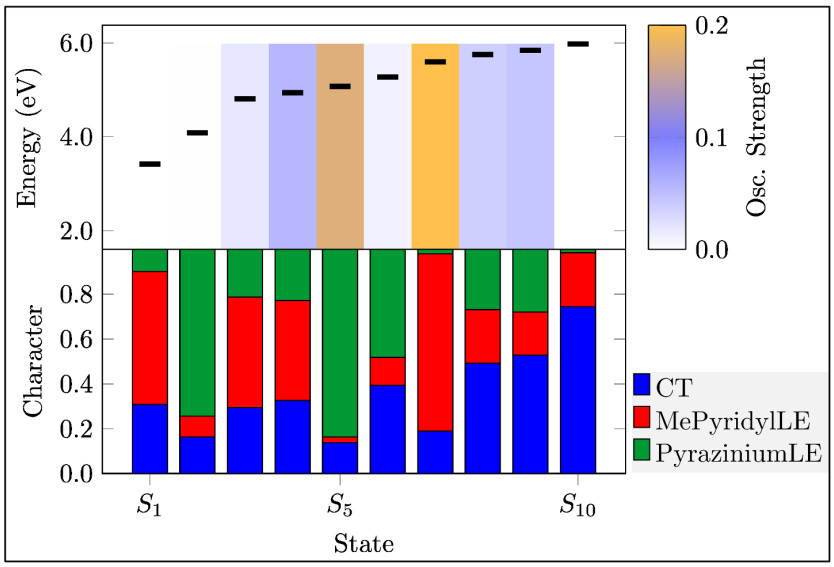


Figure 3.15 Benzoyl PyridineCF3 Theodore Analysis Results

3.3.3 Testing the presence of a charge

An alternative possible reason for the observed CT state is the actual charge itself on the pyrazinium ring. To explore this theory we designed a dual charged compound with the same charged structure on both side of the compound. This increseases the overall charge of the compound to plus two inorder to make the positive charge effect more pronounced. Additionally the symmetric structure on both sides of the compound ensures that the charge effect is the only effect we are testing. TheoDORE analysis of the compound in (Figure 3.16) shows us that excited state five is the lowest energy accessible state with an absorbance of 245nm (5.07eV). When compared the to the benzoyl pyrazine the increase

in charge on the Mepyridyl pyrazine implies that increasing charge decreses the energy of the lowest accessible exicted state. This tunning strategy is employed later on to achieve our desired energy range. Furthermore, the Mepyridyl pyrazinium excited state five has a CT number of 0.14 which is the same as the Benzoyl Pyridine analog and less than the CT number of 0.20 of the benzoyl pyrazine analog compound. Comparing the CT number data of the benzoyl pyrazine and the Mepyridyl pyrazinium there is actually a decrease in the amount of the CT character in the lowest accessible excited state suggesting that increasing the charge on the compound dreceases the amount of CT character. While increasing the charge on the compound may lower the energy of the lowest accesible excited state it opposes the increase of the CT character in that state hence not being the origin of the CT state



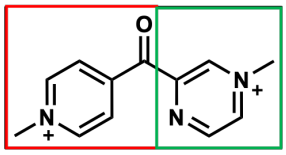


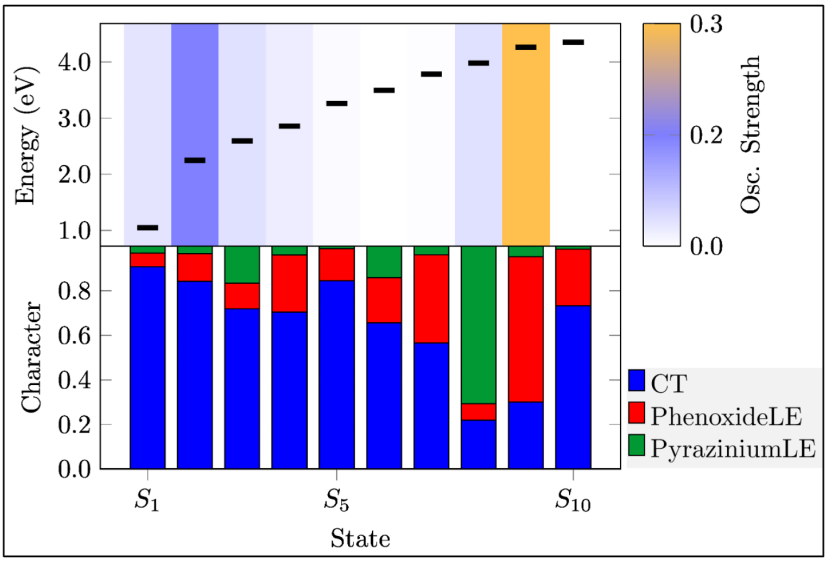
Figure 3.16 MePyridyl Pyrazinium Theodore Analysis Results

3.3.4 Testing the charge dipole produced by the charge

Using what we learned from the previous case we decided to test one more theory. An added consequence of having a charged compound is that the charge creates a charged dipole moment in the molecule. This is due to the charge being on one aromatic ring and not the other, this creates an electrical imbalance making electron density wanting to move from left to right. In order to test this hypothesis, we constructed a benzoyl pyrazinium analog that would only test the charge dipole effect and not the charge itself. We did this with the phenoxide pyrazinium analog. The phenoxide pyrazinium is overall a neutral compound however there a dipole created by the negatively charged phenoxide on the left side and the positively charged pyrazinium on the right (Figure 3.17). When analyzing the TheoDORE results indicate that the charge dipole has drastically lowered the energy of the lowest accessible state to 552 nm (2.25eV) compared the Benzoyl Pyrazinium of 280nm (4.43eV). Additionally, the CT number of excited state two is 0.84 which is by far the highest CT character of an accessible state thus far. Furthermore, all of the first seven excited states of the phenoxide pyrazinium have over 50% CT character. Noteworthy is the

first excited state having 90% CT character and being able to be accessible in the infrared region of the electromagnetic spectrum with an energy of 1184nm (1.05eV).

NTO analysis, (Figure 3.18) and (Figure 3.19), revealed that both the 1st and 2nd excited states are single particle transition from the HOMO to LUMO and HOMO to LUMO+1 respectively. The NTOs of the 1st and 2nd transitions revealed that that they are both n to π^* transitions respectively. The first transition involves the non-bonding orbital of the oxygen on the phenoxide to a π^* with 2 nodal planes going through bonds on the pyrazinium. This means there is still electron density on the positively charged nitrogen. As opposed to the 2nd transition that involves the non-bonding orbital of the oxygen on the phenoxide to a π^* with 2 nodal planes, where one of planes cuts through the two Nitrogen atoms. This leaves the charged nitrogen without electron density and why it is higher in energy compared the 1st transition. This data and analysis strongly suggests and leads us to believe that the charged dipole is the reason behind the CT states.



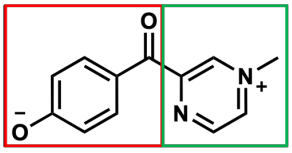


Figure 3.17 Phenoxide Pyrazinium Theodore Analysis Results

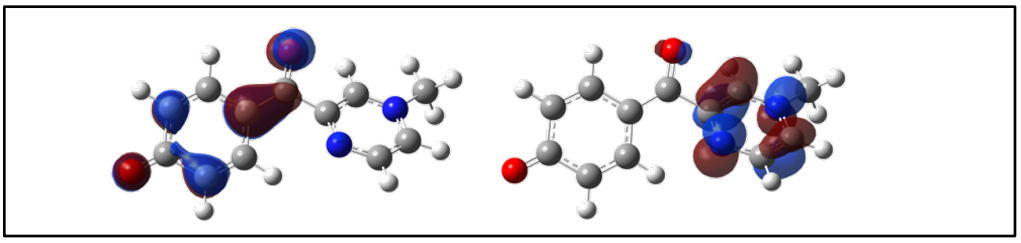


Figure 3.18 Phenoxide Pyrazinium Excited State 1 NTOs

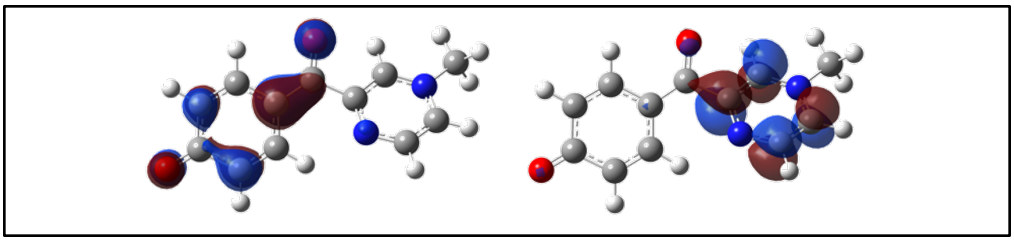


Figure 3.19 Phenoxide Pyrazinium Excited State 2 NTOs

3.4 Push Pull Systems and Hammett Study

Using what we learned about the electric dipole mechanism to enhance the amount CT character in an excited state and the previous tunning strategies disccussed, we designed compounds to see if we could tune the excited state CT character and energy. We began by implementing successive para substituted benzoyl pyrazinium derivatives with increasing electron dontating ability from left to right (Figure 3.20). This was done to slowly tune and increase the dipole in the compound from left to right.

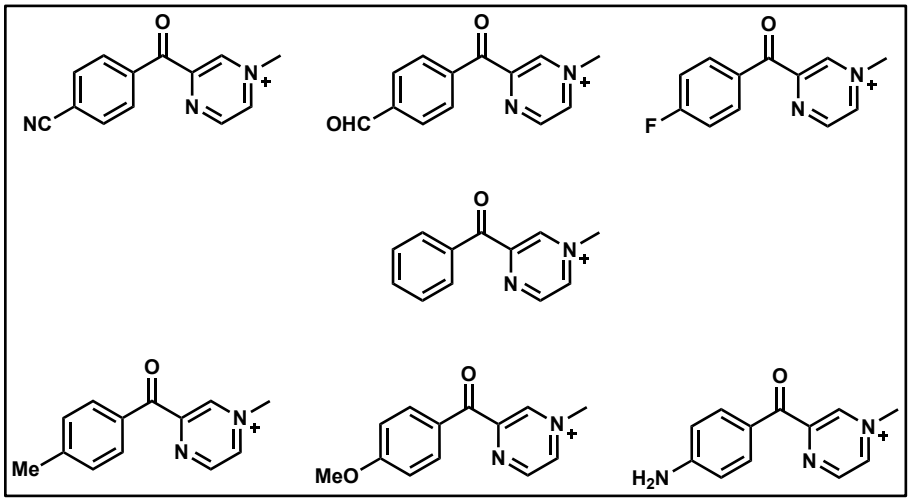


Figure 3.20 Para-substituted Benzoyl Pyrazinium Derivatives

After performing TheoDORE analysis on all of the compounds, we noticed that in general there is an increase in the amount of CT when varying the electron widrawing groups (EWGs) to the electron donating groups (EDGs). In order to quantify the variation in electron donation ability between all these compounds, we used the hammet sigma parameter (σ_p).[60] The hammet sigma parameter is based off a linear free energy relationship which measures how varying electron donating ability of benzoic acid with different para substitued functional groups affects its pKa. A negative sigma values are correlated with EDGs since they decrease the rate deprotonation in the benzoic acid. While a positive sigma value are correlated with EWGs since they increase the rate of deprotonation. Using the tabulated values for each of the para substituted functional groups in (Figure 3.20) and

comparing them to the their calculated CT number from the TheoDORE analysis we were able to find a trend.

Performing linear regresssion on the data suggest a linear free energy relationship between the CT number and σ_p (Figure 3.21). The linear correlation proposes that increasesing the electron donation of the parasubstitued group increases the amount of CT in the compound. Furthermore, 82% of the variation in the CT number can be explained by just the hammet parameter, σ_p, and it is statistically significant within a 95% confidence interval.

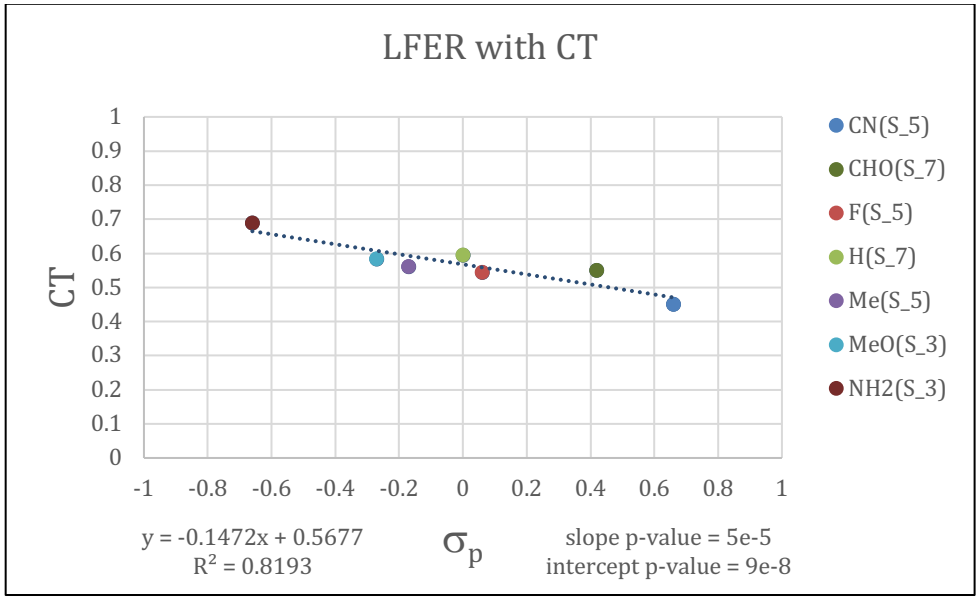


Figure 3.21 Linear Free Energy Relationship between CT and a hammet parameter. This is a linear regression plot between seven compound's hammet parameter and CT number. Linear regression between σ_p and CT yielded a slope of -0.1472 ± 0.03 with p-value = 5e-5, intercept of 0.5677 ± 0.03 with p-value = 9e-8, and R^2 = 0.8193.

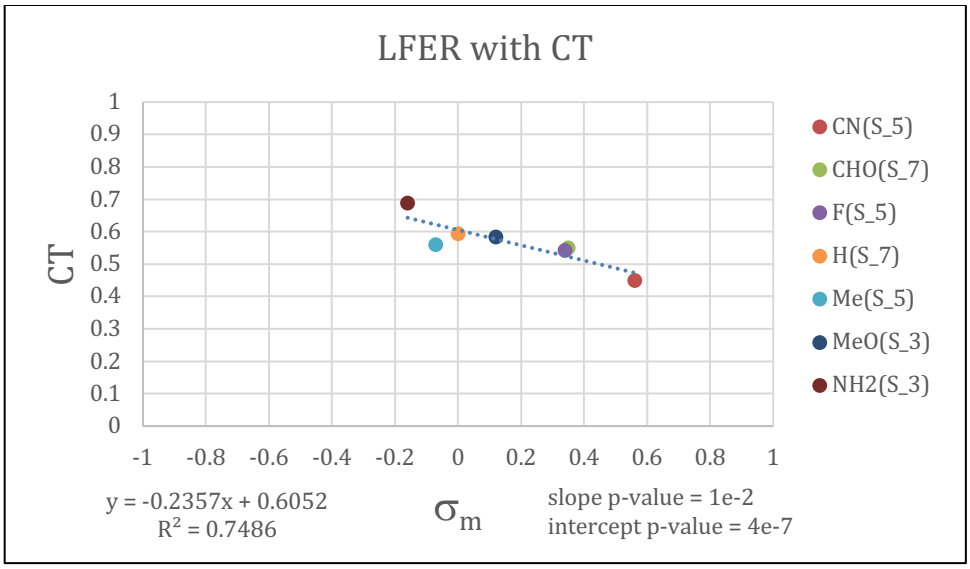


Figure 3.22 Linear Free Energy Relationship between CT and a hammet parameter. This is a linear regression plot between seven compound's meta hammet parameter and CT number. Linear regression between σ_p and CT yielded a slope of -0.2357 ± 0.06 with p-value = 1e-2, intercept of 0.6052 ± 0.02 with p-value = 4e-7, and R^2 = 0.7486.

While the σ_p hammet parameter can relate information about the electronic resonance effects of substituted benzoyl pyraziniums it does not relate how the inductive effects of these substituted derivatives are related to charge transfer. To test this correlation a new hammet parameter σ_m is used since meta substituents on a benzene cannot resonate to the same position as a para substituted benzene rings. Performing linear regression with σ_m, results in only 75% of the variation in the CT number can be explained by the inductive effects of the substituted benzoyl pyraziniums. This lead us to conclude that substituents with stronger resonance effects enhance the CT number more than inductive substituents.

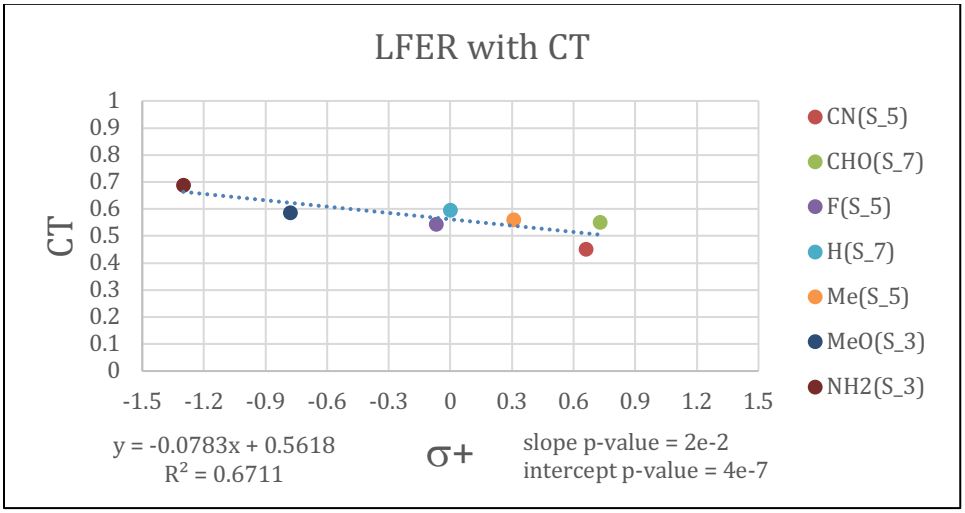


Figure 3.23 Linear Free Energy Relationship between CT and a hammet parameter.

This is a linear regression plot between seven compound's meta hammet parameter and CT number. Linear regression between σ_p and CT yielded a slope of -0.2357 ± 0.06 with p-value = 1e-2, intercept of 0.6052 ± 0.02 with p-value = 4e-7, and R^2 = 0.7486.

Lastly, we investigated if the CT number was correlated to the resonance effects of direct conjugation of a para positioned positive charge in the benzene ring. The linear regression results in Figure 3.23 showed that only 67% of the variance in the CT number can be explained by this property. This led us to believe that the most effective strategy for increasing the CT number is to use substituted electron donating groups at the para position that have the strongest resonance effect.

Furthermore, (Figure 3.24) illustrates how the λ_{max} is red shifted to lower energy values as we increase the elctron dontating ability of the functional group. This was the same trend that we observed when we tested the benzoyl pyridine compounds and was attributed to electron donation ability of the of the groups on the compound.

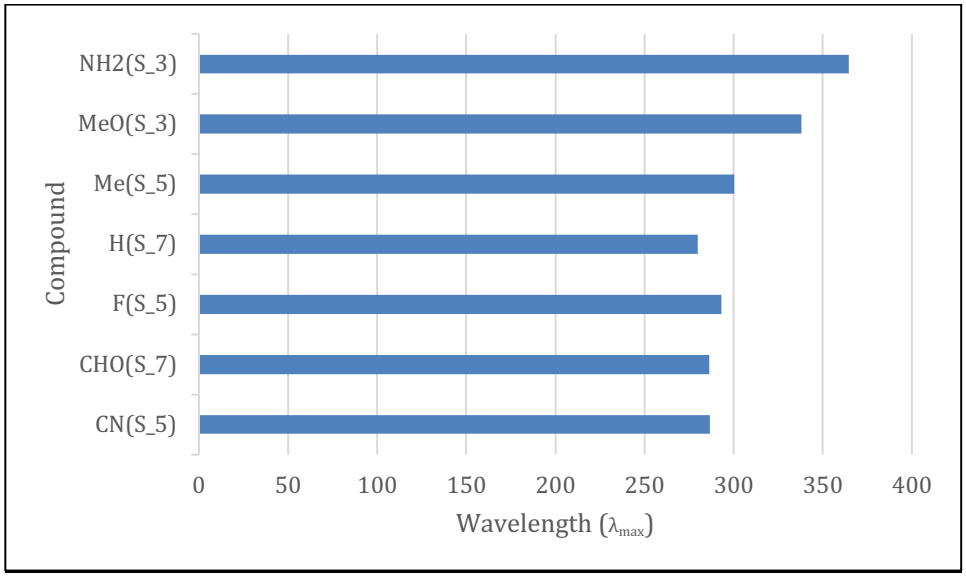
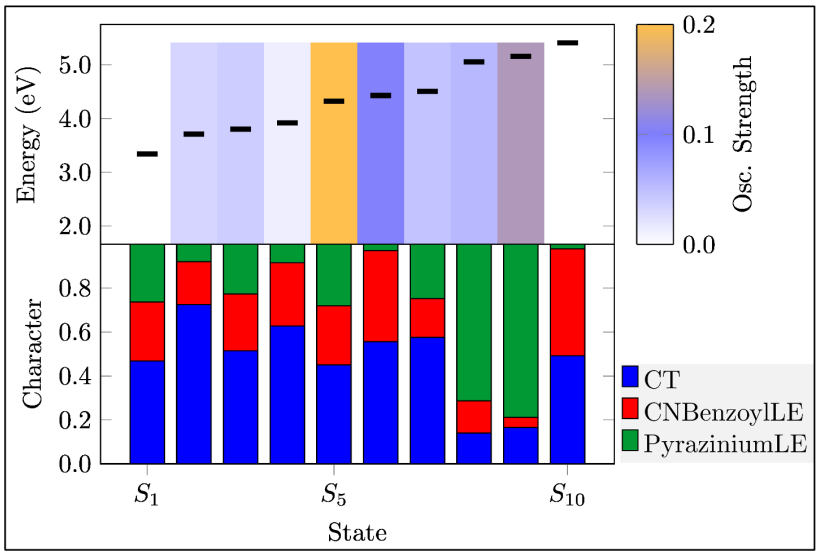


Figure 3.24 Electronic effects on absorption λ_{max} of compounds in (Figure 3.20)



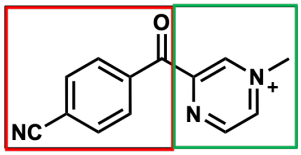
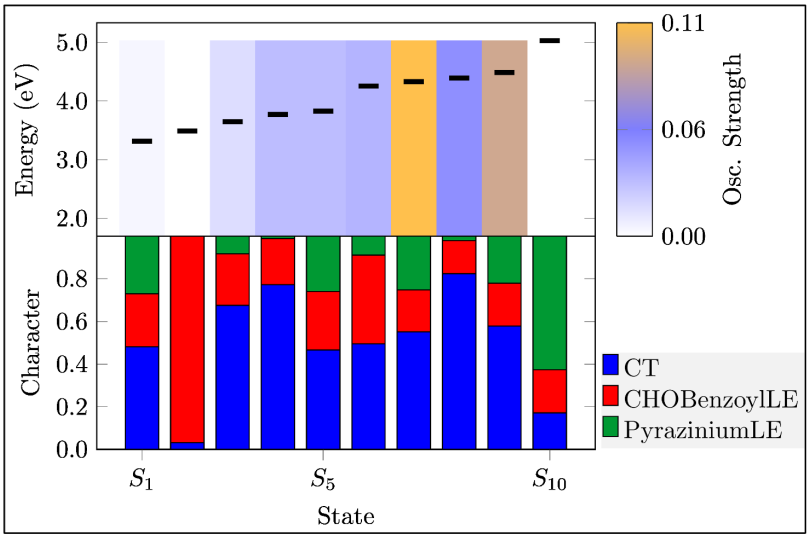


Figure 3.25 CN BenzoylPyrazinium Theodore Analysis Results



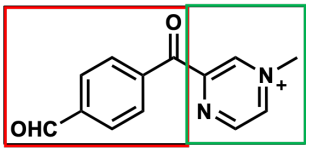
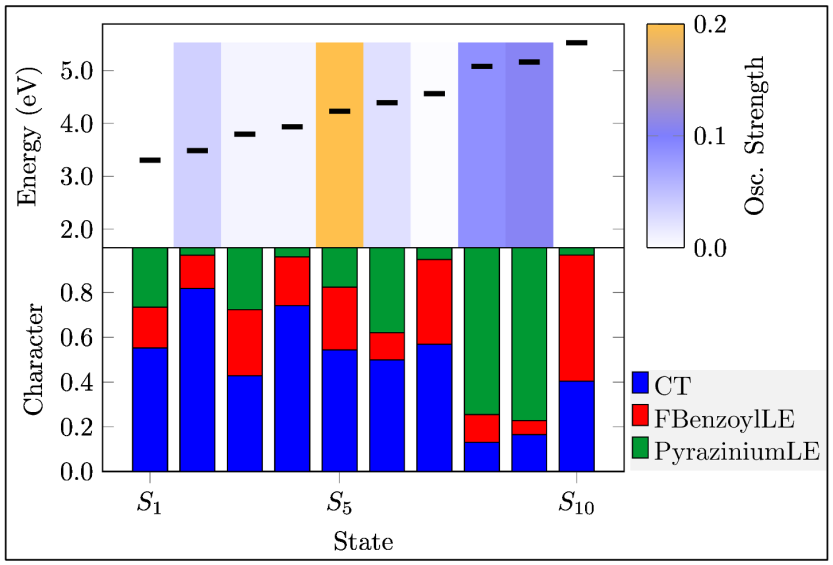


Figure 3.26 CHO BenzoylPyrazinium Theodore Analysis Results



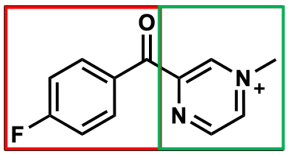
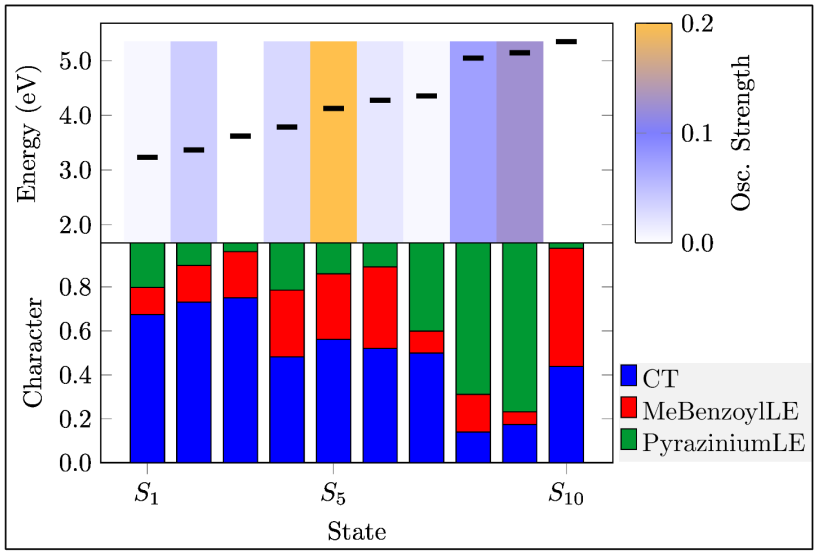


Figure 3.27 FBenzoylPyrazinium Theodore Analysis Results



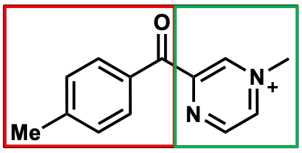
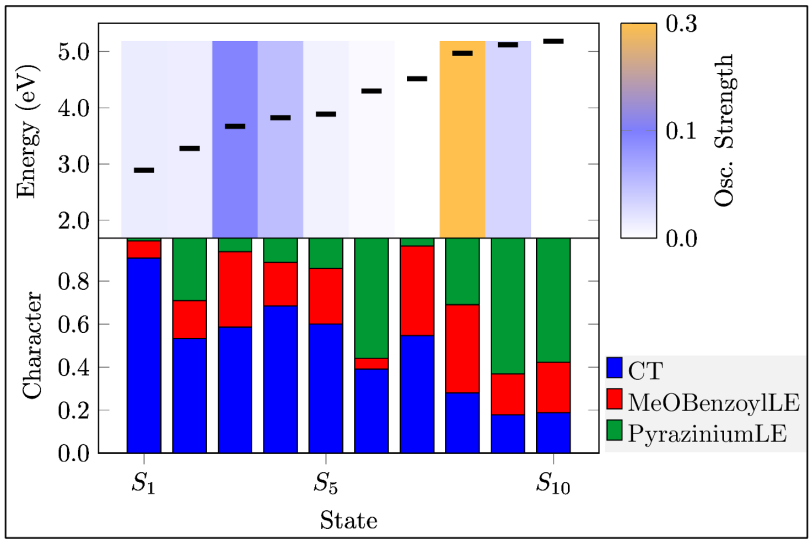


Figure 3.28 MeBenzoyl Pyrazinium Theodore Analysis Results



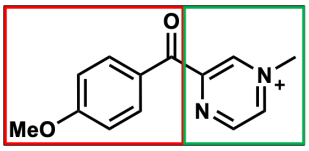
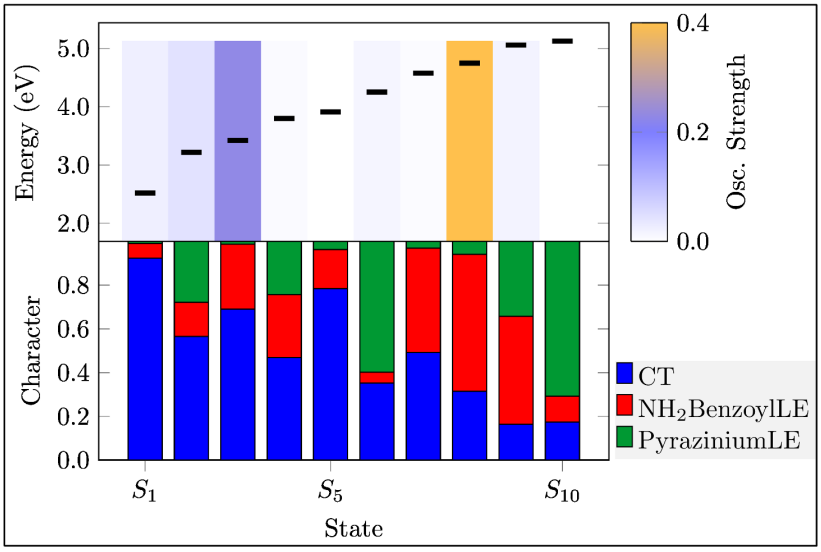


Figure 3.29 MeOBenzoyl Pyrazinium Theodore Analysis Results



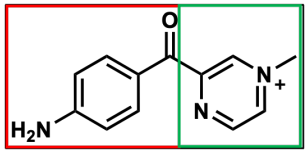


Figure 3.30 NH2Benzoyl Pyrazinium Theodore Analysis Results

3.5 Conclusion

In conclusion, by modeling the photophysical absorbption of the benzoyl pyrazinium we were able to determine that the state of interest for photophysical cyclization of this compound is a charge transfer state as determined by the difference density and the NTO analysis. Moreover we tested if the charge transfer state came was caused by the electronic difficiency, inductiveness, charge density, or charge dipole. Thorough investigation of each of these theories was tested by designing compounds in a systematic manner and were ruled out. The charge dipole was the determining factor for the presence of the charge transfer state at low energies. This was then used as a rational design princple for increasing the amount of CT character in a series of compounds. All compounds saw an increase in the amount of CT character as the hammet parameter

became more negative. A linear free energy relationship strongly supported the data fitting the hammet equation. Further work will need to be done in order to find a rational design principle for increasing the oscillator strength of the charge transfer state for optimal absorption.

Chapter 4

Δ-SCF Methods for Charge Transfer Excitations

4.1 Background

Computational modeling of electronic excited states is essential for understanding photophysical transitions and photochemical phenomena in dyes, photocatalyst, and optoelectronics.[61–65] Time-dependent density functional theory (TD-DFT) is the most widely used quantum chemistry technique for computing electronic excited state energies due to its low computational cost.[66] For quantitative accuracy, hybrid functionals are recommended, where the exchange-correlation energy (E_{XC}) contains a percentage of Hartree-Fock exchange. While hybrid TD-DFT does quite well for valence excitations, it has serious problems for CT excitations. This deficiency stems from the exchange correlation energy having the wrong long-range behavior. This causes TD-DFT to underestimate excitation energy from CT states. To characterize these difficult excited state transitions many methods have been developed based on difference densities, and transition densities. Despite these models and developing CT metrics this still remains an active area of research.[55,67]

One model developed by Martin for interpreting TD-DFT results has a simple one-electron interpretation in terms of a particle (the excited electron) and hole.[54] The Natural Transition Orbital (NTO) model uses the transition density matrix to characterize an electronic excitation into a condensed orbital representation. The NTOs are a pair of particle hole orbitals with coefficients giving the contribution of each pair's contribution to the excitation. Excited state properties can then be decomposed into contributions from particle and hole densities constructed from the particle and hole orbitals respectively. In particular, the particle and hole densities can be used to define CT distance metrics as a weighted sum between atoms. However, this approach requires defining a fragmentation scheme over which of the atoms are being considered. This the approach taken by Plasser and coworkers which allows them to calculate the exciton size and distance.[68]

Another approach was recently developed by our group that uses Δ-SCF to generate the difference density from two SCF calculations. In particular, the projected initial maximum overlap method (PIMOM) variant was used to obtain the ground and excited state densities to the form the difference density between both states.[69] This has the advantage that PIMOM works with the standard ground state machinery, such as highly efficient programs for calculating analytic derivatives and electronic properties. This leads to costs similar to both ground state Hartree-Fock and DFT calculations. Also, since Δ-SCF is a mean-field method relaxation is accounted in the excited state by changes in

the mean-field potential found in the Fock operator. Using the difference density, it is then possible to decompose the density difference into an excitation and relaxation densities. Which allowed us to decouple the excitations and relations and define a CT metric and oscillator strengths based on a particle hole pair from just the excitation matrix.[70]

4.2 Results

In the following we test and compare Δ-SCF with TD-DFT using different compounds and compare qualitative and quantitative results between both methods. Each of the compound's calculations were done with DFT using the ω-B97XD functional and def2-TZVP basis set. Subsequent TD-DFT calculations were computed at the same level of theory for the first S_1 excited state. These compounds were chosen to test the different kinds of CT and the degree to which Δ-SCF can reproduce or exceed TD-DFT results compared to experiment.

4.2.1 Ruthenium and MLCT

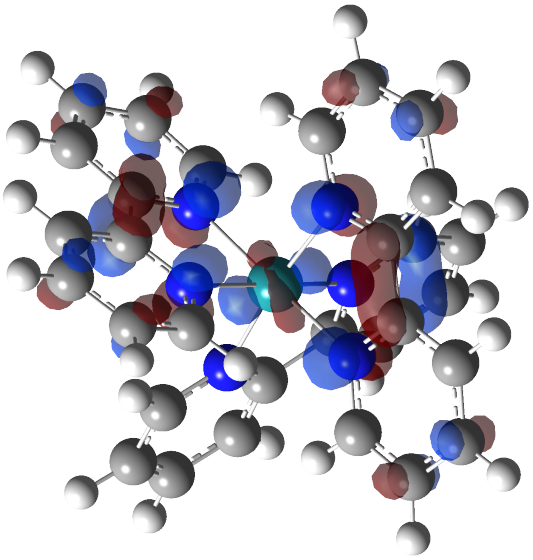


Figure 4.1 RuBiPy Particle NTO

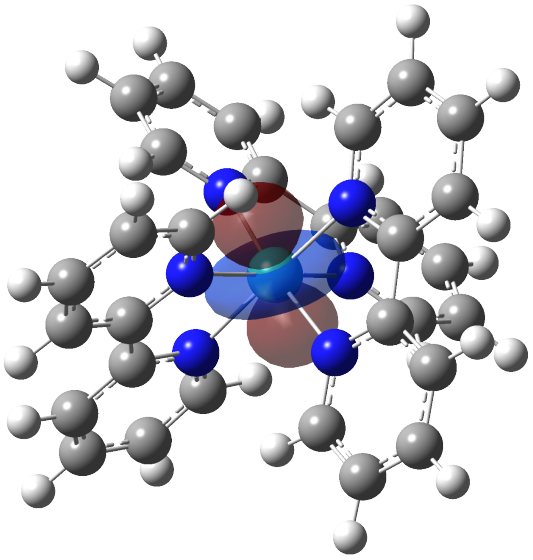


Figure 4.2 RuBiPy Hole NTO

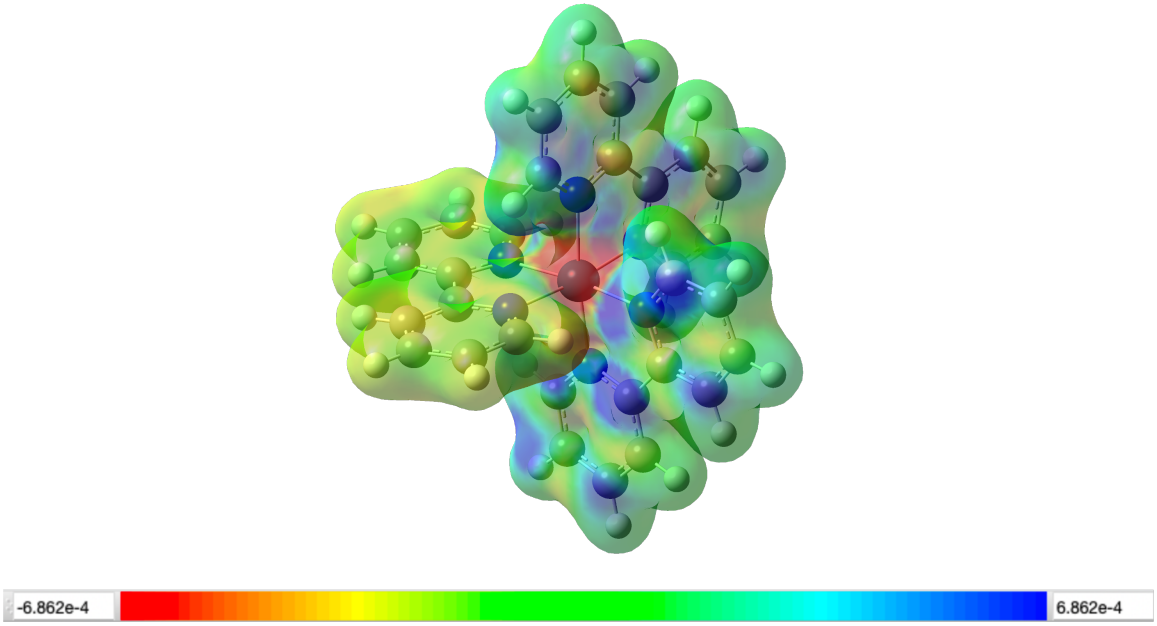


Figure 4.3 RuBiPy TD-DFT Density Difference

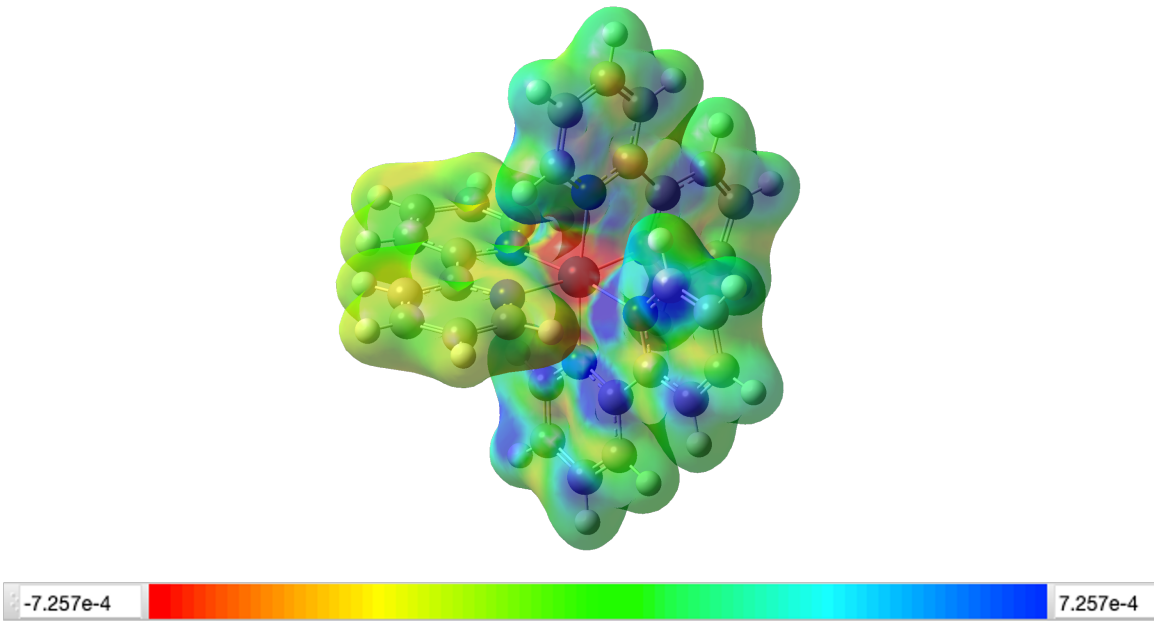


Figure 4.4 RuBiPy Δ-SCF Difference Density

4.2.2 Copper and LLCT

To test if Δ-SCF can be used for charge transfer excitation we chose three different compound of different CT character. Ru(II)$(bpy)_3$ or RuBiPy as it is commonly known was chosen as the test case for meta to ligand charge transfer (MLCT).[71] The first analysis we performed was the NTO model mentioned above. Figure 4.1 and Figure 4.2 show the results of the analysis as the particle and hole pair. It is easy to see that the excitation can be characterized as MLCT since the hole NTO is a localized d-orbital on ruthenium and the particle NTO is dispersed across the ligand. The second analysis is to use the TD-DFT computed density difference formed the ruthenium ground state and the S_1 excited state Figure 4.3. This was compared with the Δ-SCF computed density difference from the ground sate SCF job and the PIMOM excited state job Figure 4.4. The same features are found in both densities showing the loss of densities on the metal and the gain of density in the excited state. It is clear that for a MLCT there is very little difference between the Δ-SCF and TD-DFT computed density difference.

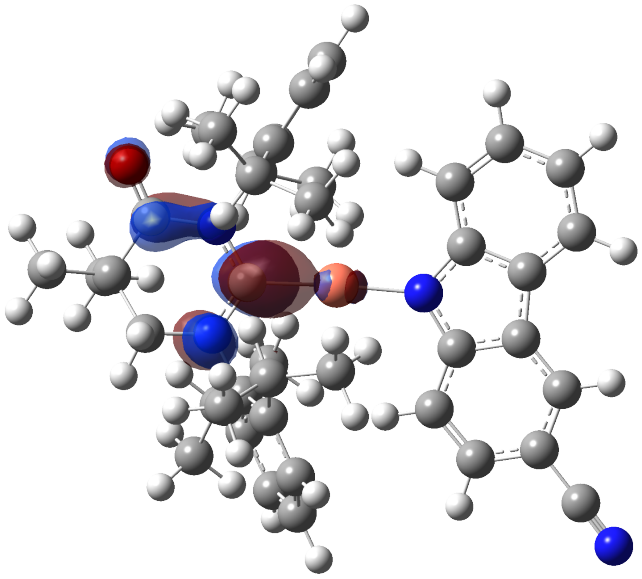


Figure 4.5 MACCu(I)CzCN Particle NTO

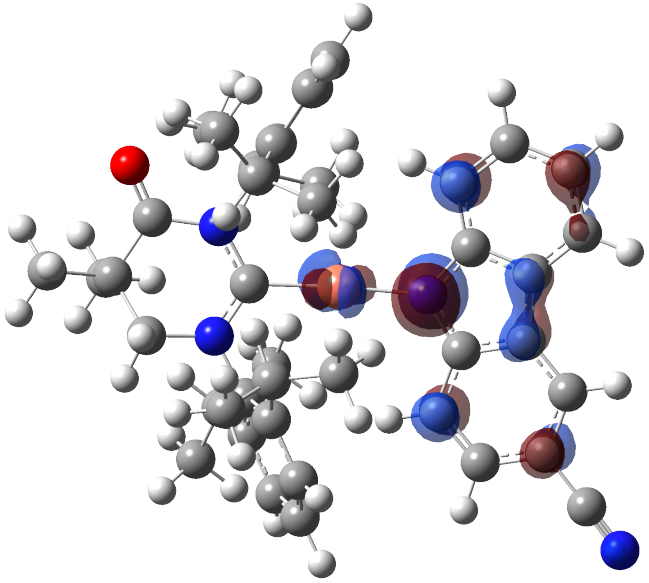


Figure 4.6 MACCu(I)CzCN Hole NTO

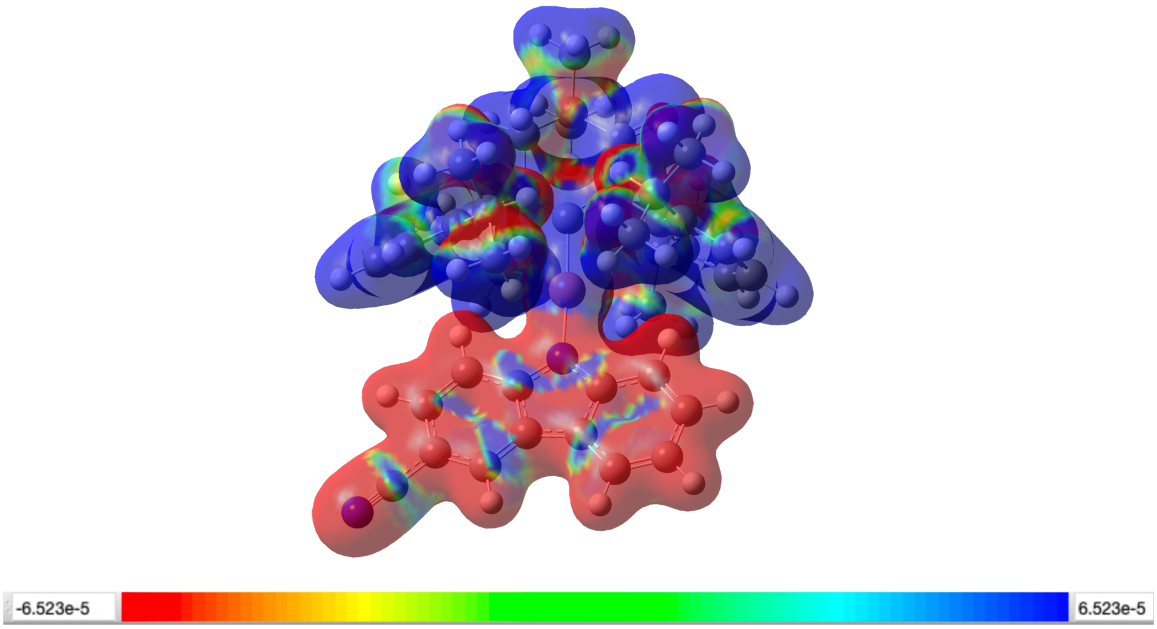


Figure 4.7 MACCu(I)CzCN TD-DFT Difference Density

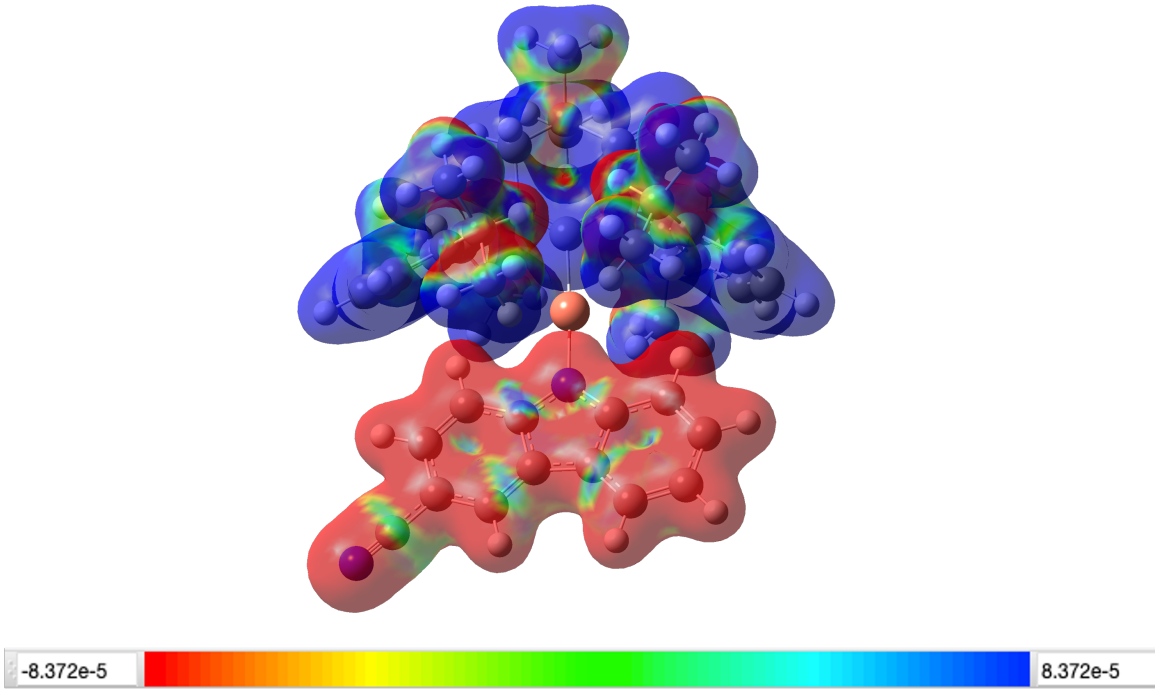


Figure 4.8 MACCu(I)CzCN Δ-SCF Difference Density

4.2.3 Zirconium and LMCT

The following compound is to test ligand-to-ligand charge transfer (LLCT) and was tested on MACCu(I)CzCN.[72] The NTO analysis shows the hole NTO, Figure 4.6, localized on the ligand on the right and the particle NTO, Figure 4.5, localized on the ligand on the left. Since the particle and hole orbitals are localized on different ligands, we characterized this excitation as a LLCT. Correspondingly, the difference density analysis was computed using both the TD-DFT and Δ-SCF densities from the ground and excited states respectively. Figure 4.7 and Figure 4.8 show the results from TD-DFT and Δ-SCF. The TD-DFT results show a clear loss and gain of electron density from one ligand to the other. While the Δ-SCF results give the same end results of change in density from one ligand to the other. It is much clearer to identify this an LLCT since there is no electron density present on metal center. This points to the excitation moving density from one ligand directly to the other.

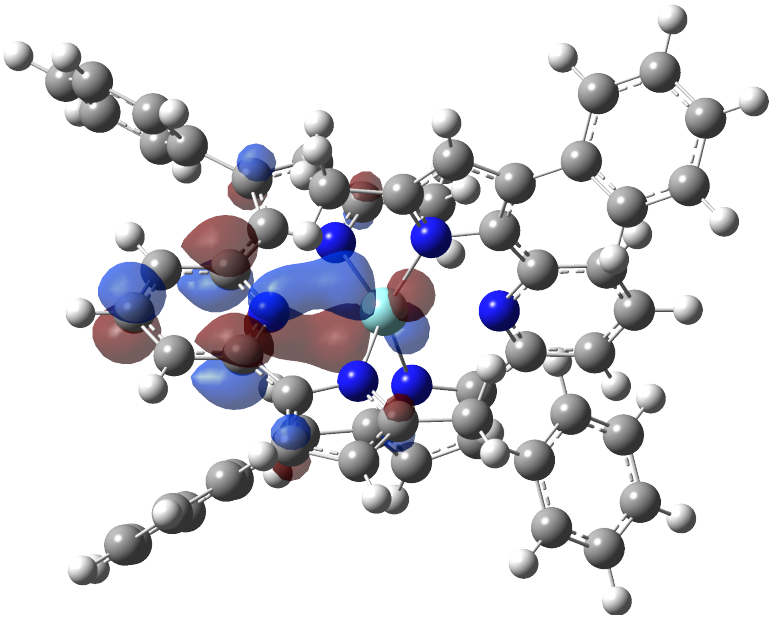


Figure 4.9 Zr(IV)Me(PDP)$_2$ Particle NTO

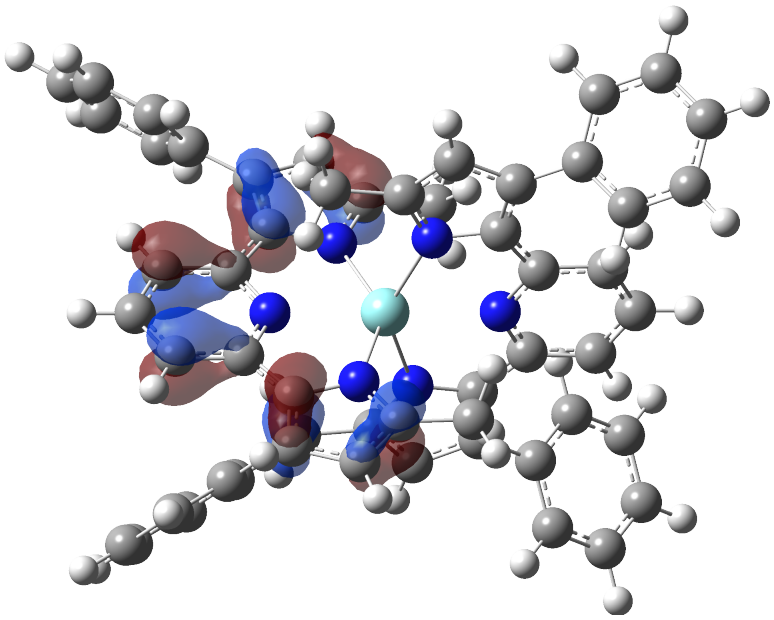


Figure 4.10 Zr(IV)Me(PDP)$_2$ Hole NTO

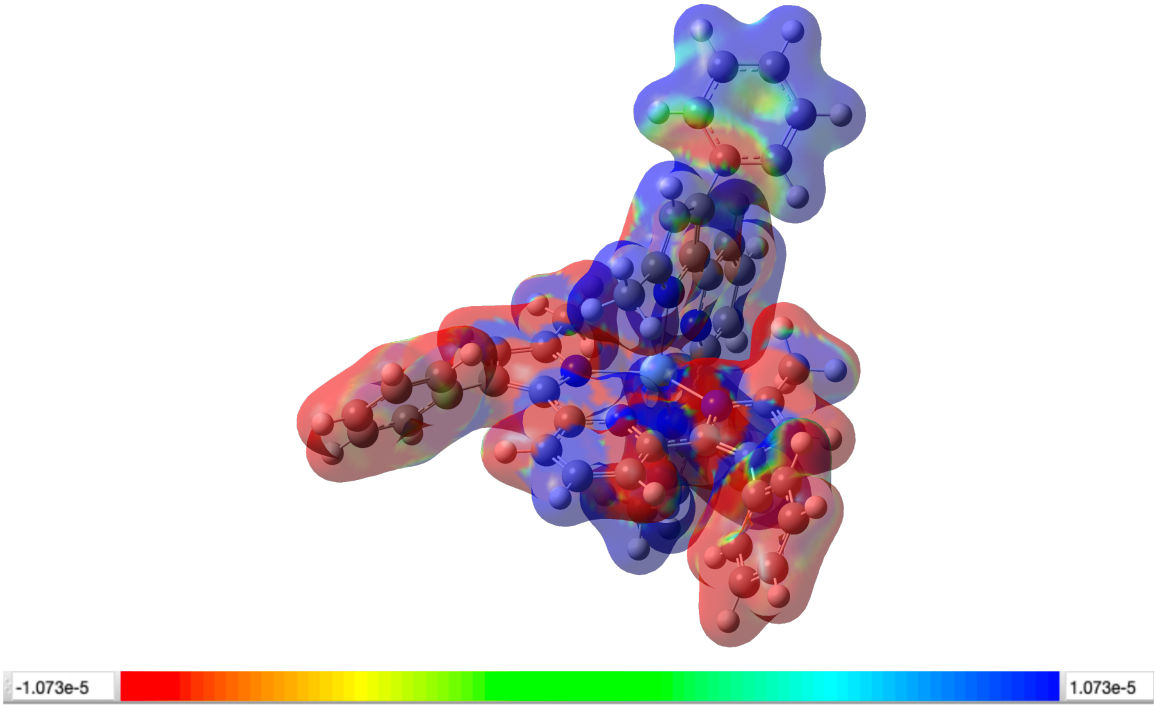


Figure 4.11 Zr(IV)Me(PDP)$_2$ TD-DFT Density Difference

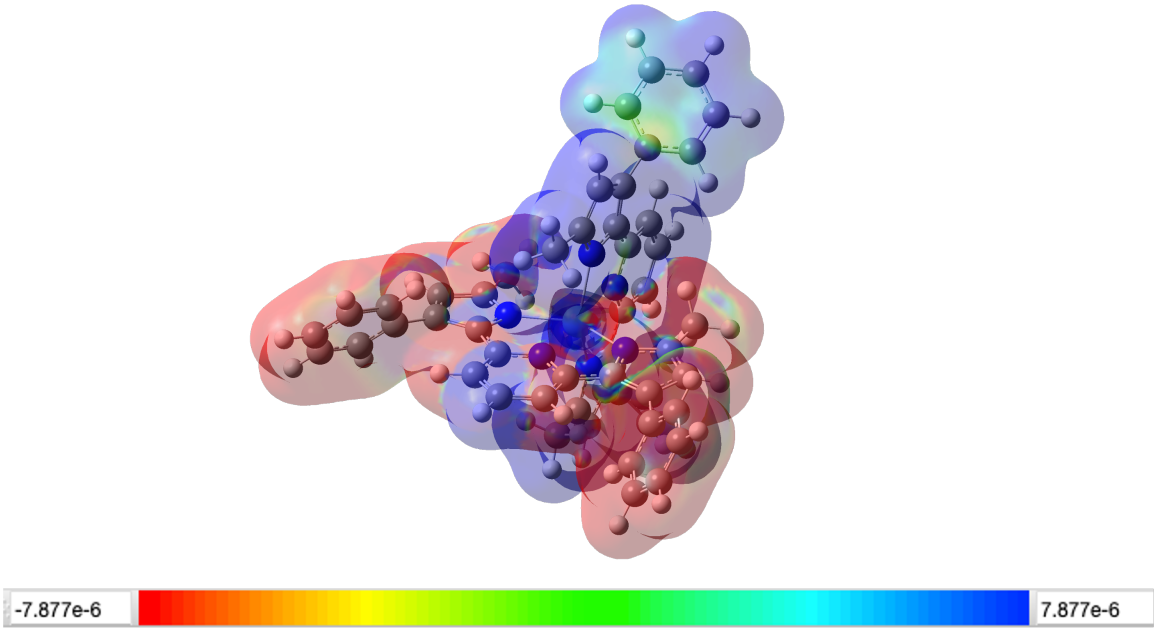


Figure 4.12 Zr(IV)Me(PDP)$_2$ Δ-SCF Difference Density

Our final analysis was on a Zr(IV)Me(PDP)$_2$ complex to test if we could characterize a ligand to metal charge transfer (LMCT).[73] The hole NTO, Figure 4.6, shows a delocalized π orbital over the ligand. While the particle NTO, Figure 4.9, show donation from the ligand to a metal d-orbital. This is already suspect of CT and specifically shows signs of a LMCT. To confirm we analyzed both of the difference densities from TD-DFT and Δ-SCF. The TD-DFT results, Figure 4.11, shows loss of electron density from the ligand and gain of electron density at the metal. However more detail can be seen from the Δ-SCF results which show there is a larger concentration of electron density gained at the metal center compared to the rest of molecule. This distinction is why characterization of the excitation was easier with the Δ-SCF method and was assigned as LMCT.

Table 1 Quantitative metrics for Δ-SCF vs TD-DFT on Charge Transfer States

Compound	Ref (nm)	$\Delta E_{\Delta SCF}$ (nm)	ΔE_{DFT} (nm)	$f_{\Delta SCF}$ (a.u)	f_{DFT} (a.u.)	$\|\boldsymbol{d}_{CT}\|_{\Delta SCF}$ (Å)	$\|\boldsymbol{d}_{CT}\|_{\mathrm{DFT}}$ (Å)
Ru(II)(bpy)$_3$	455	447	384	0.001	0.000	1.27	0.83
MACCu(I)CzCN	492	430	336	0.073	0.122	4.55	2.31
Zr(IV)(^{Me}PDP)$_2$	528	450	415	0.226	0.263	0.03	0.19

While the NTOs and difference densities provide a way to qualitatively characterize the different kinds of CT it does not give us quantitative information and metrics regarding the extent of CT. Table 1 shows the excitation energies ΔE of each of the compounds along

with their corresponding oscillators strengths (f) and CT distance, $\|\boldsymbol{d}\|$, computed at the TD-DFT and Δ-SCF level. The results of the excitation energies show that Δ-SCF is much better at absolute energies and closer to experimental results than TD-DFT. The oscillator strengths give us relative agreement in intensities between both methods. The extent of the CT as measured by the distance metric is where we see the largest difference between the methods due to the exchange correlation of TD-DFT at long range. Specifically, we see the largest difference with the LLCT Cu complex since this has the largest distance traveled from one side of the molecule to the other. This effect is not seen with the Δ-SCF since it is taken into account by the exact exchange.

4.3 Conclusion

In conclusion, we have analyzed and tested three different compounds with different characterizations of CT. Both TD-DFT and Δ-SCF difference densities were used to analyze and characterize each compound as either MLCT, LLCT, or LMCT. Qualitatively the difference densities from both methods are in agreement but the Δ-SCF method shows a much more detailed and clearer picture of the excitation and makes it easier to characterize the transitions. Quantitatively the excitation energies computed by Δ-SCF are in better agreement to experiment than TD-DFT. The biggest difference was seen with extent of CT distance since TD-DFT struggles at long-range. In all, Δ-SCF has proven to be a capable alternative to TD-DFT than can reliably achieve or surpass qualitative and quantitative metrics for characterization of various different CT states.

Chapter 5

Transition State Optimization

"The underlying physical laws necessary for the mathematical theory of a large part of physics and the whole of chemistry are thus completely known, and the difficulty is only that the exact application of these laws leads to equations much too complicated to be soluble. It therefore becomes desirable that approximate practical methods of applying quantum mechanics should be developed, which can lead to an explanation of the main features of complex atomic systems without too much computation."

-Paul Dirac

5.1 Background

Potential energy surfaces play a crucial role in modeling chemical reactions using computational chemistry. In fact, most calculations begin by optimizing one or more chemical structures to minima on a potential energy surface (PES). This is because most chemical processes and properties require equilibrium geometries, which are minima on a PES. For example, to calculate thermodynamic quantities using the harmonic approximation you first need to find the minima on the PES which coincide with equilibrium geometries. Furthermore, to calculate elementary reaction rate constants or reaction barriers, you need to be able to locate transition state structures, which correspond to first order saddle points on the PES. These and many more chemical phenomena rely upon algorithms that are efficient and robust to be able to explore the stationary points of a PES.[74,75]

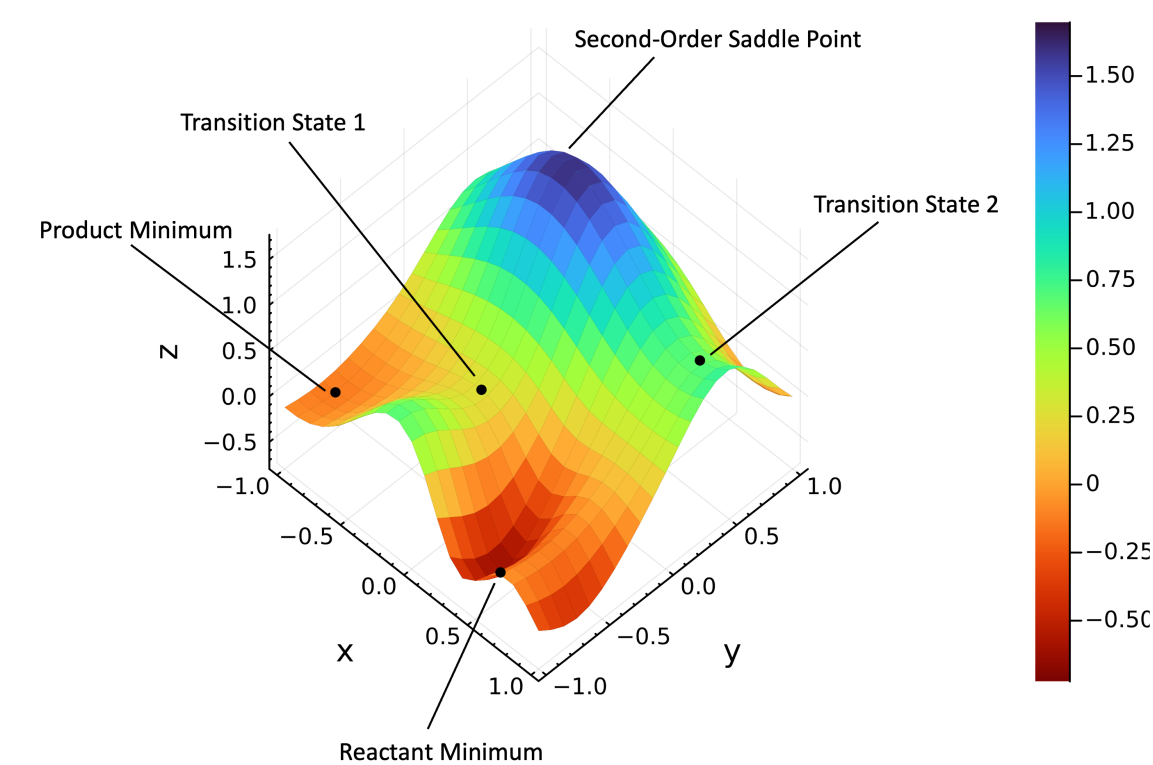


Figure 5.1 The Schlegel model potential energy surface showing reactant and product minima, multiple transition states (first-order saddle points), and a second-order saddle point.

Figure 5.1 shows the Schlegel model PES and many characteristic topologies. This model surface is meant to demonstrate many of the features encountered in real molecules and reactions. The energy of this model system is along the z-axis, and the nuclear coordinates are represented on the x and y axes. A common way to describe the topology of a PES is by comparing it to the mountainous terrain and landscapes a hiker would encounter by walking along the surface. On this surface, molecular geometries correspond to the location of the minima in the valleys. Reaction rates can be identified by the height or energy difference between a reactant minimum and the transition state. Moreover, the stability of different isomers can be assessed by the relative difference in elevation or energy of the minima. Similarly, the curvature and shape of the valley at a minimum allows you to compute a molecule's vibrational spectrum. These and many more molecular properties rely on the location of these minima and their relative energy levels on a PES.

5.2 The Newton-Raphson Method

Finding minima or stable geometries on a PES has become routine, efficient, and relatively easy to locate. This is due to Newton-Raphson optimization-based algorithms, which are known to have a quadratic convergence. The basis of these algorithms is to use a multivariable second-order Taylor series expansion of the PES.

$$E(\mathbf{x}) = \mathrm{E}(\mathbf{x}_0) + \boldsymbol{g}_\mathbf{0}^\mathrm{T}\Delta\mathbf{x} + \frac{1}{2}\Delta\mathbf{x}^{\boldsymbol{T}}\boldsymbol{H}_\mathbf{0}\Delta\mathbf{x} \tag{5.1}$$

where $\boldsymbol{g}_\mathbf{0}$ is the gradient of $E(\mathrm{x})$ evaluated at $\mathbf{x}_\mathbf{0}$ and $\boldsymbol{H}_\mathbf{0}$ is the hessian of $E(\mathbf{x})$ evaluated at $\mathbf{x}_\mathbf{0}$. The gradient, $\boldsymbol{g}$, of the Taylor expansion can then be written as

$$\boldsymbol{g}(\mathbf{x}) = \boldsymbol{g}_\mathbf{0} + \boldsymbol{H}_\mathbf{0}\Delta\mathbf{x} \tag{5.2}$$

setting gradient equal to zero and solving for $\Delta\mathbf{x}$ results in

$$\Delta\mathbf{x} = -\boldsymbol{H}_\mathbf{0}^{-1}\boldsymbol{g}_\mathbf{0} \tag{5.3}$$

expanding $\Delta\mathbf{x}$ for the k-th iterate gives the full update step

$$\mathbf{x}_\mathbf{k+1} = \mathbf{x}_\mathbf{k} - \boldsymbol{H}_\mathbf{k}^{-1}\boldsymbol{g}_\mathbf{k} \tag{5.4}$$

5.2.1 The Hessian Eigen Basis

Newton-Raphson is often praised for its fast quadratic convergence and accurate steps, due to curvature information from the Hessian, compared to other first-order methods such as gradient descent. However, Newton-Raphson has some draw backs such as sensitivity to initial guess meaning if the initial guess is poor the method may diverge or converge to unintended solution. In geometry optimizations this remedied by using a starting geometry that uses molecular mechanics parameters or an optimized lower level of theory structure. A concern with this method is the need to invert the Hessian matrix which has a cost of $\mathcal{O}(N^3)$ where N is the size of the matrix. However, since SCF methods like HF and DFT have a scaling of roughly $\mathcal{O}(K^4)$, where K is the number of basis functions, $\mathcal{O}(N^3)$ operations do not contribute significantly as in other cases. A larger problem is that matrix inversion implicates that the Hessian must be non-singular. To deal with this, the update step can be rewritten in the Hessian eigen basis as follows.

$$\begin{aligned}
\Delta\mathbf{x} &= -\boldsymbol{H}^{-1}\boldsymbol{g} \\
\boldsymbol{H}^{-1} &= \boldsymbol{V}\boldsymbol{\Lambda}^{-1}\boldsymbol{V}^{\boldsymbol{T}} \\
\Delta\mathbf{x} &= -\mathbf{V}\boldsymbol{\Lambda}^{-1}\boldsymbol{V}^{\boldsymbol{T}}\boldsymbol{g} \\
\boldsymbol{V}^{\boldsymbol{T}}\Delta\mathbf{x} &= -\boldsymbol{\Lambda}\boldsymbol{V}^{\boldsymbol{T}}\boldsymbol{g}
\end{aligned} \tag{5.5}$$

since the Hessian, $\boldsymbol{H}$, is symmetric the eigen vectors, $\boldsymbol{V}$, are orthogonal and the diagonal matrix, $\boldsymbol{\Lambda}$, of eigen values, λ_i, are real. Defining new primed variables in the eigen basis then gives

$$\begin{aligned}
\Delta\boldsymbol{x}' &= \boldsymbol{V}^{\boldsymbol{T}}\Delta\mathbf{x} \\
\boldsymbol{g}' &= \boldsymbol{V}^{\boldsymbol{T}}\boldsymbol{g}
\end{aligned} \tag{5.6}$$

which results in the primed coordinate Newton-Raphson update step.

$$\mathbf{\Delta x'} = -\mathbf{\Lambda^{-1}} \boldsymbol{g'} \tag{5.7}$$

The advantage of being in the Hessian eigen basis is that it is diagonal, and the matrix vector multiplication can be rewritten for each component of the update as follows.

$$\Delta \mathrm{x'_i} = -\frac{g'_i}{\lambda_i} \tag{5.8}$$

Notice as well that the update step in component form also removes the need to invert the Hessian since we diagonalized it instead. Additionally, the $\mathcal{O}(N^2)$ need for a matrix vector multiply between $\mathbf{\Lambda^{-1}}$ and $\boldsymbol{g}$ in component form is reduced to a division of $\mathcal{O}(N)$. While diagonalization is still an $\mathcal{O}(N^3)$ operation we get a lot more benefits from this factorization. For example, the eigen values, λ_i, can be ensured to be positive if we are searching for a minimum by taking their absolute value.

$$\Delta \mathrm{x'_i} = -\frac{g'_i}{|\lambda_i|} \tag{5.9}$$

The eigenvalues also allow you to threshold or remove search directions by setting the $\Delta \mathrm{x'}_i$ component equal to zero for eigenvalues that are close to zero determined by the threshold value. This thresholding essentially removes the singularities from the Hessian and ensures you are moving in a direction that is making progress towards the minimizer. Using the same technique, we can also make the smallest eigen value negative and all the remaining eigenvalues positive. This ensures that the stationary point we reach will be a first-order saddle point.

$$\begin{aligned} \Delta \mathrm{x'_1} &= \frac{g'_1}{|\lambda_1|} \\ \Delta \mathrm{x'_{i+1}} &= -\frac{g'_{i+1}}{|\lambda_{i+1}|} \end{aligned} \tag{5.10}$$

This method also ensures that if there are more than one negative eigenvalue it goes with the smallest or most negative. However, the most negative eigen value might not always be the imaginary frequency, ω, corresponding to the transition state of interest. Eigen vector (EF) following allows for this flexibility by choosing a specific frequency ω or normal mode q which you want to follow since they correspond to the eigen values and eigen vectors of the mass weighted Hessian. Simply it allows for the user to define and choose the eigen value and eigen vector they want to follow towards the saddle point using the same method.

The Hessian eigen basis Newton Raphson allows for exploration of the PES towards minima and transition states and alleviates a lot of concerns and pitfalls the standard Newton-Raphson update step.

5.2.2 The Trust-Region Newton-Raphson

Another strategy that is often paired with the Newton-Raphson step is a trust region. This is because the Newton-Raphson step assumes the function you're taking an update step in is a quadratic surface. However, in our case and many others, it is only an approximation to the PES therefor the step size it is suggesting you take is often too large and incorrect until you are close to a critical point also known as the quadratic region. While the direction it is suggesting is better than just gradient descent due to the curvature information from the Hessian. A scalar value which reduces the step size or region, is chosen to ensure you are always stepping towards a critical point with trust.

Mathematically this can be formulated as a constrained optimization problem with Lagrange multipliers. The function that is optimized is the second-order Taylor expansion of the energy, $E(\mathbf{x})$, and the constraint is that the norm of the step size squared stays within a radius δ.

$$\mathcal{L}(\Delta x, \lambda) = \mathrm{E}(\mathbf{x}_0) + \boldsymbol{g}_\mathbf{0}^\mathrm{T}\Delta\mathbf{x} + \frac{1}{2}\Delta\mathbf{x}^T\boldsymbol{H}_\mathbf{0}\Delta\mathbf{x} + \frac{\lambda}{2}(\|\Delta\mathbf{x}\|^2 - \delta^2) \tag{5.11}$$

To find the optimal step Δx, we then differentiate the lagragian, $\mathcal{L}$, with respect to $\Delta\mathbf{x}$ and set it equal to zero.

$$\begin{aligned}\frac{\partial\mathcal{L}}{\partial\Delta\mathbf{x}} = \boldsymbol{g}_\mathbf{0} + \boldsymbol{H}_\mathbf{0}\Delta\mathbf{x} + \lambda\Delta\mathbf{x} &= 0\\ \boldsymbol{H}_\mathbf{0}\Delta\mathbf{x} + \lambda\Delta\mathbf{x} &= -\boldsymbol{g}_\mathbf{0}\\ (\boldsymbol{H}_\mathbf{0} + \lambda\boldsymbol{I})\Delta\mathbf{x} &= -\boldsymbol{g}_\mathbf{0}\\ \Delta\mathbf{x} &= -(\boldsymbol{H}_\mathbf{0} + \lambda\boldsymbol{I})^{-1}\boldsymbol{g}_\mathbf{0}\end{aligned} \tag{5.12}$$

If the Hessian eigen basis is used and the augmented Hessian, $(\boldsymbol{H}_0 + \lambda\boldsymbol{I})$, is diagonalized, then Eq 5.12 can be written as

$$\Delta\mathbf{x} = -\sum_{i=1}^{n}\frac{\mathbf{v}_\mathrm{i}(\mathbf{v}_\mathrm{i}^T\boldsymbol{g}_\mathbf{0})}{\gamma_i - \lambda} \tag{5.13}$$

where γ_i and $\mathbf{v}_i$ are the augmented Hessian's eigenvalue and corresponding eigenvectors respectively. Similarly, to find the lagrange multiplier λ, we then differentiate the lagragian, $\mathcal{L}$, with respect to λ and set it equal to zero.

$$\begin{aligned}\frac{\partial\mathcal{L}}{\partial\lambda} = \frac{1}{2}(\|\Delta\mathbf{x}\|^2 - \delta^2) &= 0\\ \|\Delta\mathbf{x}\|^2 &= \delta^2\\ \Delta\mathbf{x}^T\Delta\mathbf{x} &= \delta^2\end{aligned} \tag{5.14}$$

plugging in the expression for $\Delta\mathbf{x}$ from Eq 5.12 into Eq 5.14 we get

$$\boldsymbol{g_0^T}(\boldsymbol{H_0}+\lambda \boldsymbol{I})^{-T}(\boldsymbol{H_0}+\lambda \boldsymbol{I})^{-1}\boldsymbol{g_0} = \delta^2 \tag{5.15}$$

since both $\boldsymbol{H_0}$ and $\boldsymbol{I}$ are symmetric then we can use the property that the inverse of a symmetric matrix is also symmetric hence simplifying the equation above to

$$(\boldsymbol{H_0}+\lambda \boldsymbol{I})^{-T} = (\boldsymbol{H_0}+\lambda \boldsymbol{I})^{-1} \tag{5.16}$$

$$\boldsymbol{g_0^T}(\boldsymbol{H_0}+\lambda \boldsymbol{I})^{-1}(\boldsymbol{H_0}+\lambda \boldsymbol{I})^{-1}\boldsymbol{g_0} = \delta^2 \tag{5.17}$$

then diagonalizing the augmented hessian into eigenvalues $\boldsymbol{\Gamma}$ and eigen vectors $\boldsymbol{V}$ and inverting it along with algebraic manipulations lead to our final form of our equation.

$$\begin{aligned}
(\boldsymbol{H_0}+\lambda \boldsymbol{I})^{-1} &= \boldsymbol{V}(\boldsymbol{\Gamma}+\lambda \boldsymbol{I})^{-1}\boldsymbol{V}^T \\
\boldsymbol{g_0^T V}(\boldsymbol{\Gamma}+\lambda \boldsymbol{I})^{-1}\boldsymbol{V}^T\boldsymbol{V}(\boldsymbol{\Gamma}+\lambda \boldsymbol{I})^{-1}\boldsymbol{V}^T\boldsymbol{g_0} &= \delta^2 \\
\boldsymbol{g_0^T V}(\boldsymbol{\Gamma}+\lambda \boldsymbol{I})^{-2}\boldsymbol{V}^T\boldsymbol{g_0} &= \delta^2 \\
\boldsymbol{g_0'} &= \boldsymbol{V^T g_0} \\
\boldsymbol{g_0'}^T(\boldsymbol{\Gamma}+\lambda \boldsymbol{I})^{-2}\boldsymbol{g'_0} &= \delta^2
\end{aligned} \tag{5.18}$$

This final equation can then be rewritten in component form as follows

$$\sum_{i=1}^{n}\frac{{g_i'}^2}{(\gamma_i+\lambda)^2} - \delta^2 = 0 \tag{5.19}$$

$$\left(\sum_{i=1}^{n}\frac{{g_i'}^2}{(\gamma_i+\lambda)^2}\right)^{\frac{1}{2}} - \delta = 0 \tag{5.20}$$

where a root solving method can now be used to solve for lambda. However, since λ is in the denominator and the equation has the form of a hyperbola, it is often rewritten in a linear form for the same answer but faster convergence and numerical stability.

$$\begin{aligned}
\|\Delta x\| &= \delta \\
\frac{1}{\|\Delta x\|} &= \frac{1}{\delta} \\
\left(\sum_{i}^{n}\frac{{g_0'}^2}{(\gamma_i+\lambda)^2}\right)^{-\frac{1}{2}} - \frac{1}{\delta} &= 0
\end{aligned} \tag{5.21}$$

Using Eq 5.12 and Eq 5.20 allows you calculate the best search direction given a second-order quadratic model to the function or PES at the given point. The last thing to do is ensure that the actual step length is not longer than the trust radius δ and evaluate the energy function at the new step, $\mathbf{x}+\Delta\mathbf{x}$, to compute the ratio, ρ, of how well the model prediction agrees with the actual difference between steps.

$$\rho = \frac{actual}{predicted} = \frac{|E(\mathbf{x}) - E(\mathbf{x} + \Delta\mathbf{x})|}{\left|E(\mathbf{x}) - \left(E(\mathbf{x}) + g^T\Delta\mathbf{x} + \frac{1}{2}\Delta\mathbf{x}^T H\Delta\mathbf{x}\right)\right|} \tag{5.22}$$

Then the value of the trust radius, δ, can be adjusted dynamically throughout the course of the optimization depending on the agreement between the actual energy difference after each step and the predicted energy difference by the second order model. The value of the ratio, ρ, then decides whether the trust radius, δ, will either shrink, expand, or remain fixed.

5.3 Quasi Newton Methods

Since analytic Hessians are computationally expensive, it is beneficial to avoid computing second derivatives if possible. While computationally cheaper, relying solely on energy and gradient evaluations means we forfeit the rapid quadratic convergence from the Hessian in the Newton-Raphson algorithm. Quasi-Newton (QN) methods address both of these concerns while only requiring the computational costs of energy and gradient evaluations. The QN step direction, $\Delta\mathbf{x}$, is still calculated using Eq 5.12, but instead of the analytical Hessian, $\boldsymbol{H}$, we use an approximate Hessian, $\boldsymbol{B}$.

$$\boldsymbol{B} \approx \boldsymbol{H} \tag{5.23}$$

$$\Delta\mathbf{x} = \boldsymbol{B}^{-1}\boldsymbol{g} \tag{5.24}$$

The first QN step can be initialized with either an empirical Hessian, numerically with finite differences, or a Hessian that was previously computed at a lower level of theory. Then subsequent steps in the optimization use Hessians that are computed using Hessian updating schemes. Hessian updating schemes approximates the true Hessian by using the change in position, $\Delta\mathbf{x}$, and gradients from previous steps. Some of the most commonly used updates depend on whether the approximated Hessian is updated using a symmetric rank 1 or rank 2 matrix update.[76]

$$\boldsymbol{B}_{k+1} = \boldsymbol{B}_k + \alpha\mathbf{v}\mathbf{v}^T \tag{5.25}$$

$$\boldsymbol{B}_{k+1} = \boldsymbol{B}_k + \alpha\mathbf{v}\mathbf{v}^T + \beta\mathbf{u}\mathbf{u}^T \tag{5.26}$$

The other important criteria are that the new updated hessian must be symmetric

$$\boldsymbol{B}_k^T = \boldsymbol{B}_k \tag{5.27}$$

and constrained to the secant equation which is just the multidimensional finite difference for the approximate hessian.

$$\Delta\mathbf{y} = \boldsymbol{g}_{k+1} - \boldsymbol{g}_k \tag{5.28}$$

$$\boldsymbol{B}_{k+1}\Delta\mathbf{x} = \Delta\mathbf{y} \tag{5.29}$$

Then using the method of lagrange multipliers and minimizing a weighted Frobenius norm between the difference of $\boldsymbol{B}_{k+1}$ and $\boldsymbol{B}_k$ gives

$$\|\boldsymbol{B}_{k+1} - \boldsymbol{B}_k\|_F \tag{5.30}$$

and leads to many of the following Hessian update formulas. Lastly, if the inverse Hessian is needed instead and the update is a rank 1 or rank 2 matrix then the Sherman-Morrison-Woodberry formula can be used to get the expression for the inverse Hessian.[77]

Some of the most common updates include the symmetric rank 1 (SR1) or Murtagh-Sargent (MS), Davidon-Fletcher-Powell (DFP), and Powell symmetric Broyden (PSB), and Broyden-Fletcher-Goldfarb-Shanno (BFGS).[74,76–86]

$$\boldsymbol{B}_{k+1}^{BFGS} = \boldsymbol{B}_k + \frac{\Delta \boldsymbol{g} \Delta \boldsymbol{g}^T}{\Delta \boldsymbol{g}^T \Delta \mathbf{x}} - \frac{\boldsymbol{B}_k \Delta \mathbf{x} \Delta \mathbf{x}^T \boldsymbol{B}_k^T}{\Delta \mathbf{x}^T \boldsymbol{B}_k \Delta \mathbf{x}} \tag{5.31}$$

$$\boldsymbol{B}_{k+1}^{DFP} = (\boldsymbol{I} - \frac{\Delta \mathbf{x} \Delta \boldsymbol{g}^T}{\boldsymbol{g}^T \Delta \mathbf{x}}) \boldsymbol{B}_k (\boldsymbol{I} - \frac{\Delta \boldsymbol{g} \Delta \mathbf{x}^T}{\boldsymbol{g}^T \Delta \mathbf{x}}) + \frac{\Delta \boldsymbol{g} \Delta \boldsymbol{g}^T}{\Delta \boldsymbol{g}^T \Delta \mathbf{x}} \tag{5.32}$$

$$\boldsymbol{B}_{k+1}^{SR1} = \boldsymbol{B}_k + \frac{(\Delta \boldsymbol{g} - \mathbf{B}_\mathrm{k} \Delta \mathbf{x})(\Delta \boldsymbol{g} - \mathbf{B}_\mathrm{k} \Delta \mathbf{x})^\mathrm{T}}{\Delta \mathbf{x}^\mathrm{T} (\Delta \boldsymbol{g} - \mathbf{B}_\mathrm{k} \Delta \mathbf{x})} \tag{5.33}$$

$$\boldsymbol{B}_{k+1}^{PSB} = \boldsymbol{B}_k + \frac{(\Delta \boldsymbol{g} - \mathbf{B}_\mathrm{k} \Delta \mathbf{x}) \Delta \mathbf{x}^T + \Delta \mathbf{x} (\Delta \boldsymbol{g} - \mathbf{B}_\mathrm{k} \Delta \mathbf{x})^T}{\Delta \mathbf{x}^T \Delta \mathbf{x}} - \frac{\Delta \mathbf{x}^T (\Delta \boldsymbol{g} - \boldsymbol{B}_k \Delta \mathbf{x}) \Delta \mathbf{x} \Delta \mathbf{x}^T}{(\Delta \mathbf{x}^\mathrm{T} \Delta \mathbf{x})^2} \tag{5.34}$$

The BFGS Hessian update is considered the best for minimizations and is given by Eq 5.31.[87] This is because it is symmetric, numerically robust, positive definite, and rank two. Additionally, the inverse Hessian has a closed form, which is needed to form the Newton-Raphson step.

$$\boldsymbol{B}_{k+1}^{-1(BFGS)} = \frac{(\mathbf{I} - \Delta \mathbf{x} \Delta \boldsymbol{g}^T)}{\Delta \mathbf{x}^T \Delta \boldsymbol{g}} \boldsymbol{B}_k^{-1} \frac{(\mathbf{I} - \Delta \boldsymbol{g} \Delta \mathbf{x}^T)}{\Delta \mathbf{x}^T \Delta \boldsymbol{g}} + \frac{\Delta \mathbf{x} \Delta \mathbf{x}^T}{\Delta \mathbf{x}^T \Delta \boldsymbol{g}} \tag{5.35}$$

$$\Delta \mathbf{x} = -\boldsymbol{B}^{-1} \boldsymbol{g} \tag{5.36}$$

This avoids forming B_k and then inverting it at each iteration, relying on the differences in positions and gradients to compute the inverse Hessian in one step. While the other Hessian updates can be inverted using the Sherman-Morrison-Woodberry formula, they are not as numerically robust, which comes from the fact that the BFGS Hessian update minimizes the difference in the inverse Hessian as opposed to the difference in the Hessian.

5.4 TS Optimization Methods

In contrast, finding transition states that connect one minimum to another remains a challenge. The ability to efficiently find a transition state depends upon numerical optimization algorithms that are able to locate first-order saddle points. This is mainly because first-order saddle points are defined as the highest energy point on a PES

connecting adjacent minima. This path is referred to as the minimum energy path (MEP) and goes through the reactant, transition state, and product. Topologically the transition state can be described as the top of the lowest mountain pass connecting two valleys. This means the TS connecting all three stationary points, has negative curvature but has local upward curvature in all other directions.

Mathematically this suggests the Hessian at the TS has one and only one negative eigen value and all the other eigen values must be positive. Furthermore, the Hessian is also known as the force constant matrix and the vibrational frequencies correspond to the square root of the eigenvalues of the mass-weighted Hessian. This means at the TS the mass-weighted Hessian has one and only one imaginary frequency. Consequently, the corresponding eigen vector of that imaginary frequency is known as the transition vector. Physically the transition vector is related to the molecular displacements going through the TS along the reaction coordinate. The transition vector can then be visualized using normal mode analysis to see if the located TS corresponds to the reaction of interest.

One popular method for locating TSs is the QST2 method. It uses a reactant structure and a product structure to bound the TS and form an approximate reaction path going through the TS using a quadratic curve. A third point can be used if a guess for the TS is given, and the approximate quadratic path then uses all three structures to find the maximum of this path. Once the maximum of the is quadratic path is reaction a full QN step is taken toward the TS. Once a step has been the new coordinates are then used with the reactant and product to find the maximum on this new quadratic path.[88–90] However since QN methods require an initial Hessian this method relies on a good initial guess that has at least one negative eigen value and a correspond eigen vector that is parallel to the desired path. Therefore, Hessian updating that allows for indefinite Hessians is needed and accurate Hessians to produce a suitable transition vector to follow. Hence if the TS is not an average structure of the reactant and product or if the Hessian becomes ill conditioned then this method can fail.

Another approach is to optimize an entire reaction path connecting the reactant and products. This is done by discretizing the path connecting reactant and product into points also known as images or states forming an elastic band. Then the energies of all these points can be minimized by constraining the points to be equally spaced by including a harmonic potential to update all the points. The tangent at each point is calculated used to project and decompose the PES gradient and harmonic gradient into parallel and perpendicular components. The points are then updated parallel with the PES gradient and perpendicularly using the harmonic gradient.[91–93] While this method works and other updating schemes such as quasi-newton methods can be used to update the points. It can become very expensive due to the large number of points needed to map the minimum energy path connecting the reactant, product and transition state.

5.5 Gradient Decomposition Method

This method aims to design a new transition method using only energy and gradient evaluations. This method performs this by generating a TS guess close to the saddle point quadratic region such that a second-order method or Quasi-Newton methods should be able locate the TS. Generating this guess close to the quadratic region eliminates the need to use chemical intuition or methods that require a user-provided input structure to locate the TS. The goal is to minimize the number expensive quantum chemical calculations without the need for a TS guess from a user.

The gradient decomposition method works by iteratively decomposing the cartesian molecular coordinates onto their respective parallel and perpendicular gradient components along a linear reaction path formed by the reactant and product structures. At each step, a new linear reaction path is formed from the new reactant, the new product, or both, depending on which one took a step during that iteration. To decide if the reactant, product, or both are taking step a predefined parameter, $\mathcal{E}$, is defined such that the reactant coordinates, $\mathbf{x}_R$, and the product coordinates, $\mathbf{x}_P$, energies are evaluated for each new step to compute the energy difference against the parameter $\mathcal{E}$. If ΔE between the reactant and product is less than $\mathcal{E}$ than both the reactant and product coordinates are updated. However, if ΔE is greater than $\mathcal{E}$, only the reactant or product with the lower energy is allowed to be updated. This condition for deciding which coordinates are updated is to minimize the number of gradient evaluations and a led to a very important feature of our method which will be discussed later.

Once you know you know whose coordinates are being updated that iteration you can use the current coordinates to form an approximate linear reaction path, $\mathbf{x}_{PR}$.

$$\mathbf{x}_{PR} = \mathbf{x}_P - \mathbf{x}_R \tag{5.37}$$

$$\hat{\mathbf{x}}_{PR} = \frac{\mathbf{x}_{PR}}{\|\mathbf{x}_{PR}\|} \tag{5.38}$$

For the first iteration both reactant and product coordinates are updated along the linear reaction path from their respective minima to avoid zero gradients. At each iteration the linear reaction path is defined as the parallel direction along which a transition state is located. Since a first-order saddle point is defined as maximum in one direction and a minimum in all others we want to move up the parallel direction and down all other perpendicular directions. We can do this by computing the gradient, $\boldsymbol{g}$,at each step and projecting the gradient onto the parallel direction, $\mathbf{x}_{PR}$. Then the perpendicular direction, $\boldsymbol{g}_\perp$, is easily defined as the orthogonal complement of the parallel direction.

$$\boldsymbol{g} = \boldsymbol{\nabla} E \tag{5.39}$$

$$\boldsymbol{g}_{\parallel} = (\boldsymbol{g}^{\mathrm{T}} \hat{\mathbf{x}}_{\boldsymbol{PR}})\, \hat{\mathbf{x}}_{\boldsymbol{PR}} \tag{5.40}$$

$$\widehat{\boldsymbol{g}}_{\parallel} = \frac{\boldsymbol{g}_{\parallel}}{\|\boldsymbol{g}_{\parallel}\|} \tag{5.41}$$

$$\boldsymbol{g}_{\perp} = \boldsymbol{g} - \boldsymbol{g}_{\parallel} \tag{5.42}$$

$$\widehat{\boldsymbol{g}}_{\perp} = \frac{\boldsymbol{g}_{\perp}}{\|\boldsymbol{g}_{\perp}\|} \tag{5.43}$$

Since we want to step up in the parallel direction, we perform gradient ascent in this direction. A parameter α_0 is chosen to decide the largest acceptable step size that can be taken in the parallel direction if not the step is just scaled by the parallel gradient.

$$\Delta \mathbf{x}_{\parallel} = \alpha\, \hat{\mathbf{x}}_{\boldsymbol{PR}} \tag{5.44}$$

$$\alpha = \begin{cases} \alpha_0 & if \ \ \|\boldsymbol{g}_{\parallel}\| > \alpha_0 \\ \|\boldsymbol{g}_{\parallel}\| & if \ \ \|\boldsymbol{g}_{\parallel}\| < \alpha_0 \end{cases} \tag{5.45}$$

For the perpendicular direction, $\boldsymbol{g}_{\perp}$, we want to minimize and go down in all directions orthogonal to $\mathbf{x}_{PR}$. This can be achieved by many of the methods mentioned at the beginning of this chapter since we are performing a minimization. However, our implementation chose to use the Bofill QN Hessian update. This Hessian update is a weighted sum of the MS or SR1 with the PSB update. The SR1 update has the benefit of faster convergence to the true the Hessian and it can approximate an indefinite Hessian but can become numerically unstable. The PSB Hessian update remedies this by being able to also approximate an indefinite hessian but having greater numerical stability. To decide between when to mix in the PSB update vs the SR1 a parameter ϕ, is calculated at each step measuring the amount of numerical instability in the SR1 update.

$$\boldsymbol{B}_{k+1}^{Bofill} = \phi \boldsymbol{B}_{k+1}^{SR1} + (1-\phi)\boldsymbol{B}_{k+1}^{PSB} \tag{5.46}$$

$$\phi = \frac{\left(\Delta \mathbf{x}^{T}(\Delta \boldsymbol{g} - \boldsymbol{B}_{k}\Delta \mathbf{x})\right)^{2}}{\|\Delta \mathbf{x}\|^{2}\|\Delta \boldsymbol{g} - \boldsymbol{B}_{k}\Delta \mathbf{x}\|^{2}} \tag{5.47}$$

Once we have our updated Hessian we then project into the orthogonal subspace using a projector matrix, **P**, to ensure our QN update is only moving in the orthogonal subspace. Then the Bofill QN step is taken using $\boldsymbol{g}_{\perp}$ as follows

$$\boldsymbol{P} = I - \hat{\mathbf{x}}_{PR}\hat{\mathbf{x}}_{PR}^{T} \tag{5.48}$$

$$\boldsymbol{B}_{\perp}^{Bofill} = \boldsymbol{P}^{T}\boldsymbol{B}_{k+1}^{Bofill}\boldsymbol{P} \tag{5.49}$$

$$\Delta \mathbf{x}_{\perp} = -\beta \boldsymbol{B}_{\perp}^{-1(Bofill)}\boldsymbol{g}_{\perp} \tag{5.50}$$

As before the QN step is taken in the Hessian eigen basis and a parameter β is introduced to scale the QN step using

$$\beta = \begin{cases} \beta_0 & if \ \|\Delta \mathbf{x}_\perp\| > \beta_0 \\ \|\Delta \mathbf{x}_\perp\| & if \ \|\Delta \mathbf{x}_\perp\| < \beta_0 \end{cases} \tag{5.51}$$

Finally, the full update step is given as a combination of the parallel and perpendicular steps.

$$\Delta \mathbf{x} = \Delta \mathbf{x}_\parallel + \Delta \mathbf{x}_\perp \tag{5.52}$$

These updates continue until the distance between $\mathbf{x}_R$ and $\mathbf{x}_P$ is within a specified tolerance d. Once the distance tolerance is met on the last linear reaction path the midpoint between $\mathbf{x}_R$ and $\mathbf{x}_P$ is chosen as the TS guess which can then optimized using Newton-Raphson or QST2 to find the final optimized coordinates for the TS.

5.6 Results

In this work, we employ two analytical surfaces to test the numerical stability and robustness of our new TS method. The first analytical surface is the Müller-Brown (MB) surface given by

$$E(x,y) = \sum_{i=1}^{4} \boldsymbol{A}_i \exp[\boldsymbol{a}_i(x - \mathbf{x}_i^0)^2 + \boldsymbol{b}_i(x - \mathbf{x}_i^0)(y - \mathbf{y}_i^0) + \boldsymbol{c}_i(y - \mathbf{y}_i^0)^2] \tag{5.53}$$

where $\boldsymbol{A}$ = (-200, -100, -170, 15), $\mathbf{x}_0$ = (1, 0, -0.5, -1), $\mathbf{y}_0$= (0, 0.5, 1.5, 1), and $\boldsymbol{a}$ = (-1, -1, -6.5, 0.7), $\boldsymbol{b}$ = (0, 0, 11, 0.6), $\mathbf{c}$ = (-10, -10, -6.5, 0.7).[94] The topology of this surface is characterized by two transition states TS1 and TS2 located at (-0.822, 0.624) and (0.212, 0.293) respectively. Along with three minima A, B, and C located at (-0.558, 1.442), (0.623, 0.028), and (-0.050, 0.467) respectively. Since the MB surface has multiple stationary points, it forms and a high degree of curved path between stationary it forms a challenging surface for new TS optimization algorithms. Consequently, the MB surface is often the go to surface for testing new TS optimization methods.

The other analytical surface used to test the new method was the Schlegel surface. This surface is given by

$$E(x,y) = \sum_{i=1}^{9} \boldsymbol{a}_i \exp[-\boldsymbol{b}_i(x - \boldsymbol{c}_i)^2 - \boldsymbol{d}_i(y - \boldsymbol{e}_i)^2] \tag{5.54}$$

where $\boldsymbol{a}$ = (1.7, 1.7, 0.8, 0.8, -1, -1, -0.25, -0.25, -0.5), $\boldsymbol{b}$ = (1.5, 1.5, 4, 4, 14, 14, 4, 4, 4), $\boldsymbol{c}$ = (-0.25, 1.75, -0.1, 1.6, 0.35, 1.15, -0.75, 2.25, 0.75), $\boldsymbol{d}$ = (4, 4, 4, 4, 4, 4, 4, 4, 4), and $\boldsymbol{e}$ = (0.5, 0.5, -0.95, -0.95, -0.75, -0.75, -0.75, -0.75, 1.2). This is another well used surface that features first-order TSs, higher order TSs, inflection points, curved paths, and minima. Its higher topological complexity and additional stationary points make it a difficult test for new methods to locate specific stationary points (see Figure 5.1). Both the MB and

Schlegel surfaces serve as model chemical potential energy surfaces due their high degree of intricacies.

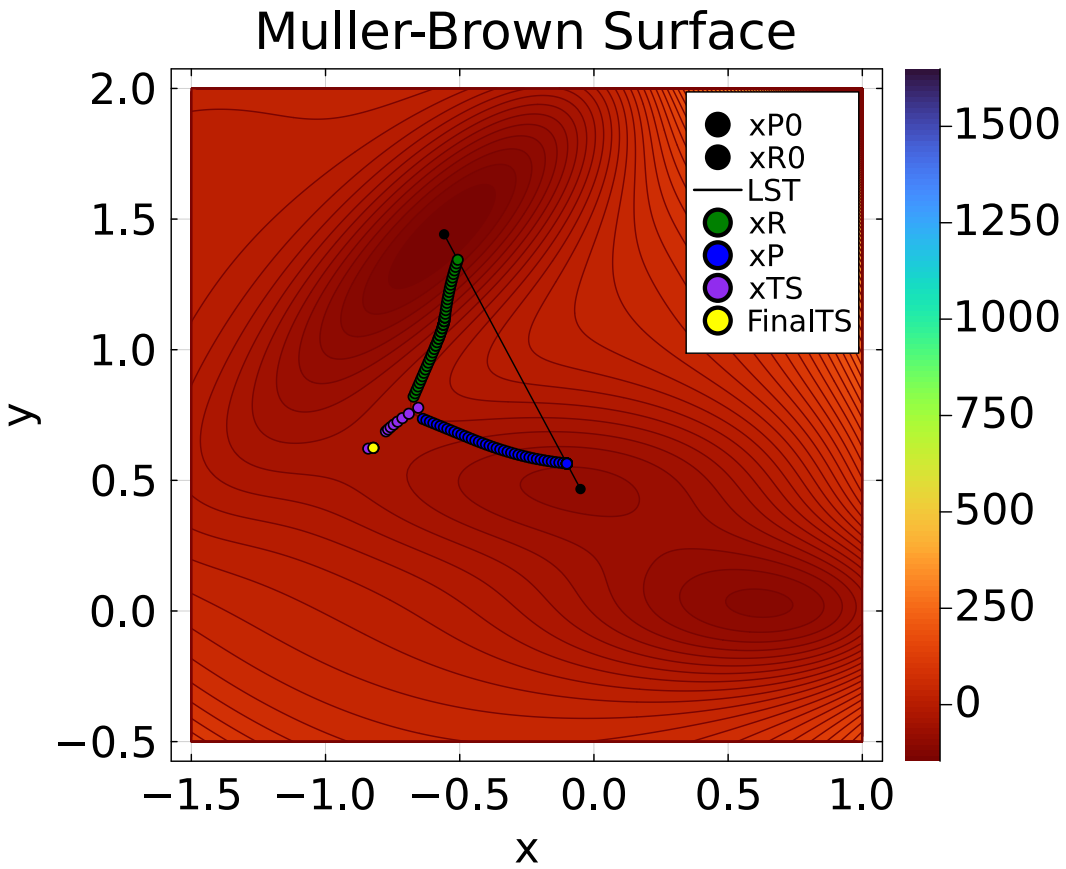


Figure 5.2 Gradient Decomposition Method between adjacent minima on the Muller-Brown surface.

In our experience the parameters $\mathcal{E}, \alpha_0, \beta_0$, and d that worked the best are 0.001 a.u, 0.01 a.u., 0.01 a.u., and 0.1 a.u. respectively. Our method was first initialized with minima A and B on the MB surface. Figure 5.2 shows the trajectory followed by the reactant and product towards the quadratic region of TS1. Notice that the trajectories for both structures begin by a displacement along the linear energy path. While the step size of both structures is the same, it can be observed that the reactant did take more steps. This is expected since minimum A is lower in energy than minimum B. This is a consequence of implementing the difference in energy condition and why it is important that only one structure is allowed to be updated while the other waits until the energy difference is within the threshold. We also observe that the path both structures is different reflects the local gradient projections for each structure. This property allows each trajectory to be different and tolerates reactants and products that have different local topographies. This is important since real chemical system will not always have symmetrical local topologies and our method allows for that variation in its initialization. Another trait that can be observed is that trajectories both get closer to quadratic region of the TS with each step due

to the perpendicular step using a Bofill Hessian update. Finally, we observe that the TS guess generated by the midpoint of the two final structures is with the quadratic region of the TS and is easily located with Newton-Raphson.

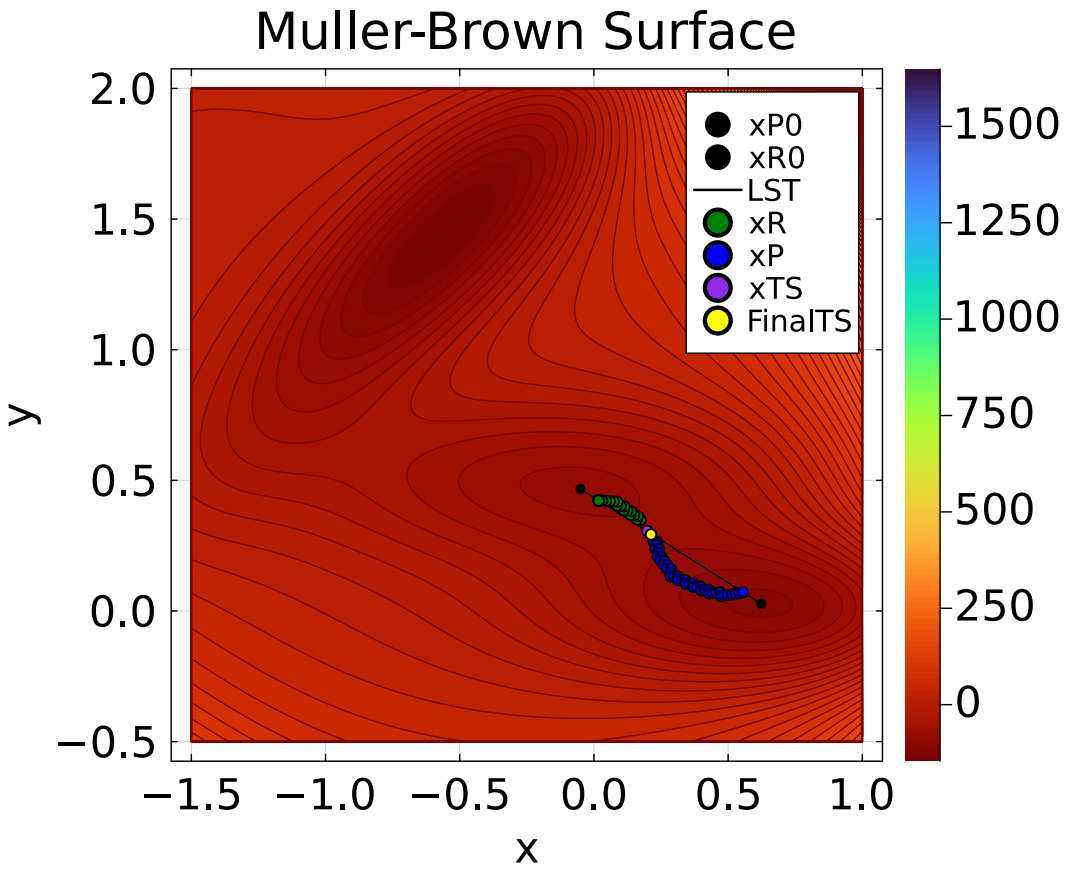


Figure 5.3 Gradient Decomposition Method between adjacent minima on the Muller-Brown Surface

We then tested MB surface initialized from minimum B and C to see if we could locate TS2 Figure 5.3. Compared to Figure 5.2 we see that the degree of curvature affected the initial trajectories of the reactant and products starting off in different directions. Despite this both trajectories self-correct and locate each other within the quadratic region of TS2. Furthermore, the product trajectory is longer than the reactant path this time, indicating the saddle point is closer to the reactant as oppose to the previous trajectory. This highlights that this method can handle both reactant like and product like TSs reliably. Also the guess that was generated for TS2 was a lot closer to the final TS and took fewer Newton-Raphson steps compared to locating TS1.

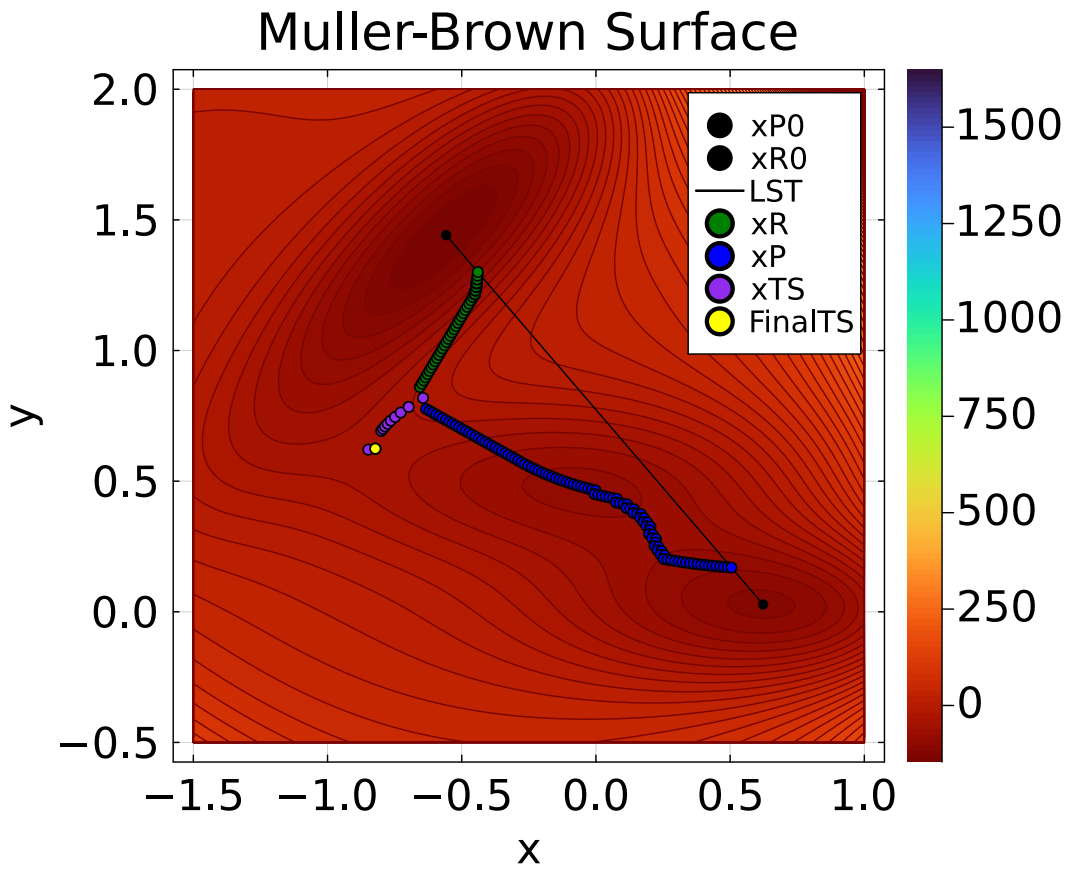


Figure 5.4 Gradient Decomposition Method between nonadjacent minima on the Muller-Brown surface.

The last initialization state we tried used started from minima A and C. This initialization was to model a multistep reaction since there was minimum B in between A and C, which could be interpreted as an intermediate formed in a chemical reaction. Additionally, there was two possible transition state that could be found TS1 and TS2 (Figure 5.4). The results showed that once again we were able to locate a TS reliably but we actually able to locate the higher energy TS1 state. This is very significant because TS1 in this model would be the rate determining step and the TS that you would mostly likely like to optimize in chemical reaction. Furthermore, the trajectory traced out by the product structure had to traverse TS2 and minimum B and was not stalled by either of the two stationary points with different characteristics. This demonstrates the robustness of the method to different stationary points and curvatures.

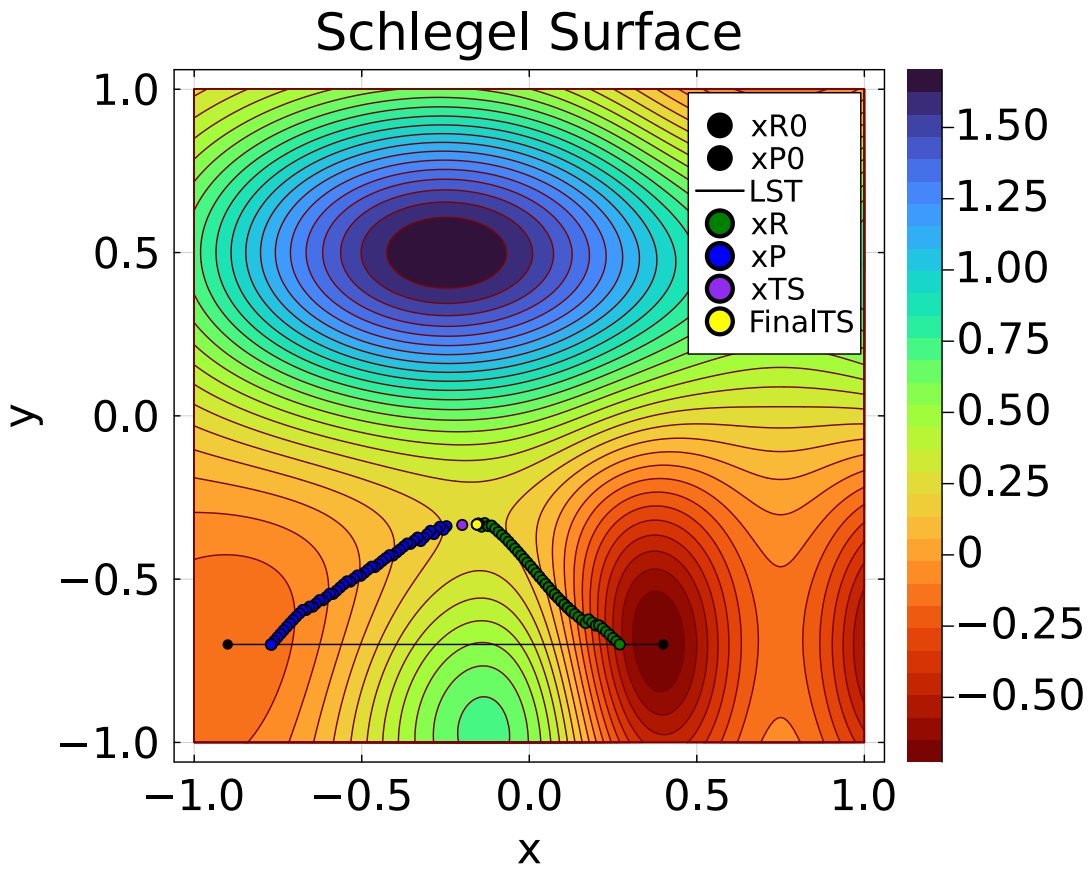


Figure 5.5 Gradient Decomposition Method between adjacent minima on the Schlegal surface.

The last initialization we tested was with the Schlegel surface to test a different surface's topology and curvature. The method once again was able to reliability locate a transition state. As can be seen on Figure 5.1and Figure 5.5 the Schlegel surface has many different minima and TSs of varying degree. Our method located the TS that was between the two adjacent minima. Another striking feature however was its ability to distinguish between the first-order saddle point and the second-order saddle point. This demonstrated its strength towards being to specifically generate TS guesses for first-order saddle points and locate them with very few Newton-Raphson steps.

5.7 Conclusions

We designed a first order TS optimization algorithm that can locate TS guesses within the quadratic region of the TS. The final optimization using standard NR based methods is sufficient to find the TS in most cases. We have tested our algorithm on 2 analytic surfaces. This early work demonstrates algorithmic efficacy however fixed vs. dynamic step size control remains an open question for further study. A defining feature of the method is its ability to consistently locate the higher energy TS in the presence of multiple TSs. Additionally, the method is tolerant to different potential energy surfaces of varying curvature. The trajectory and updates generated are tolerant to different stationary points of different characteristics. Lastly, the new method can distinguish and generate

guesses for first first-order saddle points in the presence of higher order saddle-points. All these descriptions make it a suitable and dependable method that can be used for first-order saddle points.

Future work will consider using different Hessian updating schemes for the perpendicular update direction. For example, mixing the SR1 update with either the DFP or BFGS update. Another possible direction is to just Broyden style updates where you can use a weighted combination of both the DFP and BFGS or replacing the SR1 with the PSB update and mix with either BFGS or DFP. While most of the work shown here was done in cartesian coordinates for simplicity or the coordinates can be used such as internal coordinates. These are coordinates systems that haven been known to reduce the number optimization steps by decoupling entries in the Hessian. Finally, molecular cases are need to fully validate it against real world scenarios. Molecules of choice would be HCN, Acetone, and methyl chloride with a chloride anion. These reactions would test various different kind of common elementary steps found in common mechanism and are used routine to validate model surface results.

References

1. Schrödinger, E. An Undulatory Theory of the Mechanics of Atoms and Molecules. *Physical Review* **28**, 1049 (1926).
2. Born, M. & Oppenheimer, R. Zur Quantentheorie der Molekeln. *Ann. Phys.* **389**, 457–484 (1927).
3. Hartree, D. R. The Wave Mechanics of an Atom with a Non-Coulomb Central Field. Part I. Theory and Methods. *Mathematical Proceedings of the Cambridge Philosophical Society* **24**, 89–110 (1928).
4. Hartree, D. R. The Wave Mechanics of an Atom with a Non-Coulomb Central Field. Part II. Some Results and Discussion. *Mathematical Proceedings of the Cambridge Philosophical Society* **24**, 111–132 (1928).
5. Slater, J. C. The Self Consistent Field and the Structure of Atoms. *Physical Review* **32**, 339 (1928).
6. Artree, D. R. H. & Artree (, W. H. Self-consistent field, with exchange, for beryllium. *Proc. R. Soc. Lond. A Math. Phys. Sci.* **150**, 9–33 (1935).
7. Artree, D. R. H. & Artree, W. H. Self-consistent field, with exchange, for beryllium - II—The (2s) (2p) 3P and 1P excited states. *Proc. R. Soc. Lond. A Math. Phys. Sci.* **154**, 588–607 (1936).
8. Fock, V. Näherungsmethode zur Lösung des quantenmechanischen Mehrkörperproblems. *Zeitschrift für Physik* **61**, 126–148 (1930).
9. Jensen Frank. Introduction to Computational Chemistry, 3rd Edition | Wiley. *Wiley* 660 (2017).
10. Roothaan, C. C. J. New Developments in Molecular Orbital Theory. *Rev. Mod. Phys.* **23**, 69 (1951).
11. Löwdin, P. O. On the Nonorthogonality Problem. *Advances in Quantum Chemistry* **5**, 185–199 (1970).
12. Kohn, W. & Sham, L. J. Self-Consistent Equations Including Exchange and Correlation Effects. *Physical Review* **140**, A1133 (1965).
13. Hohenberg, P. & Kohn, W. Inhomogeneous Electron Gas. *Physical Review* **136**, B864 (1964).
14. Langreth, D. C. & Mehl, M. J. Beyond the local-density approximation in calculations of ground-state electronic properties. *Phys. Rev. B* **28**, 1809 (1983).
15. Perdew, J. P. *et al.* Atoms, molecules, solids, and surfaces: Applications of the generalized gradient approximation for exchange and correlation. *Phys. Rev. B* **46**, 6671 (1992).
16. Loos, P. F. & Gill, P. M. W. The uniform electron gas. *Wiley Interdiscip. Rev. Comput. Mol. Sci.* **6**, 410–429 (2016).
17. physics, A. B.-T. J. of chemical & 1996, undefined. Density-functional thermochemistry. IV. A new dynamical correlation functional and implications for exact-exchange mixing. *lab409chem.ccu.edu.twAD BeckeThe Journal of chemical physics, 1996•lab409chem.ccu.edu.tw* https://lab409chem.ccu.edu.tw/var/file/80/1080/img/1707/B95_Becke_JCP_1996.pdf (1996).

18. Becke, A. D. Density-functional thermochemistry. III. The role of exact exchange. *J. Chem. Phys.* **98**, 5648–5652 (1993).
19. Goerigk, L. & Grimme, S. Double-hybrid density functionals. *Wiley Interdiscip. Rev. Comput. Mol. Sci.* **4**, 576–600 (2014).
20. Foresman, J. B., Head-Gordon, M., Pople, J. A. & Frisch, M. J. Toward a systematic molecular orbital theory for excited states. *Journal of Physical Chemistry* **96**, 135–149 (2002).
21. Dreuw, A. & Head-Gordon, M. Single-Reference ab Initio Methods for the Calculation of Excited States of Large Molecules. *Chem. Rev.* **105**, 4009–4037 (2005).
22. Sekino, H. & Bartlett, R. J. A linear response, coupled-cluster theory for excitation energy. *Int. J. Quantum Chem.* **26**, 255–265 (1984).
23. Nakatsuji, H. & Hirao, K. Cluster expansion of the wavefunction. Symmetry-adapted-cluster expansion, its variational determination, and extension of open-shell orbital theory. *J. Chem. Phys.* **68**, 2053–2065 (1978).
24. Runge, E. & Gross, E. K. U. Density-Functional Theory for Time-Dependent Systems. *Phys. Rev. Lett.* **52**, 997 (1984).
25. Lee, F. Y. F., Workman, P., Roberts, J. T. & Bleehen, N. M. Clinical pharmacokinetics of oral CCNU (Lomustine). *Cancer Chemother. Pharmacol.* **14**, 125–131 (1985).
26. Garg, U. C. & Hassid, A. Inhibition of rat mesangial cell mitogenesis by nitric oxide-generating vasodilators. *American Journal of Physiology - Renal Fluid and Electrolyte Physiology* **257**, (1989).
27. Y, Z., PM, V. & SW, L. Vascular nitric oxide: Beyond eNOS. *J. Pharmacol. Sci.* **129**, 83–94 (2015).
28. Hall, A. H., Saiers, J. & Baud, F. Which cyanide antidote? Which cyanide antidote? Hall et al. *Crit. Rev. Toxicol.* **39**, 541–552 (2009).
29. Namkoong, S. & Kim, Y.-M. Therapeutic Application of Nitric Oxide in Human Diseases. *Biomol. Ther. (Seoul).* **18**, 351–362 (2010).
30. Peng George Wang, * *et al.* Nitric Oxide Donors: Chemical Activities and Biological Applications. *Chem. Rev.* **102**, 1091–1134 (2002).
31. Mukhopadhyay, S. & Batra, S. Applications of Sodium Nitrite in Organic Synthesis. *European J. Org. Chem.* **2019**, 6424–6451 (2019).
32. Chaskar, A. C., Langi, B. P., Deorukhkar, A. & Deokar, H. Bismuth chloride-sodium nitrite: A novel reagent for chemoselective N-nitrosation. *Synth. Commun.* **39**, 604–612 (2009).
33. Célariès, B. & Párkányi, C. Tin(IV) Chloride-Sodium Nitrite as a New Nitrosating Agent for N-Nitrosation of Amines, Amides and Ureas under Mild and Heterogeneous Conditions. *Synthesis (Stuttg).* **2006**, 2371–2375 (2006).
34. Borikar, S. P. & Paul, V. N-nitrosation of secondary amines using p-TSA-NaNO2 as a novel nitrosating agent under mild conditions. *Synth. Commun.* **40**, 654–660 (2010).
35. Doyle, . P *et al.* Hydrolysis, nitrosyl exchange, and synthesis of alkyl nitrites. *ACS PublicationsMP Doyle, JW Terpstra, RA Pickering, DM LePoireThe Journal of Organic Chemistry, 1983•ACS Publications* **48**, 3379–3382 (1983).

36. Li, P. & Jia, X. tert-Butyl Nitrite (TBN) as a Versatile Reagent in Organic Synthesis. *Synthesis (Stuttg).* **50**, 711–722 (2017).
37. Yaghoubi, M., Rajaram, P., Sarabia, C. & Baxter, R. 3,3-Dimethyl-2-Nitroso-2,3-Dihydrobenzo[d]Isothiazole-1,1-Dioxide. *Encyclopedia of Reagents for Organic Synthesis* 1–2 (2022).
38. Galloway, J. D., Sarabia, C., Fettinger, J. C., Hratchian, H. P. & Baxter, R. D. Versatile New Reagent for Nitrosation under Mild Conditions. *Org. Lett.* 3253–3258 (2021).
39. Ma, J. *et al.* Luminescent Covalent Organic Frameworks for Biosensing and Bioimaging Applications. *Small* **18**, 2103516 (2022).
40. Lin, L. *et al.* Luminescent graphene quantum dots as new fluorescent materials for environmental and biological applications. *TrAC Trends in Analytical Chemistry* **54**, 83–102 (2014).
41. Wang, Y. *et al.* Color-Tunable Supramolecular Luminescent Materials. *Advanced Materials* **34**, 2105405 (2022).
42. Cai, X. & Su, S. J. Marching Toward Highly Efficient, Pure-Blue, and Stable Thermally Activated Delayed Fluorescent Organic Light-Emitting Diodes. *Adv. Funct. Mater.* **28**, (2018).
43. Shan, Q. *et al.* Perovskite Quantum Dots for the Next-Generation Displays: Progress and Prospect. *Adv. Funct. Mater.* **34**, 2401284 (2024).
44. Coropceanu, V., Chen, X. K., Wang, T., Zheng, Z. & Brédas, J. L. Charge-transfer electronic states in organic solar cells. *Nature Reviews Materials 2019 4:11* **4**, 689–707 (2019).
45. Bureš, F. Fundamental aspects of property tuning in push–pull molecules. *RSC Adv.* **4**, 58826–58851 (2014).
46. Wang, D. *et al.* Achieving Color-Tunable and Time-Dependent Organic Long Persistent Luminescence via Phosphorescence Energy Transfer for Advanced Anti-Counterfeiting. *Adv. Funct. Mater.* **33**, 2208895 (2023).
47. Liu, Y., Xiao, X., Ran, Y., Bin, Z. & You, J. Molecular design of thermally activated delayed fluorescent emitters for narrowband orange–red OLEDs boosted by a cyano-functionalization strategy. *Chem. Sci.* **12**, 9408–9412 (2021).
48. Romero, N. A. & Nicewicz, D. A. Organic Photoredox Catalysis. *Chem. Rev.* **116**, 10075–10166 (2016).
49. Prier, C. K., Rankic, D. A. & MacMillan, D. W. C. Visible light photoredox catalysis with transition metal complexes: Applications in organic synthesis. *Chem. Rev.* **113**, 5322–5363 (2013).
50. Elisei, F., Favaro, G. & Romani, A. A laser flash photolysis study of di-pyridyl ketones. *Chem. Phys.* **144**, 107–115 (1990).
51. Rajan, A. K., Rajaram, P. S., Chakkanalil, K., Ghosh, S. & Baxter, R. D. Optically Tunable Properties of Small Organic Molecules via Photomediated Aza Nazarov Cyclizations. *J. Org. Chem.* **90**, 15481–15488 (2025).
52. Hurt, C. R. & Filipescu, N. Photocyclization of Di(2-pyridyl) Ketone and 2-BenzoyIpyridine in Aqueous Solution. *J. Am. Chem. Soc.* **94**, 3649–3651 (1972).
53. Hurt, C. R. & Filipescu, N. Photocyclization of Di(2-pyridyl) Ketone and 2-BenzoyIpyridine in Aqueous Solution. *J. Am. Chem. Soc.* **94**, 3649–3651 (1972).

54. physics, R. M.-T. J. of chemical & 2003, undefined. Natural transition orbitals. *pubs.aip.org* **118**, 4775–4777 (2003).
55. Le Bahers, T., Adamo, C. & Ciofini, I. A qualitative index of spatial extent in charge-transfer excitations. *J. Chem. Theory Comput.* **7**, 2498–2506 (2011).
56. Guido, C. A., Cortona, P., Mennucci, B. & Adamo, C. On the metric of charge transfer molecular excitations: A simple chemical descriptor. *J. Chem. Theory Comput.* **9**, 3118–3126 (2013).
57. Plasser, F. & Lischka, H. Analysis of excitonic and charge transfer interactions from quantum chemical calculations. *J. Chem. Theory Comput.* **8**, 2777–2789 (2012).
58. Plasser, F. TheoDORE: A toolbox for a detailed and automated analysis of electronic excited state computations. *Journal of Chemical Physics* **152**, 84108 (2020).
59. Plasser, F., Wormit, M. & Dreuw, A. New tools for the systematic analysis and visualization of electronic excitations. I. Formalism. *Journal of Chemical Physics* **141**, 24106 (2014).
60. Hansch, C., Leo, A. & Taft, R. W. A Survey of Hammett Substituent Constants and Resonance and Field Parameters. *Chem. Rev.* **91**, 165–195 (1991).
61. Fehér, P. P. & Stirling, A. Selecting the Optimal DFT Functionals for Reproducing the UV-Vis Properties of Transition-Metal Photocatalysts. *Chemistry-Methods* **5**, e202400071 (2025).
62. Laurent, A. D., Adamo, C. & Jacquemin, D. Dye chemistry with time-dependent density functional theory. *Physical Chemistry Chemical Physics* **16**, 14334–14356 (2014).
63. Chantzis, A., Cerezo, J., Perrier, A., Santoro, F. & Jacquemin, D. Optical properties of diarylethenes with td-DFT: 0-0 energies, fluorescence, stokes shifts, and vibronic shapes. *J. Chem. Theory Comput.* **10**, 3944–3957 (2014).
64. Hao, M. *et al.* Molecular Origins of Photoinduced Backward Intramolecular Charge Transfer. *Journal of Physical Chemistry C* **124**, 16820–16826 (2020).
65. Adamo, C., Jacquemin, D., Adamo, S. & Adamo ab, C. The calculations of excited-state properties with Time-Dependent Density Functional Theory. *Chem. Soc. Rev.* **42**, 845–856 (2013).
66. Mester, D. & Kállay, M. Charge-Transfer Excitations within Density Functional Theory: How Accurate Are the Most Recommended Approaches? *Cite This: J. Chem. Theory Comput* **18**, 1646–1662 (2022).
67. Herbert, J. M. & Mandal, A. Importance of Orbital Invariance in Quantifying Electron–Hole Separation and Exciton Size. *J. Chem. Theory Comput.* **20**, 9446–9463 (2024).
68. Plasser, F. & Lischka, H. Analysis of excitonic and charge transfer interactions from quantum chemical calculations. *J. Chem. Theory Comput.* **8**, 2777–2789 (2012).
69. Corzo, H. H., Abou Taka, A., Pribram-Jones, A. & Hratchian, H. P. Using projection operators with maximum overlap methods to simplify challenging self-consistent field optimization. *J. Comput. Chem.* **43**, 382–390 (2022).
70. Bovill, A. J., Taka, A. A., Harb, H. & Hratchian, H. P. Excitation/Relaxation Analysis of Electronic Transitions Using Difference Density Natural Orbitals. *J. Chem. Theory Comput.* **22**, 930–939 (2026).

71. Sun, Y., Hudson, Z. M., Rao, Y. & Wang, S. Tuning and switching MLCT phosphorescence of [Ru(bpy) 3] 2+ complexes with triarylboranes and anions. *Inorg. Chem.* **50**, 3373–3378 (2011).
72. Shi, S. *et al.* Highly Efficient Photo- and Electroluminescence from Two-Coordinate Cu(I) Complexes Featuring Nonconventional N-Heterocyclic Carbenes. *J. Am. Chem. Soc.* **141**, 3576–3588 (2019).
73. Zhang, Y., Petersen, J. L. & Milsmann, C. A Luminescent Zirconium(IV) Complex as a Molecular Photosensitizer for Visible Light Photoredox Catalysis. *J. Am. Chem. Soc.* **138**, 13115–13118 (2016).
74. Jensen, F. *Introduction to Computational Chemistry*. (John Wiley & Sons, 2017).
75. Szabo, A. & Ostlund, N. *Modern Quantum Chemistry: Introduction to Advanced Electronic Structure Theory*. (Courier Corporation, 2012).
76. Broyden, C. G. The Convergence of a Class of Double-rank Minimization Algorithms: 2. The New Algorithm. *IMA J. Appl. Math.* **6**, 222–231 (1970).
77. Shanno, D. F. Conditioning of quasi-Newton methods for function minimization. *Math. Comput.* **24**, 647–656 (1970).
78. MURTAGH BA & SARGENT RWH. Computational experience with quadratically convergent minimisation methods. *Comput. J.* **13**, 185–194 (1970).
79. Davidon, W. C. Variable Metric Method for Minimization. *https://doi.org/10.1137/0801001* **1**, 1–17 (2006).
80. Fletcher, R. & Powell, M. J. D. A Rapidly Convergent Descent Method for Minimization. *Comput. J.* **6**, 163–168 (1963).
81. Powell, M. J. D. Recent advances in unconstrained optimization. *Math. Program.* **1**, 26–57 (1971).
82. FLETCHER R. A new approach to variable metric algorithms. *Comput. J.* **13**, 317–322 (1970).
83. Goldfarb, D. A family of variable-metric methods derived by variational means. *Math. Comput.* **24**, 23–26 (1970).
84. Greenstadt, J. Variations on Variable-Metric Methods. *Math. Comput.* **24**, 1 (1970).
85. Hratchian, H. P. & Schlegel, H. B. Finding minima, transition states, and following reaction pathways on ab initio potential energy surfaces. in *Theory and Applications of Computational Chemistry* 195–249 (Elsevier, 2005). doi:10.1016/B978-044451719-7/50053-6.
86. Schlegel, H. B. Geometry optimization. *Wiley Interdiscip. Rev. Comput. Mol. Sci.* **1**, 790–809 (2011).
87. Head, J. D. & Zerner, M. C. A Broyden—Fletcher—Goldfarb—Shanno optimization procedure for molecular geometries. *Chem. Phys. Lett.* **122**, 264–270 (1985).
88. Peng, C. & Bernhard Schlegel, H. Combining Synchronous Transit and Quasi-Newton Methods to Find Transition States. *Isr. J. Chem.* **33**, 449–454 (1993).
89. Cerjan, C. J. & Miller, W. H. On finding transition states. *J. Chem. Phys.* **75**, 2800–2801 (1981).
90. Halgren, T. A. & Lipscomb, W. N. The synchronous-transit method for determining reaction pathways and locating molecular transition states. *Chem. Phys. Lett.* **49**, 225–232 (1977).

91. Henkelman, G., Uberuaga, B. P. & Jónsson, H. A climbing image nudged elastic band method for finding saddle points and minimum energy paths. *J. Chem. Phys.* **113**, 9901–9904 (2000).
92. Henkelman, G. & Jónsson, H. Improved tangent estimate in the nudged elastic band method for finding minimum energy paths and saddle points. *J. Chem. Phys.* **113**, 9978–9985 (2000).
93. JÓNSSON, H., MILLS, G. & JACOBSEN, K. W. Nudged elastic band method for finding minimum energy paths of transitions. 385–404 (1998) doi:10.1142/9789812839664_0016.
94. Müller, K. & Brown, L. D. Location of saddle points and minimum energy paths by a constrained simplex optimization procedure. *Theor. Chim. Acta* **53**, 75–93 (1979).